

УДК 539.17

THE RELATIVISTIC MEAN FIELD  
AND SOME OF ITS RECENT  
APPLICATIONS

*Y. K. Gambhir, A. Bhagwat*

Department of Physics, I. I. T. Powai, Bombay, India\*

INTRODUCTION	366
FORMULATION	372
DETAILS OF THE CALCULATIONS	377
RMF/RHB RESULTS FOR GROUND STATE PROPERTIES	379
ANTIPROTON ANNIHILATION	400
ORIGIN OF PSEUDOSPIN SYMMETRY	407
CROSS SECTIONS	412
DECAY HALF-LIVES	423
SUMMARY AND CONCLUSIONS	432
REFERENCES	433

---

\*E-mail: [yogy@phy.iitb.ac.in](mailto:yogy@phy.iitb.ac.in)

УДК 539.17

## THE RELATIVISTIC MEAN FIELD AND SOME OF ITS RECENT APPLICATIONS

*Y. K. Gambhir, A. Bhagwat*

Department of Physics, I. I. T. Powai, Bombay, India\*

Essentials of relativistic mean field (RMF) theory and some of its recent applications are presented. The explicit calculations are carried out for a few selected isotopic, isotonic, and isobaric chains of nuclei covering the entire periodic table. The calculated ground-state properties are found to be in good agreement with the corresponding experiment: the binding energies are reproduced, on the average, within 0.25%, and the charge radii differ only in the second decimal place of fermi. The relativistic origin of the pseudospin symmetry is briefly discussed. The density distributions obtained are found to be in good agreement with the experiment (where available). The peripheral factor — the ratio of the neutron and the proton densities at the nuclear periphery, extracted in the antiproton annihilation experiments — is well reproduced. The RMF densities are used to calculate the reaction ( $\sigma_R$ ) and charge-changing ( $\sigma_{cc}$ ) cross sections in the Glauber model as well as the  $\alpha$  (cluster)-daughter interaction energy. The energy in turn is employed to estimate the decay half-lives of superheavy (transactinide) nuclei in the WKB approximation. The calculations are found to agree well with the experiment. This success of the RMF in accurately describing the nuclear properties with only a few fixed parameters is indeed remarkable.

Изложена суть теории релятивистского среднего поля (РСП) и представлены некоторые из ее недавних применений. Проведены точные расчеты для нескольких выбранных изотопических, изотонических и изобарических каналов ядер, полностью охватывающие таблицу периодических элементов. Результаты вычислений свойств основного состояния находятся в хорошем согласии с соответствующим экспериментом: энергии связи воспроизводятся, в среднем, в пределах 0,25 %, а зарядовые радиусы отличаются только во втором знаке после запятой в единицах ферми. Коротко обсуждается релятивистское происхождение псевдоспиновой симметрии. Полученные распределения плотностей находятся в хорошем согласии с экспериментом (где возможен их расчет). Хорошо воспроизводится периферийный фактор — отношение плотности нейтронов к плотности протонов на периферии ядра, извлекаемое в экспериментах по протон-антипротонной аннигиляции. Плотности РСП используются для вычисления сечений реакции ( $\sigma_R$ ) и перезарядки ( $\sigma_{cc}$ ) в модели Глаубера, а также энергии  $\alpha$  (кластерного)-дочернего взаимодействия. Энергия, в свою очередь, может быть использована для оценки периодов полураспада сверхтяжелых (трансактинидных) ядер в рамках ВКБ-приближения. Расчеты находятся в хорошем согласии с экспериментом. Теория РСП успешно описывает свойства ядер при использовании всего нескольких фиксированных параметров.

---

\*E-mail: yogy@phy.iitb.ac.in

## INTRODUCTION

The formulation and application of the relativistic mean field (RMF) theory has been the most striking development in the field of nuclear structure. The RMF [1–8] is now established to be one of the most successful and satisfactory theory for the description of the nuclear structure properties. The RMF still works at the level of nucleons and mesons. It starts with a Lagrangian density describing Dirac spinor nucleons interacting via meson and photon fields. The classical Euler–Lagrange variational principle yields the equations of motion. At this stage, the mean field approximation is introduced, i.e., the fields are not quantized, but instead, are replaced by their expectation values or  $c$  numbers. This leads then to the Dirac equation with the potential terms describing the nucleon dynamics and the Klein–Gordon-type equations involving nucleonic currents and densities as source terms for mesons and the photon. This set of coupled, nonlinear differential equations, known as the RMF equations, is required to be solved self-consistently. The vacuum polarization effects are not included (no sea approximation) and the Fock exchange terms are ignored. The parameters of the effective Lagrangian of this relativistic Hartree RMF theory, are fitted and are expected to include phenomenologically the vacuum polarization and the exchange contributions.

The pairing correlations are important for the open shell nuclei. These can be incorporated either by using the simple constant gap approximation [6,8,9] or the Bogoliubov transformation [9]. The latter approach which treats the pairing correlations self-consistently, leads to the relativistic Hartree–Bogoliubov (RHB) equations [10].

The RMF/RHB equations are solved in practice either by using the conventional basis expansion technique (spherical or axially symmetric deformed harmonic oscillator basis) or in the coordinate space. The solution obtained in the coordinate space is considered to be more reliable especially for the cases where the asymptotics is expected to play a crucial role. This is due to the fact that the required boundary conditions are correctly incorporated in the coordinate space solution, thereby ensuring the correct asymptotics.

Several variants of this formulation, like the effective field theory (EFT) [11–14] and the point coupling approach (PCA) [15–17] exist. All these start with an appropriate interaction Lagrangian. The conventional RMF has  $\sigma$ ,  $\omega$ ,  $\rho$ , and  $\delta$  fields along with Dirac nucleon spinors. It has basically seven (eight) parameters (if self-coupling of  $\omega$  is included). The EFT, inspired by the QCD based expansion, includes up to quartic meson terms. Conventionally, it has thirteen parameters. On the other hand, the PCA, as the name suggests, avoids completely the meson fields and includes quadratic (including derivatives), cubic, and quartic terms of bilinear spinors. It has nine (seven) parameters (if the isovector terms are dropped). The parameters appearing in their respective Lagrangians are seldom derived. These are usually determined phenomenologically by fitting some of the

ground state properties of a few selected even–even nuclei. All the approaches, though having different number of parameters, lead, more or less, to the results of the same level of accuracy. Even the density dependence of the parameters has been investigated. It is not still clear, which one is the most appropriate. Maybe, only the future investigations will dictate.

Here, we shall consider and use only the conventional RMF ( $\sigma, \omega, \rho$  model). We analyze quantitatively the differences in the calculated observables arising due to the use of different prescriptions generally employed for the solution of the RMF/RHB equations. For example, the comparison of the results obtained by solving the RHB equations in the coordinate space and those obtained by solving the RHB equations using the spherical oscillator basis will indicate the importance of the correct asymptotics. The differences between the results obtained through the solutions of the RHB equations and those of the RMF equations with frozen gap in the spherical oscillator basis will demonstrate the contributions arising due to the self-consistent treatment of pairing. On the other hand, the comparison between the RMF results with the frozen gap in the spherical and deformed (axially symmetric) oscillator basis will highlight the importance of the deformation effects.

The experimental determination of absolute charge radii for unstable nuclei is a difficult task. However, the difference between the squared charge radii ( $\delta r_c^2$ ) of the given isotope with respect to the reference nucleus in the isotopic chain has been measured through the hyperfine splitting (isotopic shift) experiments (laser spectroscopy) [18–21]. These measurements have revealed rich information about the  $\delta r_c^2$  for the given isotopic chain with the addition/removal of neutrons. In particular, the charge radii are found to increase with removal of neutrons from specific neutron number. This is contrary to the expected  $r_0 A^{1/3}$  behavior and therefore, is termed as anomalous behavior of the isotopic shifts. Such anomalies have been observed at several places throughout the periodic table. The relativistic mean field theory has been successful in explaining these anomalies. This is explicitly demonstrated for several isotopic chains considered here.

For illustration, a few representative examples of isotopic, isotonic, and isobaric chains are selected. In particular, the calculated results for the chains of Nitrogen, Neon, Argon isotopes (sd shell), Iron isotopes (pf shell), Cesium isotopes (rare earth), Radium isotopes,  $N = 12$  isotones, and  $A = 18$  isobars have been presented and discussed in detail.

The pseudospin symmetry [22, 23] has been used in the nuclear structure physics since over thirty years. Its origin, however, remained an unresolved mystery. Only recently, the pseudospin symmetry has been shown using RMF to be purely of relativistic origin [24–27].

The antiproton ( $\bar{p}$ ) annihilation experiments [28–32] help to investigate the nuclear periphery. In such experiments, a beam of slow antiprotons is made to interact with the target. The antiproton then occupies a higher Bohr orbit

in the target nucleus. It then cascades down the Bohr orbits by emitting the characteristic antiprotonic  $X$  rays. Finally, it enters the nuclear periphery and gets annihilated upon encountering a proton or a neutron. This so-called annihilation site is estimated to be around 2.5 fm away from the half density radius of the nucleus. These experiments enable one to extract the ratio of neutron and proton densities of the target nucleus at the annihilation site through the so-called peripheral factor, which is proportional to the ratio of the corresponding annihilation probabilities [28,29]. In this peripheral region, both the neutron and proton densities are very small. Therefore, the asymptotics becomes important in the theoretical studies of nuclear densities. Further, the ratio of two very small numbers (neutron and proton densities) imposes a stringent test on the theoretical model used for the calculation of the nuclear densities. A small error even in one of them could affect the resulting ratio considerably. The peripheral factors calculated and discussed here agree well with the experiment.

The radioactive ion beam (RIB) facility helps to produce and use the unstable nuclei as secondary beams for further experimentation. The total reaction cross sections ( $\sigma_R$ ) for a number of chains of isotopes as projectiles incident on  $^{12}\text{C}$  target have been experimentally measured [33]. In practice, using these experimental reaction cross sections, the parameter in the assumed form of the neutron density distribution of the projectile is extracted within the Glauber model [34] by knowing the densities of the target nucleus and the proton density distribution of the projectile. This yields the so-called experimental neutron (matter) root-mean-square (r.m.s.) radius and the neutron (matter) density distribution of the projectile. We compare these matter radii with the corresponding calculated results. We use the calculated proton and neutron density distributions of the projectile to calculate the reaction cross sections within the Glauber model. The calculated cross sections are then directly compared with the experiment.

Another related, and important observable is the total charge-changing cross section ( $\sigma_{cc}$ ). This is defined as the total cross section for change in the charge number of the projectile. The difference between  $\sigma_R$  and  $\sigma_{cc}$  is equal to the total neutron removal cross section ( $\sigma_{-xn}$ ). The  $\sigma_{cc}$  yields information about the proton densities in the presence of neutrons in projectile. Also, it has been claimed that the  $\sigma_{cc}$  may set an upper limit over the r.m.s. charge radius of the projectile [35]. Intuitively, it appears that the  $\sigma_{cc}$  may be obtained theoretically by just using the projectile proton density in the Glauber model, instead of both the neutron and the proton densities, as is done for the  $\sigma_R$ . It has been, however, shown that this approach is conceptually deficient [36]. Experimentally, the charge-changing cross sections for all the isotopic chains from Boron to Fluorine have been recently measured [37]. Here, we calculate theoretically the  $\sigma_{cc}$  for some of these nuclei as projectiles, incident on  $^{12}\text{C}$  targets at specified energies, within the Glauber model and compare them with the corresponding experiment [37].

The superheavy nuclei have been the focus of research activity in both theoretical and experimental sectors, since the prediction of island of stability around  $Z \sim 114$  and  $N \sim 184$  [38, 39]. So far, the elements up to charge number 116 have been successfully produced in the laboratories around the world using cold/hot fusion technique [40–43]. Search for the elements with higher charge numbers is still on. These elements decay primarily by emitting  $\alpha$ 's or by spontaneous fission. Another very interesting and, perhaps, the most striking decay mode of the elements around Uranium (actinides, e.g., Rn, Ra, U, Am, etc.), is the cluster (heavier than  $\alpha$  particle) radioactivity [44–50]. So far, around thirty such decays have been reported [50]. Here, we employ the RMF formalism to investigate the structure and subsequently, the  $\alpha$  (cluster)-decay properties of the superheavy (actinides) elements.

**Why Relativistic Formulation?** The nonrelativistic analysis is known to indicate that the average field in the nucleus has almost Woods–Saxon (WS) radial shape with strength ( $U$ ) about 50 MeV. However,  $U \sim 50 \text{ MeV} \ll mc^2$  ( $\sim 1000 \text{ MeV}$ ). Now the question arises: why the relativistic formulation is required? The answer to this question is affirmative mainly due to the following reasons.

1. The conventional optical model failed to account for the measured spin observables such as the analyzing power ( $A_y$ ) and the spin rotation function ( $Q$ ) in the polarized proton–nucleus scattering experiments at the intermediate energies ( $\sim 300 \text{ MeV}$ ). As the proper description of spin is relativistic, it was therefore suggested to use the Dirac equation with Lorentz scalar ( $S$ , attractive) and vector ( $V$ , repulsive) time-like potentials, instead of the Schrödinger equation. This so-called Dirac phenomenology turned out to be remarkably successful in accurately reproducing the measured cross sections ( $\sigma$ ) and the spin variables  $A_y$  and  $Q$  [51–57]. As an illustrative example, the  $\sigma$ ,  $Q$ , and  $A_y$  calculated by using the Dirac phenomenology for the polarized proton –  $^{40}\text{Ca}$  scattering at 200 MeV are presented in Figs. 1, *a–c*. Excellent agreement between the calculated [58] and the corresponding experimental results is amply evident from these figures. It was this phenomenal success of Dirac phenomenology which triggered the numerous successful applications of RMF approach to several nuclear properties.

2. The most direct indication for the need of relativistic description stems from the observed large anomalous nuclear  $l \cdot s$  splitting. We now illustrate this below explicitly. Notice that in the atomic case  $l \cdot s$  interaction is given by the well-known Thomas formula:

$$U_{ls}^{\text{at}} = \frac{1}{4M^2} \frac{1}{r} \frac{\partial U^{\text{at}}}{\partial r} (\mathbf{l} \cdot \boldsymbol{\sigma}), \quad (1)$$

where  $U^{\text{at}}$  is the central potential, which is the sum of the Coulomb field of the nucleus and the self-consistent field, calculated using, for example, the Hartree–Fock procedure. The observed nuclear  $l \cdot s$  splitting is very large ( $\sim 30$  times)

and is of opposite sign as compared to the atomic case. This important term in the nonrelativistic description, as mentioned before, is introduced in practice, phenomenologically. Explicitly:

$$\frac{\alpha}{r} \frac{\partial \rho}{\partial r} (\mathbf{1} \cdot \boldsymbol{\sigma}), \quad (2)$$

with

$$\frac{\partial U}{\partial r} = - \frac{\partial \rho}{\partial r}, \quad (3)$$

$U \sim -50$  MeV, having WS shape.

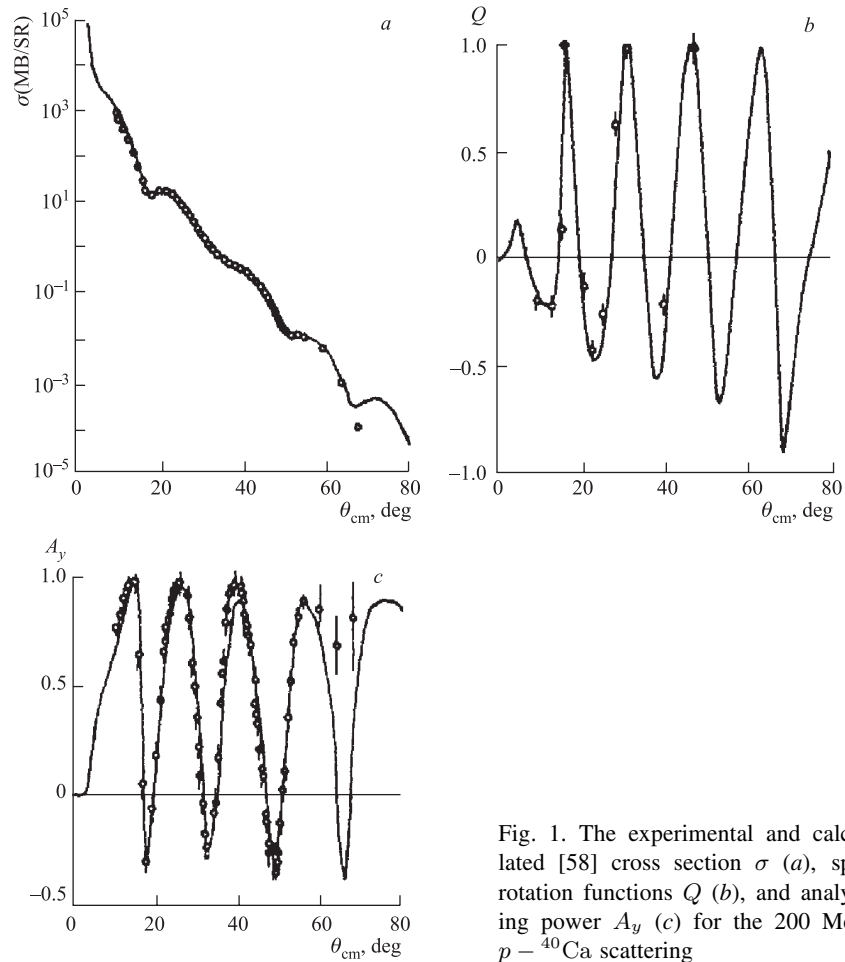


Fig. 1. The experimental and calculated [58] cross section  $\sigma$  (a), spin rotation functions  $Q$  (b), and analyzing power  $A_y$  (c) for the 200 MeV  $p - {}^{40}\text{Ca}$  scattering

We shall now show that these features do emerge from the  $\sigma$ - $\omega$  model of Walecka [1] or from the so-called Dirac phenomenology. In this picture the nucleon dynamics is governed by the Dirac equation with the static scalar ( $S$ ) and vector ( $V$ ) potentials (fields). It reads:

$$[\alpha \cdot p + \beta(M + S) + V] \Psi_\mu = E_\mu \Psi_\mu. \quad (4)$$

Rewriting this equation in terms of  $\psi_u$  ( $\psi_l$ ) upper (lower) component of the Dirac spinor ( $\Psi_\mu$ ) and eliminating the lower component  $\psi_l$ , one ends up with the following second-order differential equation (up to an accuracy of order  $\epsilon/M$ ) for the upper component  $\psi_u$ :

$$\left[ p \frac{1}{2\mathcal{M}} p + \underbrace{(S + V)} + \frac{1}{r} \underbrace{\left( \frac{\partial}{\partial r} \frac{1}{2\mathcal{M}} \right)} l\sigma \right] \psi_u = \epsilon \psi_u. \quad (5)$$

The first term in the r.h.s. of the above equation corresponds to  $U(r)$ , whereas the second term can be identified with  $U_{ls}$ . The energy  $E$  is measured relative to nucleon mass  $M$  ( $E_\mu = M + \epsilon_\mu$ ;  $\epsilon_\mu$  being negative).

This is the Schrödinger-like equation with:

(i) Central potential  $U(r) = S + V$ ;  $S - ve$  and  $|S| > |V|$ .

(ii) Mass term  $\mathcal{M} = M \left( 1 + \frac{S - V}{2M} \right)$ ,  $2\mathcal{M} = 2M + S - V$ .

(iii) Spin-orbit term:  $U_{l\sigma}$ ;  $U_{ls} = \frac{1}{r} \frac{\partial}{\partial r} \left( \frac{1}{2\mathcal{M}} \right) U_{ls}$  is large, as  $|V - S| \gg U$   
 $\mathcal{M} < M$ .

Notice that it has the correct sign and also the magnitude. Comparing this with the corresponding nonrelativistic (phenomenological) term

$$\frac{1}{r} \frac{\partial}{\partial r} \left( \frac{1}{2\mathcal{M}} \right) = \frac{\alpha}{r} \frac{\partial \rho}{\partial r} \quad (6)$$

yields:

$$\frac{1}{2\mathcal{M}} = \alpha \rho + \frac{1}{2M}. \quad (7)$$

The last term appears because for  $r \gg$  nuclear size,  $\mathcal{M} \rightarrow M$ ,  $\rho \rightarrow 0$ .

Knowing  $\alpha$  and  $\rho$  one can estimate  $V$  and  $S$ . For example, phenomenology gives:  $\alpha = 85.5 \text{ MeV} \cdot \text{fm}^5$  and  $\rho = 0.17 \text{ fm}^{-3}$ , therefore

$$\frac{\mathcal{M}}{M} = \frac{1}{1 + 2\alpha\rho M} \approx 0.6. \quad (8)$$

Thus,  $\mathcal{M} = 0.6M$  yields  $2M + S - V = 2 \times 0.6M$ ; or  $S - V = -0.8M \approx -750$  MeV. Shell model gives  $V + S \approx -50$  MeV, yielding,  $V \simeq 350$  MeV and  $S \simeq -400$  MeV.

These magnitudes of  $V$  and  $S$  are consistent with the Dirac phenomenology.

Thus, in spite of the fact that  $\epsilon/M \ll 1$ , inside the nucleus the fields acting on the nucleon are not small ( $\sim -400$  MeV,  $+350$  MeV) in comparison with its rest mass. So this is the reason why the nucleus is relativistic even though  $\epsilon/M \ll 1$ . The value  $U = -50$  MeV is the result of the delicate cancellation of two big numbers.

Section 1 presents the essentials of the RMF/RHB formulation. Some of the calculated results obtained by using the different prescriptions employed for the solution of the RMF/RHB equations, are discussed in Sec. 2. The representative results are presented and discussed in Sec. 3. The antiproton annihilation for the nuclear periphery is investigated in Sec. 4. The relativistic mean field description of pseudospin symmetry is the subject matter of Sec. 5. The calculation of the reaction and charge-changing cross sections in the Glauber model is discussed in Sec. 6. A comparative study of the calculated reaction and the charge-changing cross sections for some representative cases (Nitrogen isotopes,  $N = 12$  isotones, and  $A = 18$  isobars) is presented in the same section. The double folding model and the WKB approximation, required to calculate the  $\alpha$ /cluster decay half-lives, are discussed in Sec. 7. The explicit results for the  $\alpha$ /cluster decay of «transuranium» elements are presented and discussed. The summary and conclusions form the subject matter of Sec. 8.

## 1. FORMULATION

A review of RMF/RHB theories is in order here. In this formulation, the point nucleons are assumed to be interacting only via the  $c$ -number electromagnetic (e.m.) and meson fields. The classical mean ( $c$ -number) fields, scalar  $\sigma$ , and vector  $\omega$  are produced by the relativistic nucleon sources. The Lagrangian density describing their dynamics is taken to be the standard nonlinear  $\sigma$ - $\omega$  model of Walecka [1,2]. The total Lagrangian density  $\mathcal{L}$  with minimal coupling is composed of three terms:

- a) the free baryonic ( $\mathcal{L}_{\mathcal{B}}^{\text{free}}$ ),
- b) the free mesonic ( $\mathcal{L}_{\mathcal{M}}^{\text{free}}$ ), and
- c) the interaction ( $\mathcal{L}_{\mathcal{B}\mathcal{M}}^{\text{interac}}$ ):

$$\mathcal{L} = \mathcal{L}_{\mathcal{B}}^{\text{free}} + \mathcal{L}_{\mathcal{M}}^{\text{free}} + \mathcal{L}_{\mathcal{B}\mathcal{M}}^{\text{interac}}. \quad (9)$$

These are given by

$$\mathcal{L}_{\mathcal{B}}^{\text{free}} = \bar{\psi}_i (i\gamma^\mu \partial_\mu - M) \psi_i, \quad (10)$$

$$\begin{aligned} \mathcal{L}_{\mathcal{M}}^{\text{free}} = & -\frac{1}{2}\partial^\mu\sigma\partial_\mu\sigma - U(\sigma) - \frac{1}{4}\mathbf{\Omega}^{\mu\nu}\mathbf{\Omega}_{\mu\nu} + \frac{1}{2}m_\omega^2\omega^\mu\omega_\mu + \frac{1}{4}g_4(\omega^\mu\omega_\mu)^2 - \\ & - \frac{1}{4}\mathbf{R}^{\mu\nu}\mathbf{R}_{\mu\nu} + \frac{1}{2}m_\rho^2\rho^\mu\rho_\mu - \frac{1}{4}F^{\mu\nu}F_{\mu\nu} \end{aligned} \quad (11)$$

and the interaction term is taken to be

$$\begin{aligned} \mathcal{L}_{\mathcal{B}\mathcal{M}}^{\text{interac}} = & -g_\sigma\bar{\psi}_i\psi_i\sigma - g_\omega\bar{\psi}_i\gamma^\mu\psi_i\omega_\mu - g_\rho\bar{\psi}_i\gamma^\mu\boldsymbol{\tau}\psi_i\boldsymbol{\rho}_\mu - \\ & - e\bar{\psi}_i\gamma^\mu\frac{(1+\tau_3)}{2}\psi_iA_\mu. \end{aligned} \quad (12)$$

The nucleons are assumed to be embedded in the self-interacting  $\sigma$ -meson potential having the cubic and quartic terms given by [59]:

$$U(\sigma) = \frac{1}{2}m_\sigma\sigma^2 + \frac{1}{3}g_2\sigma^3 + \frac{1}{4}g_3\sigma^4. \quad (13)$$

In the above equations,  $M$  stands for the nucleon mass, the symbols  $m_\sigma$  ( $g_\sigma$ ),  $m_\omega$  ( $g_\omega$ ),  $m_\rho$  ( $g_\rho$ ) are meson masses (coupling constants);  $g_2$  and  $g_3$  are the coupling constants for the cubic and quartic self-interaction terms for the  $\sigma$  field [59];  $g_4$  is the coupling constant for the quartic self-interaction term for the  $\omega$  field;  $\frac{e^2}{4\pi} = \frac{1}{137}$  is the coupling constant for the photon;  $\boldsymbol{\tau}$  ( $\tau_3$ ) denotes isotopic spin (third component of  $\boldsymbol{\tau}$ ) for the nucleon spinor ( $\tau_3$  is  $-1$  for a neutron and  $+1$  for proton). The isovector vector field  $\boldsymbol{\rho}^\mu$  is a four-vector in Minkowski's space and a three-vector in the isospin space. It allows one to adjust isovector properties in the nucleus.

The field tensors  $\mathbf{\Omega}^{\mu\nu}$ ,  $\mathbf{R}^{\mu\nu}$  corresponding to the  $\omega$  and  $\rho$  mesons and the tensor  $F^{\mu\nu}$  corresponding to the electromagnetic field, appearing in the Lagrangian, are given by

$$\mathbf{\Omega}^{\mu\nu} = \partial^\mu\omega^\nu - \partial^\nu\omega^\mu, \quad (14)$$

$$\mathbf{R}^{\mu\nu} = \partial^\mu\rho^\nu - \partial^\nu\rho^\mu, \quad (15)$$

$$F^{\mu\nu} = \partial^\mu A^\nu - \partial^\nu A^\mu. \quad (16)$$

The isovector quantities are indicated by overhead arrows.

The nuclear many-body wave function is taken to be a Slater determinant of Dirac spinors. Since the exchange contributions are neglected, the Hartree approximation is implied in the nucleon sector. The variational approach then leads to the Dirac-type equation with potential terms for the nucleons and Klein–Gordon-type equations with the sources involving nucleon moments and currents for the classical meson fields. This set of coupled nonlinear differential equations, known as the RMF equations, is to be solved self-consistently.

Application of the classical Euler–Lagrange variational principle to the total Lagrangian gives the equations of motion. To simplify the resulting equations of motion, a number of further conditions are imposed. For example, the contribution from the antiparticles is neglected (no-sea approximation). Only the static solutions of the equations are sought. Time reversal symmetry is imposed. This makes the space-like components of the fields disappear. Due to charge conservation, only the 3-component of the isovector  $\rho$  survives. The simplified equations of motion thus obtained are given by [6]

$$\left(-i\boldsymbol{\alpha} \cdot \boldsymbol{\nabla} + \beta(M + g_\sigma\sigma) + g_\omega\omega^0 + g_\rho\tau_3\rho_3^0 + e\frac{1+\tau_3}{2}A^0\right)\psi_i = \epsilon_i\psi_i \quad (17)$$

for the nucleon. Here  $M$  is the nucleon mass and  $\sigma$ ,  $\omega^0$ ,  $\rho_3^0$ , and  $A^0$  are the meson and electromagnetic fields. These fields are to be determined self-consistently from the Klein–Gordon equations for the mesons and photon:

$$\{-\nabla^2 + m_\sigma^2\}\sigma = -g_\sigma\rho_s - g_2\sigma^2 - g_3\sigma^3, \quad (18)$$

$$\{-\nabla^2 + m_\omega^2\}\omega^0 = g_\omega\rho_v + g_4(\omega^0)^3, \quad (19)$$

$$\{-\nabla^2 + m_\rho^2\}\rho_3^0 = g_\rho\rho_3, \quad (20)$$

$$-\nabla^2 A^0 = e\rho_c. \quad (21)$$

The source terms (nuclear currents and densities) appearing in the above equations are given by [6]

$$\rho_s = \sum_i n_i \bar{\psi}_i \psi_i, \quad (22)$$

$$\rho_v = \sum_i n_i \psi_i^\dagger \psi_i, \quad (23)$$

$$\rho_3 = \sum_i n_i \psi_i^\dagger \tau_3 \psi_i, \quad (24)$$

$$\rho_c = \sum_i n_i \psi_i^\dagger \left(\frac{1+\tau_3}{2}\right) \psi_i. \quad (25)$$

In practical calculations, the sum in these equations is taken only over the positive energy states (no-sea approximation).

The occupation probabilities  $n_i$  for the state  $i$ , in the absence of pairing is given by:

$$\begin{aligned} n_i &= 1 \text{ for } \epsilon_i \leq \epsilon_f; \\ &= 0 \text{ for } \epsilon_i > \epsilon_f. \end{aligned}$$

Here,  $\epsilon_i$  is the single particle energy of the state  $i$ , and  $\epsilon_f$  is the Fermi energy. In the case of simple BCS prescription of pairing, the occupation probability  $n_i$  reads:

$$n_i = v_i^2 = \frac{1}{2} \left[ 1 - \frac{\epsilon_i - \lambda}{\sqrt{(\epsilon_i - \lambda)^2 + \Delta^2}} \right]. \quad (26)$$

In practical calculations, one imposes further spherical or cylindrical symmetries. In the case of the spherical symmetry, the sources (Eqs. (22)–(25)) appearing in the Klein–Gordon (KG) equations (Eqs. (18)–(21)) take particularly simple forms:

$$\rho_s = \sum_i n_i (2j_i + 1) (f_i^2 - g_i^2), \quad (27)$$

$$\rho_v = \sum_i n_i (2j_i + 1) (f_i^2 + g_i^2), \quad (28)$$

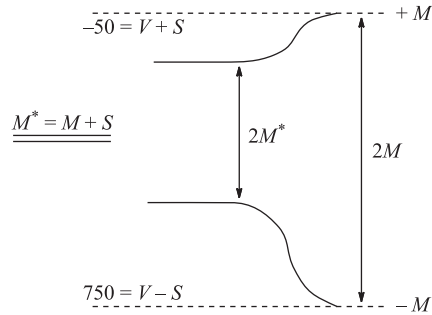
$$\rho_3 = \sum_i n_i (2j_i + 1) \tau_i (f_i^2 + g_i^2), \quad (29)$$

$$\rho_c = \sum_i n_i \left( \frac{1 + \tau_i}{2} \right) (f_i^2 + g_i^2), \quad (30)$$

where,  $f$  and  $g$  are the upper and lower components of the Dirac spinor.

The saturation mechanism is built-in in this relativistic formulation, Fig. 2. This can be readily demonstrated, particularly, with regard to the spherically symmetric case. A glance on any standard Lagrangian parameter set (see, for example, Table 2 in the next section) reveals that  $m_\sigma$ ,  $m_\omega$  are large. Ignoring the Laplacian in the KG equation, the fields are found to be proportional to the corresponding densities, that is,

$$\begin{aligned} \sigma &\propto \rho_s, \\ \omega &\propto \rho_v. \end{aligned}$$



For collapse,  $2M^*$  shrinks, i.e.,  $S$  becomes large. On the other hand, small components  $|g|^2$  become large.

Thus, if  $|g|^2$  becomes large,  $\rho_s$  becomes small. As  $\rho_s$  is the source of  $\sigma$ , i.e.,  $S$  makes automatically  $\sigma$  or  $S$  smaller. This is the mechanism (of preventing collapse) of saturation in the relativistic Hartree.

Fig. 2. Saturation mechanism in the relativistic Hartree formulation

**1.1. Relativistic Hartree–Bogoliubov Theory.** The pairing correlations are important for the open-shell nuclei. These can be incorporated either by using simple BCS prescription (constant gap) or self-consistently through the Bogoliubov transformation. The latter leads to the RHB equations, they are given by [8, 10]:

$$\begin{pmatrix} h_D - \lambda & \hat{\Delta} \\ -\hat{\Delta}^* & -h_D^* + \lambda \end{pmatrix} \begin{pmatrix} U \\ V \end{pmatrix}_k = E_k \begin{pmatrix} U \\ V \end{pmatrix}_k. \quad (31)$$

Here,  $\lambda$  is the Lagrange multiplier;  $E_k$  is the quasiparticle energy, and  $U_k$  and  $V_k$  are normalized four-dimensional Dirac super spinors,

$$\int (U_k^\dagger U_{k'} + V_k^\dagger V_{k'}) = \delta_{kk'}; \quad (32)$$

$h_D$  is the usual Dirac Hamiltonian (see [8]) given by,

$$h_D = -i\alpha \cdot \nabla + \beta(M + g_\sigma \sigma) + g_\omega \omega^0 + g_\rho \tau_3 \rho_3^0 + e \frac{1 + \tau_3}{2} A^0. \quad (33)$$

Here  $M$  is the nucleon mass, and  $\sigma$ ,  $\omega^0$ ,  $\rho_3^0$ , and  $A^0$  are the meson and e.m. fields. These fields are to be determined self-consistently from the Klein–Gordon equations (Eqs. (18)–(21)), with new sources (currents and densities) in terms of the Dirac super spinors [8, 10]:

$$\rho_s = \sum_{E_k > 0} V_k^\dagger \gamma^0 V_k, \quad (34)$$

$$\rho_v = \sum_{E_k > 0} V_k^\dagger V_k, \quad (35)$$

$$\rho_3 = \sum_{E_k > 0} V_k^\dagger \tau_3 V_k, \quad (36)$$

$$\rho_c = \sum_{E_k > 0} V_k^\dagger \frac{1 + \tau_3}{2} V_k. \quad (37)$$

In practical calculations of the sources (nucleon currents and moments), the sum is restricted, as before, only to the positive energy states (no-sea approximation).

The RHB equations have two distinct parts: the self-consistent field ( $h_D$ ) that describes the long range particle-hole correlations and the pairing field ( $\hat{\Delta}$ ) that accounts for the correlations in the particle–particle ( $pp$ ) channel. In the coordinate space representation, the kernel of the pairing field  $\hat{\Delta}$  is given by

$$\Delta_{ab}(\mathbf{r}, \mathbf{r}') = \frac{1}{2} \sum_{c,d} V_{abcd}^{pp}(\mathbf{r}, \mathbf{r}') \kappa_{cd}(\mathbf{r}, \mathbf{r}'), \quad (38)$$

where the roman symbols  $a, b, c, d$  denote all the single-particle state quantum numbers;  $V_{abcd}^{pp}(\mathbf{r}, \mathbf{r}')$  are the matrix elements of the two-body nuclear potential in the  $pp$  channel. The pairing tensor is given by

$$\kappa_{cd}(\mathbf{r}, \mathbf{r}') = \sum_{E_k > 0} U_{ck}^*(\mathbf{r}) V_{dk}(\mathbf{r}'). \quad (39)$$

The integral operator  $\hat{\Delta}$  acts on  $V_k(\mathbf{r})$ ,

$$\hat{\Delta}_a(V_k(\mathbf{r})) = \sum_b \int d^3r' \Delta_{ab}(\mathbf{r}, \mathbf{r}') V_{bk}(\mathbf{r}'). \quad (40)$$

Reliable and satisfactory derivation of  $V_{abcd}^{pp}$  is not yet available in RMF (see [8, 10]). Guided by the success of the nonrelativistic Hartree–Fock–Bogoliubov (HFB) investigations with phenomenological finite or effective zero range Gogny-type interaction in the  $pp$  channel and in the absence of the field theoretic derivation of  $V_{abcd}^{pp}$  in the RMF, one adopts a phenomenological approach while solving the RHB equations employing the finite range Gogny interaction [60, 61]. Alternatively, the density-dependent effective two-body zero-range interaction [62] is also employed for this purpose.

In the case of the constant gap,  $\hat{\Delta}_a (\equiv \Delta)$  becomes diagonal, resulting in the BCS-type expressions for the occupation probabilities [6, 8] (Eq. (26)). As a result, the RHB equations (Eq. (31)) reduce to the RMF equations with the constant gap.

Next we present and discuss the results obtained by using different techniques for the solution of RMF/RHB equations.

## 2. DETAILS OF THE CALCULATIONS

The explicit RMF/RHB calculations require the following input information:

- parameters appearing in the Lagrangian,
- $V^{pp}$  or the gap parameters  $\Delta$  for calculation of  $v_k^2$ .

The RMF/RHB calculations yield the following results: the fields ( $\sigma, \omega^0, \rho_3^0$ , and  $A^0$ ), the nucleon spinors ( $\Psi_i$ ), the single particle energies ( $\varepsilon_i$ ), the occupancies, root-mean-square radii, densities, nucleon currents, moments, and total binding energy, etc.

In this work, the RMF/RHB equations are solved either using the basis expansion method or in the coordinate space (c). Explicitly:

1. We first use the oscillator basis (ob) for the numerical solution of RMF equations (with constant gap) and also for RHB equations with finite range Gogny

D1S interaction. The corresponding results are denoted by SPH and RHB(ob), respectively. The phenomenological Gogny D1S interaction is given by [60,61]:

$$V(\mathbf{r}_1, \mathbf{r}_2) = \sum_{i=1,2} e^{-\{(\mathbf{r}_1 - \mathbf{r}_2)/\mu_i\}^2} (W_i + B_i P^\sigma - H_i P^\tau - M_i P^\sigma P^\tau). \quad (41)$$

Table 1. Gogny D1S parameters

$i$	$\mu_i$	$W_i$	$B_i$	$H_i$	$M_i$
1	0.7	-1720.30	1300.00	-1813.53	1397.60
2	1.2	103.64	-163.48	162.81	-223.93

Factors  $\mu_i$ ,  $W_i$ ,  $B_i$ ,  $H_i$ , and  $M_i$  ( $i = 1, 2$ ) are parameters of the interaction. These are listed in Table 1.

The differences between the SPH and the corresponding RHB(ob) results will be solely due to the treatment of pairing (constant gap and Bogoliubov).

2. Next we solve the RHB equations with zero-range density-dependent two-body interaction [62] in the coordinate space. This interaction is expressed as [62]:

$$V(\mathbf{r}_1, \mathbf{r}_2) = V_0 \delta(\mathbf{r}_1 - \mathbf{r}_2) \frac{1}{4} (1 - \sigma_1 \sigma_2) \left( 1 - \frac{\rho(r)}{\rho_0} \right), \quad (42)$$

here,  $V_0$  is the interaction strength, and  $\rho_0$  ( $= 0.152 \text{ fm}^{-3}$  [62]) is the nuclear matter density. The strength  $V_0$  is fixed so as to reproduce the pairing energy [62] obtained from the finite range Gogny D1S interaction.

The results obtained by solving RHB equations in coordinate space are denoted by RHB(c). The differences between the RHB(ob) and the corresponding RHB(c) results will reflect the importance of incorporating the correct asymptotics.

For explicit numerical calculations, we use the box size of 25 fm for the solution of the RHB equations in the coordinate space. The variation of the box size ( $\pm 10$  fm) marginally affects the results. For example, the binding energies, on an average, change by only 0.02%, the radii differ only in the third decimal place of fermi, whereas the peripheral factors change by less than 1%. The value of  $V_0$  obtained by reproducing the pairing energy resulting from the use of Gogny D1S interaction in RHB(ob) lies between 700 and 800  $\text{MeV} \cdot \text{fm}^{-3}$ . It is further observed that a variation in  $V_0$  by  $\pm 50 \text{ MeV} \cdot \text{fm}^{-3}$  hardly affects the radii, binding energies, and the peripheral factors.

3. To ascertain the effect of deformation the RMF equations with the constant gap approximation are solved in the deformed oscillator basis with axial symmetry (the corresponding results are denoted by DEF). The differences between the SPH and the corresponding DEF results will reflect the importance of deformation.

Numerical calculations require the parameters appearing in the Lagrangian and the gap parameters  $\Delta$  or  $V^{pp}$  as input. Several parameter sets for the Lagrangian density are available. Usually, the Lagrangian parameters are not

derived, but are determined phenomenologically by fitting the nuclear matter properties and the ground state properties of a few selected spherical nuclei, e.g.,  $^{16}\text{O}$ ,  $^{40}\text{Ca}$ ,  $^{112}\text{Sn}$ , and  $^{208}\text{Pb}$ . These parameters then are frozen and used for the calculation of any nucleus in any part of the periodic table. Here we use the most successful NL3 parameter set [63]. The NL3 set has in all seven parameters ( $M$  and  $m_\rho$  are kept fixed). These are listed in Table 2. The results obtained by using the other successful Lagrangian parameter sets (e.g., NL1 [3,6], NL-SH [64], NL-SV1 [65]) exhibit identical systematics. Therefore, the conclusions/inferences presented here will generally remain valid.

**Table 2. Different sets of the Lagrangian parameters commonly used in the RMF/RHB calculations. The masses are in MeV. All the coupling constants are dimensionless, except the  $g_2$ . The latter is expressed in terms of  $\text{fm}^{-1}$**

Parameterization	$M$	$m_\sigma$	$m_\omega$	$m_\rho$	$g_\sigma$	$g_\omega$	$g_\rho$	$g_2$	$g_3$	$g_4$
NL3	939.0	508.194	782.501	763.0	10.217	12.868	4.474	-10.431	-28.885	0.0

In the constant gap approximation for pairing, the neutron (proton) gap parameters  $\Delta_n$  ( $\Delta_p$ ) are obtained from the observed odd–even mass differences [66]. The gap  $\Delta_n$  ( $\Delta_p$ ) is taken to be identically zero for the magic neutron (proton) core and for the one particle (hole) outside (in) this core. This is expected and is also consistent with the RHB results with Gogny D1S pairing interaction in pairing channel. For example,  $\Delta_p$  ( $\Delta_n$ ) calculated from the observed odd–even mass differences is finite for  $Z > 9$  ( $N > 9$ ). The pairing energies obtained with the constant gap with the spherical oscillator basis (SPH) differ in several cases from the corresponding RHB values obtained in the spherical oscillator basis (RHB(ob)) or in the coordinate space (RHB(c)). Also, the use of the constant gaps may yield different occupation probabilities as compared to the corresponding RHB values with the Gogny D1S interaction for pairing. To be consistent with the RHB results, the constant gaps (independent of the particle level) are fixed so that the SPH pairing energy is almost identical to the corresponding RHB(ob) pairing energy. This choice of pairing gaps is shown to be important for describing the observed anomalous behavior in the Neon isotopes [67].

### 3. RMF/RHB RESULTS FOR GROUND STATE PROPERTIES

The comparative study presented here may reveal the level and the extent of differences arising in the physical observables like the binding energies, sizes (neutron and proton radii), densities, etc., arising due to the use of different variants of solving RMF/RHB equations. Extensive calculations have been carried out for such a comparative study. Here, we present and discuss the results of only

a few selected isotopic, isotonic, and isobaric chains, in particular, the isotopic chains of Nitrogen, Neon, Argon, Iron, Cesium, and Radium,  $A = 18$  isobaric and  $N = 12$  isotonic chains.

**3.1. Isotopic Chains.** For the isotopic chains up to Iron, the ground state properties are presented as a function of the third component of isospin ( $T_z = (N - Z)/2$ ). For the other two chains (Cesium and Radium), the binding energies are plotted as a function of mass number. This convention is followed throughout, unless otherwise specified.

**Binding Energies.** The differences between the calculated and corresponding experimental binding energies [66] are plotted in Fig. 3 for these isotopic chains. It is clearly seen that the different prescriptions yield very similar binding energies. The RHB(ob) and RHB(c) results are almost identical, implying that the inclusion of the correct asymptotics (within a spherical box) is not very crucial for the prediction of binding energies. However, it is also seen that SPH and RHB(ob) results though are similar, the differences do exist between them at a finer level. This is probably due to the treatment of pairing. It should be noted that the pairing gaps in SPH calculations have been selected to reproduce the corresponding RHB(ob) pairing energies. Thus, it can be concluded that even the frozen gap approximation leads to reasonable values of binding energies, provided the pairing gaps are appropriately selected. In the case of Nitrogen isotopes, the inclusion of deformation effects has hardly any effect on the calculated binding energies. It is interesting to note that the RMF/RHB calculations yield over-binding near the drip lines. In fact, a similar observation holds for all the isotopic chains in the low mass region. This indicates the need for fine tuning the Lagrangian for large positive isospins. It may also imply that the correct coupling between the continuum and the levels below the Fermi surface is important, especially for the high isospin, or the neutron-rich nuclei. This observation is absent for the case of the neutron deficient nuclei. In the case of the Neon isotopes, however, the inclusion of deformation does improve binding energies near  $N = Z$  region, where most of the nuclei in this chain are strongly deformed. Again, on the neutron-rich side over-binding is observed. The Argon chain, on the other hand, exhibits a slightly different behavior. These isotopes turn out to have milder deformations. The binding energies are not altered significantly due to deformations, except for the nuclei in the neighborhood of  $N = Z$ . The inclusion of deformation has, however, significant effect in the case of Iron isotopes. Except for  $^{54}\text{Fe}$ , which turns out to be spherical, everywhere else, the inclusion of deformation brings the calculated binding energies closer to the experiment.

For the Cesium chain, the deformation has a dramatic effect. The binding energies are improved considerably in this case. The nuclei here tend to get over-bound near the neutron shell closure ( $^{137}\text{Cs}$ ). Similar remarks hold for the Radium chain. There is a clear over-binding near the neutron shell closure,  $^{214}\text{Ra}$ . For the heavier Radium isotopes (beyond  $^{224}\text{Ra}$ ), the inclusion of deformation

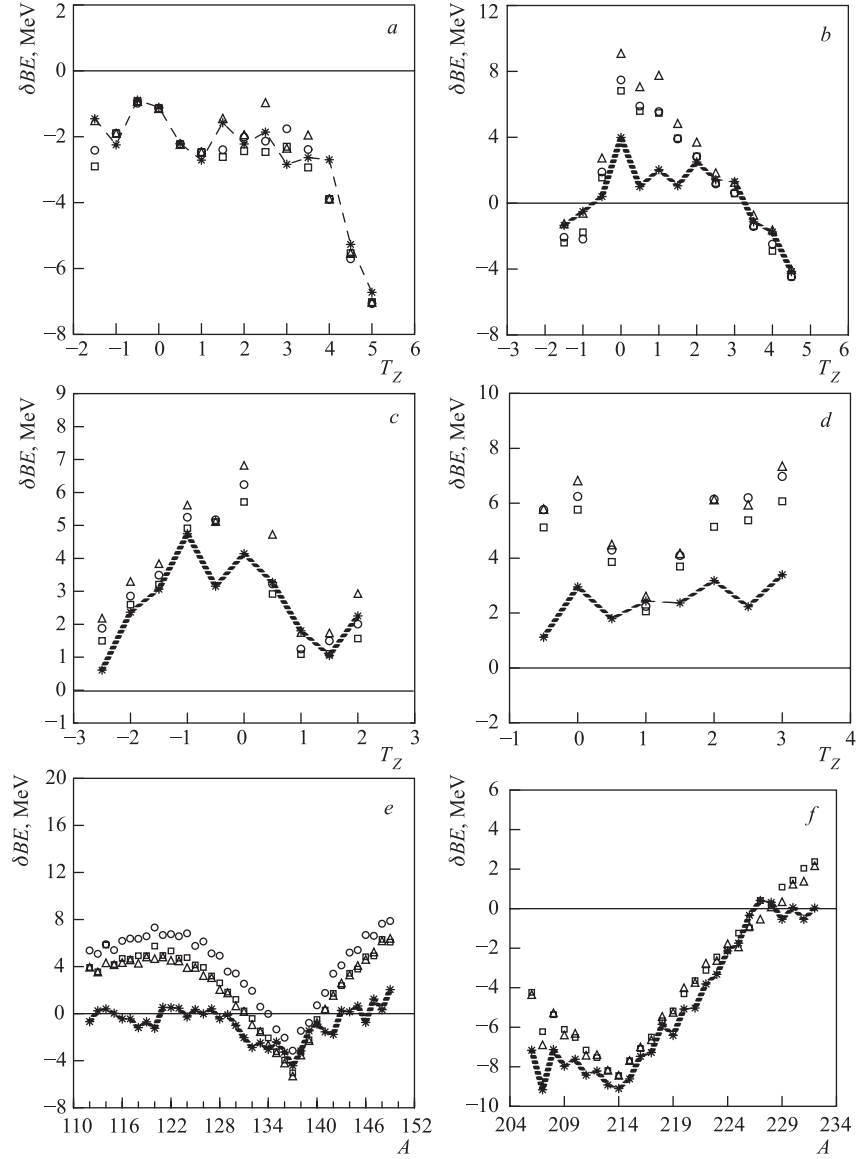


Fig. 3. The binding differences between the results obtained by different prescriptions of solving the RMF/RHB equations and the corresponding experimental values [66] for N (a), Ne (b), Ar (c), Fe (d), Cs (e), and Ra (f) chains:  $\circ$  — RHB(c);  $\square$  — RHB(ob);  $\triangle$  — SPH; \*, dashed lines — DEF

clearly improves the agreement between the calculated binding energies and the experiment.

Thus, the inclusion of deformation improves the calculated binding energies significantly for nuclei with  $Z > 8$ , especially for  $N = Z$  and neighboring isotopes. However, for the nuclei far away from the line of stability, the differences between the theory and the corresponding experiment are relatively larger. This may indicate inadequacy of the isospin dependence in the current ansatz of the Lagrangian density.

The RHB(ob) and RHB(c) results are almost identical. The SPH and RHB(ob) results are usually similar to each other. Thus, from here onward, it will suffice to present and discuss the RHB(c) and DEF results only. The only exception is the Radium chain, where the calculations in the coordinate space (RHB(c)) are not as reliable. Hence, for this case, we shall present and discuss RHB(ob) and DEF results. We close this section with a remark that overall the RMF/RHB results agree well with the corresponding experiment, but significant departures are clearly seen for the nuclei with high  $T_z$ . This is probably due to centre-of-mass motion and/or due to possible inadequacy of the isospin dependence in the Lagrangian density used. Further, the deformation effects are important for binding energies.

**Deformations.** Deformation is a measure of departure from sphericity. Conceptually, the quadrupole deformation parameter  $\beta$  is a quantitative measure of the deformation of the nucleus. It is related to the quadrupole moment. In practice,  $\beta$  is extracted from the proton ( $Q_p$ ) and neutron ( $Q_n$ ) quadrupole moments through:

$$Q = Q_n + Q_p = \sqrt{\frac{16\pi}{5}} \frac{3}{4\pi} AR_0^2 \beta, \quad (43)$$

with  $R_0 = 1.2A^{1/3}$ .

The calculated (DEF)  $\beta$  for isotopic chains are shown in Fig. 4. The  $\beta$  values shown here correspond to the lowest solution obtained in the DEF calculations. The corresponding Möller–Nix (MN) [68] values are also shown (where available) for comparison. In general, DEF and MN agree well with each other. The overall systematics of the deformation parameters is as expected.

Most of the Nitrogen isotopes turn out to be deformed. Exceptions are  $^{13,14,15}\text{N}$ . Interestingly, the most neutron-rich isotopes have relatively milder deformations. For  $^{17,18,19,21}\text{N}$  additional solutions, close to the minimum solutions are found to exist. These additional solutions are just a few hundred keV higher than the minimum solution. This may indicate shape co-existence in these cases. These solutions are indicated in the figure by unconnected stars.

The variation in  $\beta$  for Neon isotopes is as expected and is in accordance with the trend obtained by Möller and Nix [68]. Here also, the most neutron-rich iso-

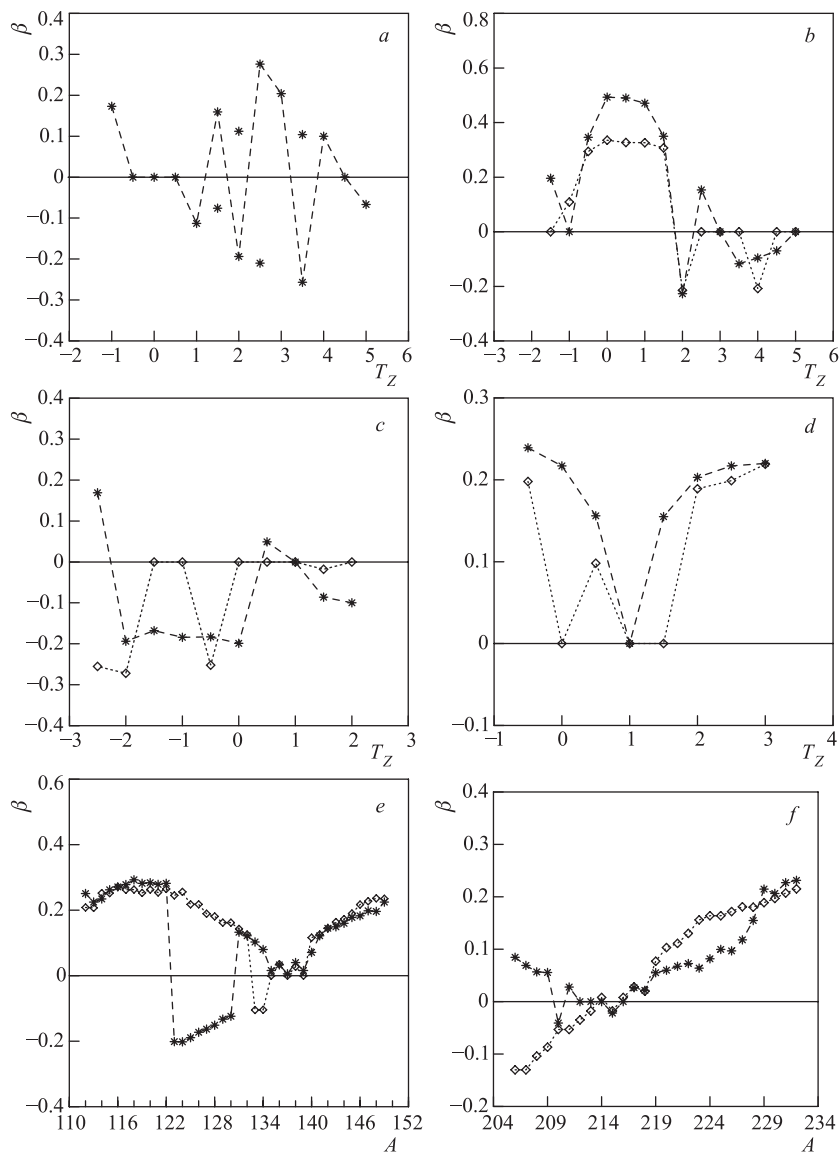


Fig. 4. The calculated quadrupole deformation parameter  $\beta$  (\*, dashed lines) for N (a), Ne (b), Ar (c), Fe (d), Cs (e), and Ra (f) chains. The corresponding Möller-Nix ( $\diamond$ , dotted lines) [68] values are also shown (where available)

topes turn out to have milder deformations. The Neon isotopes close to  $N = Z$  are found to have strong prolate deformations. The present calculation indicates shape transition between  $^{22}\text{Ne}$  and  $^{23}\text{Ne}$ , which is in accordance with that of Möller–Nix. It turns out that all the  $N = Z$  nuclei in this low mass region are prolate, with the only exception of  $^{16}\text{O}$  and  $^{18}\text{F}$ . The calculated deformation parameter  $\beta$  for the Argon isotopes seems to be reasonable. It should be noted that all the Argon isotopes considered here, except  $^{37,38}\text{Ar}$ , are found to have oblate deformation. However, oblate-to-prolate shape transition is observed from  $^{36}\text{Ar}$  to  $^{37}\text{Ar}$ .

The Iron isotopes are found to have prolate deformation, except for  $^{54}\text{Fe}$  (spherical), which has  $N = 28$  subshell closure. The case of Cesium isotopes is interesting, where all the isotopes except for the nuclei close to  $^{137}\text{Cs}$  (shell closure  $N = 82$ ), turn out to be deformed. Most of these are prolate deformed. The prolate-to-oblate shape transition is observed from  $^{122}\text{Cs}$  to  $^{123}\text{Cs}$  and oblate-to-prolate from  $^{130}\text{Cs}$  to  $^{131}\text{Cs}$ .

The Radium isotopes exhibit a slightly different trend. There is a «valley» of spherical or near spherical nuclei between  $^{209}\text{Ra}$  and  $^{218}\text{Ra}$ . In fact, the rest, except for  $^{227}\text{Ra}$  to  $^{232}\text{Ra}$ , turn out to have only milder deformation ( $< 0.1$ ).

A combined analysis of Figs. 3 and 4 reveals that the agreement between the calculated and the corresponding experimental values of the binding energies improves when the deformation is appreciable. However, as discussed earlier, there are a few exceptions. In conclusion, the inclusion of deformation is important for the ground state properties. This statement will be substantiated further in the study of the neutron/proton radii, especially the isotopic shifts. There it will be seen that the inclusion of deformation is essential for the correct theoretical description of the observed structure in the experimental isotopic shifts for the chains of Neon, Iron, and Cesium isotopes.

**Separation Energies.** The separation energies are crucial observables, since they govern the asymptotics of the nuclear density. Further, the magnitude of the single-particle separation energies reflects the extent of the «exoticity» of the nucleus. An examination of the experimental single-particle separation energies for a chain of isotopes reveals odd–even staggering effect. The calculated single- and two-neutron separation energies ( $S_n$  and  $S_{2n}$ ) obtained from the calculated binding energies are shown in Figs. 5 and 6, along with the corresponding experimental [66] values (where available).

An inspection of Fig. 5 reveals that all the calculations reproduce the experimental values of single-neutron separation energies well. The odd–even staggering is also reproduced. However, the inclusion of deformation brings the calculation closer to the experiment. The separation energies being the difference of two large numbers: the total binding energies of the neighboring nuclei, even a small change in one of the binding energies may make a significant difference to the separation energies. The deformation effects are then even more important

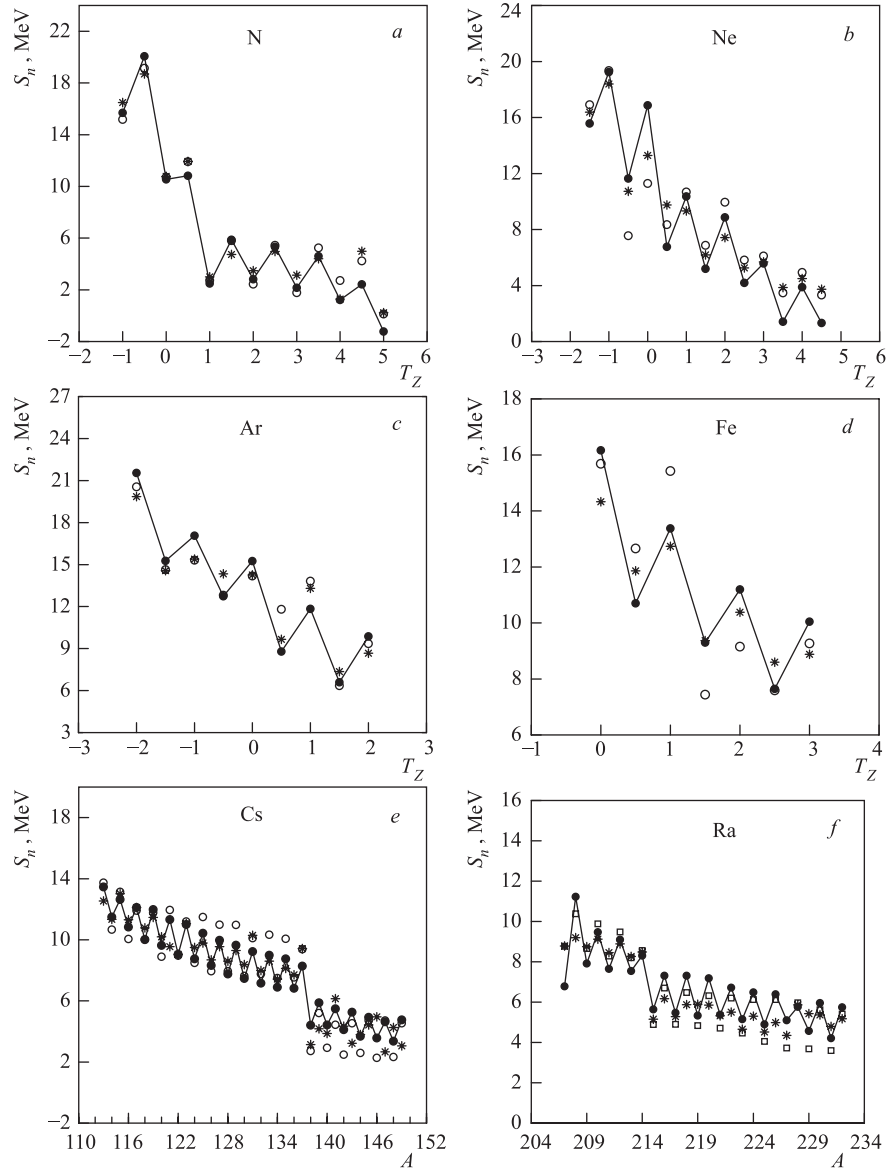


Fig. 5. The calculated single-neutron separation energies ( $S_n$ ) for the isotopic chains considered along with the corresponding experimental values (●, solid lines) [66] (where available). ○ — RHB(c); □ — RHB(ob); \* — DEF

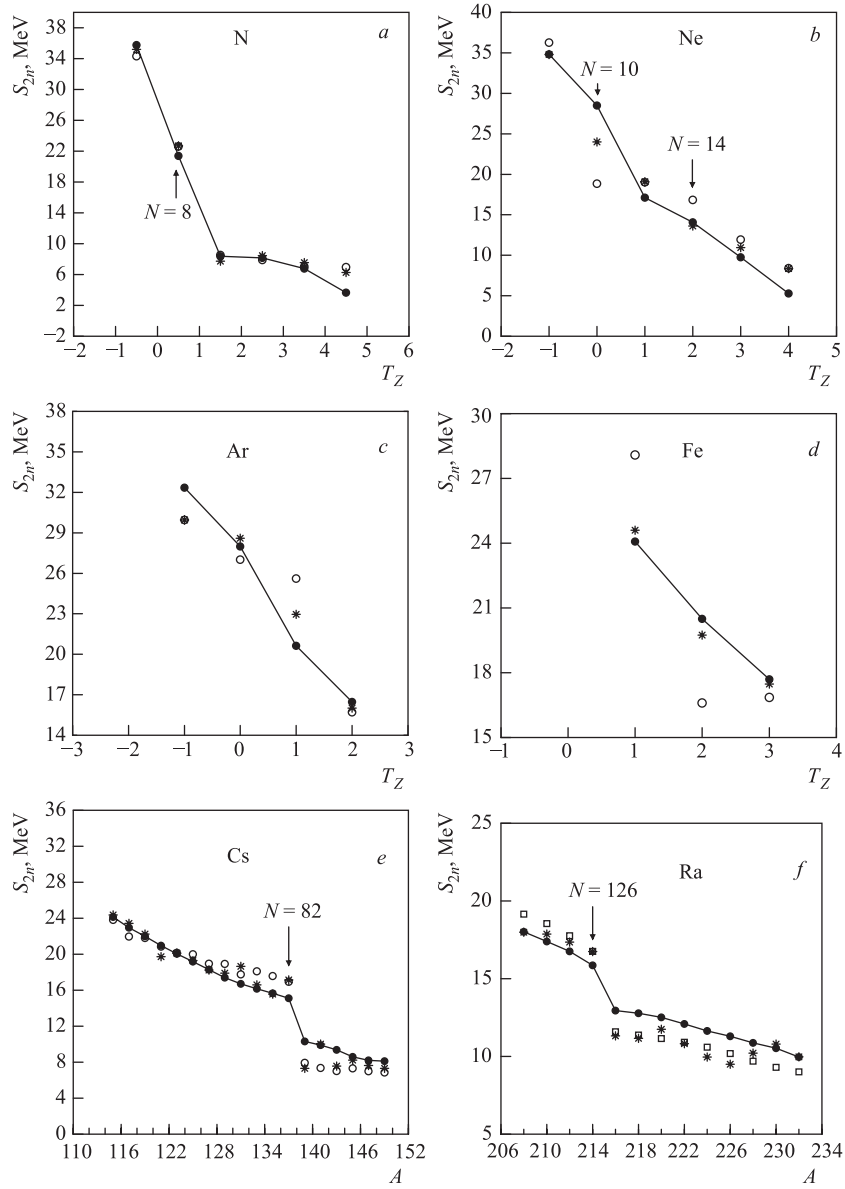


Fig. 6. The calculated two-neutron separation energies for the isotopic chains considered along with the corresponding experimental values (●, solid lines) [66] (where available). ○ — RHB(c); □ — RHB(ob); \* — DEF

for the calculation of separation energies. This is clearly seen in Neon, Iron, and Cesium isotopic chains.

It is known that negative separation energy implies unbound nucleus. The drip line is therefore characterized by the change in the sign of the separation energy. In the present study, we do not intend to make any predictions about the existence of the drip lines. We just intend to comment that, even though the calculated separation energies agree well with the corresponding experiment, small differences do exist between the two, maximum being of the order of 1 MeV. The separation energies near the drip lines are very small, which in turn demands the accurate calculation of the separation energy, better than a few hundred keV, expecting an accuracy of that order in RMF may be rather unreasonable, in the light of the complexity of the problem. Nevertheless, it is gratifying to note that the RMF/RHB yield the binding energies well within 0.25% on the average.

The calculated (RHB(c) and DEF) two-neutron separation energies are shown in Fig. 6 along with the corresponding experimental values [66] (where available). These calculations, indeed, reproduce the experiment well. The deformation effects are seen to be important here also. Two-neutron separation energies reveal the shell effects which in turn give a hint about the stability of the nucleus. If these are constant beyond a certain part of the given isotopic chain, then the corresponding nuclei can probably be regarded as unstable. The shell closures, however, are very clearly seen. These are characterized by a sharp fall in the separation energy. A very sharp fall in the two-neutron separation energy is clearly seen as one goes from  $^{137}\text{Cs}$  to  $^{139}\text{Cs}$ . This is due to the major shell closure at neutron number 82. Similar observations hold for the other isotopic chains. It is to be mentioned that in some of the light nuclei, the conventional magic numbers disappear, and instead, new shell closures appear.

The  $Q$  value for  $\alpha$  (cluster) emission is just the difference between binding energies of parent nucleus and the sum of binding energies of daughter and the alpha (cluster) nucleus. The accurate prediction of  $Q$  for  $\alpha$  (cluster) emission in very heavy and transactinium elements is really crucial, since the decay half-lives depend sensitively on  $Q$  values. Even a difference of few hundred keV may lead to an order of magnitude change in the half-life value. These are presented and discussed in detail for the  $\alpha$ -decay chain of the Superheavy nuclei (Sec. 7).

**Single-Particle Level Spectrum.** Next, the single-particle states are examined. As an illustration, the single-particle level spectrum for the Neon isotopes is presented in Fig. 7. The corresponding fermi energies are shown by dot-dashed lines. The behavior of the energy levels with  $T_z$  is as expected. For  $T_z = -1$  and  $T_z = 3$  ( $^{18,26}\text{Ne}$  resp.) the different  $m$  states for a fixed  $j$  state are degenerate, corresponding to the spherical solutions. The finite deformation ( $\beta$ ) lifts the degeneracy (as expected) in the other isotopes.

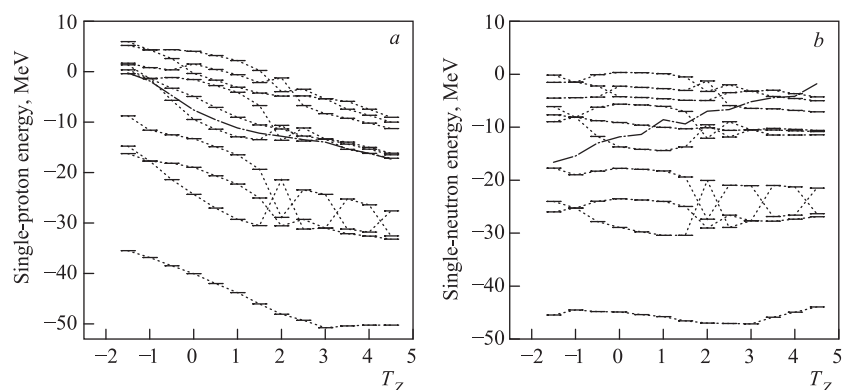


Fig. 7. The calculated DEF single-particle level spectrum for the Neon isotopes. The levels are designated by  $|2j_z|^\pi$  quantum numbers

**Nuclear Radii.** The nuclear radii are the (square root of) second moments of the density distributions. The charge radii of the stable nuclei can be determined accurately by electron scattering experiments. For the nuclei far away from the line of stability, such measurements are difficult due to their short lifetimes. However, with the developments in the field of laser spectroscopy, it has now become possible to measure the isotopic shifts of long chains of isotopes (see [18–21]). These measurements provide rich nuclear-structure information. The neutron radii, on the other hand, are still very difficult to be determined experimentally. One of the aims of the RIB experiments is to estimate the proton/neutron radii and hence the matter radii of the unstable nuclei. But these estimations are highly model-dependent, and we shall refer to them as the «so-called» experimental radii. These are generally obtained through a Glauber model analysis of the total reaction or interaction cross section. Usually, a harmonic oscillator or Woods–Saxon-type density distribution is assumed for the projectile, and the density parameter is tuned so as to reproduce the reaction cross sections [33, 69, 70].

Another interesting and important feature of the loosely bound nuclei is the nuclear skin thickness (defined as difference between the r.m.s. neutron and proton radii). As more and more neutrons are added, the single neutron separation energy goes on decreasing. The neutron density distributions, therefore, spread to larger and larger spatial extent. However, the proton distribution is little affected. The difference between the neutron and proton radii goes on increasing as one moves towards more and more neutron-rich nuclei. The skin thickness, therefore, is a measure of neutron richness or deficiency of the nucleus. It is found that the skin thickness bears a simple relation with the corresponding difference between the single nucleon separation energies.

Next, the charge radii and isotopic shift values are presented.

*Charge Radii.* The charge radii ( $r_c$ ) can be obtained from the calculated point proton root-mean-square radii ( $r_p$ ) through the relation:

$$r_c^2 = r_p^2 + 0.64, \quad (44)$$

where the factor 0.64 accounts for the finite size of proton. These then can be directly compared with the corresponding experimental values. The calculated r.m.s. charge radii ( $r_c$ ) for the chains of Neon, Argon, Iron, and Cesium isotopes are plotted in Fig. 8. The experimental charge radii, determined by either electron scattering or isotopic shift measurements are also shown (wherever available). Clearly, the calculations reproduce the experiment well. All the four figures show that the deformation effects are crucial for describing the observed anomalous behavior (departure from the expected  $r_0 A^{1/3}$  law) of the charge radii.

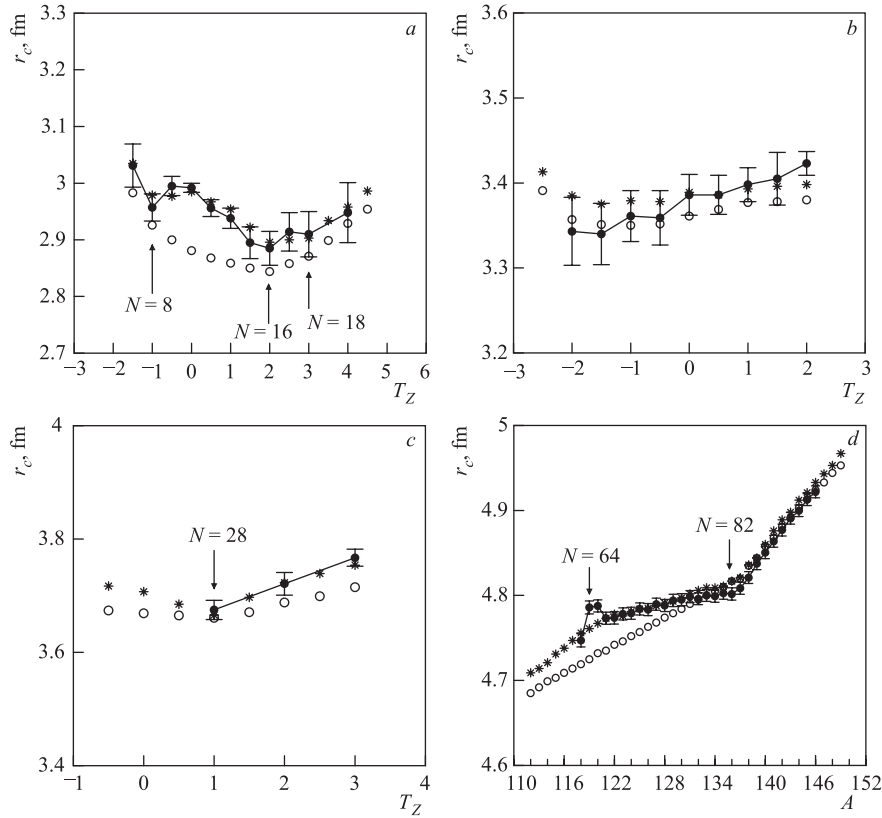


Fig. 8. The calculated and the corresponding experimental charge radii (where available) for the chains of Ne (a), Ar (b), Fe (c), and Cs (d) isotopes.  $\circ$  — RHB(c);  $*$  — DEF;  $\bullet$ , curves — experiments

The charge radii of Neon, deduced from the recent isotopic shift measurements [20] (knowing the charge radius of  $^{20}\text{Ne}$  [71]), exhibit very rich structure. The charge radius is maximum for  $^{28}\text{Ne}$  on the neutron-rich side, and for  $^{17}\text{Ne}$  on the neutron-deficient side. It goes through a minimum at  $^{24}\text{Ne}$ . Thus, with addition or removal of neutrons from  $^{24}\text{Ne}$ , the charge radius is found to *increase*. In addition, a mild odd–even staggering is clearly observed in the neutron-rich as well as deficient isotopes. The calculated (DEF) charge radii are found to be in perfect harmony with the experiment. The anomalous behavior mentioned above is well reproduced. The RHB(c) results, on the other hand, do not reproduce this trend, indicating that the deformation effects are crucial for describing the anomalous behavior.

The isotopic shift measurements have also been reported for the Argon isotopes [72]. These have been measured with respect to  $^{38}\text{Ar}$ , for which no experimental measurement of charge radius is available. However, the electron scattering measurement for  $^{40}\text{Ar}$  is available [71]. Thus, we have deduced the charge radii from the measured isotopic shifts and the known charge radius of  $^{40}\text{Ar}$ . These charge radii turn out to be nearly constant for the entire chain. Both the calculations (RHB(c) and DEF) reproduce this trend. The calculations predict an increase in the charge radius for  $^{31}\text{Ar}$  with respect to  $^{32}\text{Ar}$ , but there is no experimental data available to compare with.

Only a few experimentally determined charge radii are known [71] for the Iron isotopes. The inclusion of the deformation effects is again found (Fig. 8) to be important. A prominent kink is predicted for  $^{54}\text{Fe}$ . There is no experimental data available for comparison. It would be however, interesting to verify this prediction experimentally.

The detailed analysis of the results for Cesium lead to similar conclusions. Extensive experimental data of the laser spectroscopic studies of Cesium isotopes is available in the literature [73]. The charge radii deduced from the measured isotopic shifts [73] and from the known charge radius of  $^{133}\text{Cs}$  [71], have been shown in the figure as experimental radii. It is seen that both the calculations (RHB(c) and DEF) do reproduce the radii rather well. The kink at  $N = 82$  shell closure ( $^{137}\text{Cs}$ ) is well reproduced. Beyond this shell closure, both the RHB(c) and the DEF calculations reproduce the experimental charge radii almost exactly. However, below the shell closure, the DEF results are found to be better than the corresponding RHB(c) results. Thus, the deformation is important for the description of ground state properties. Experimentally, a prominent jump is observed from  $^{121}\text{Cs}$  to  $^{120}\text{Cs}$ . The radius again decreases from  $^{119}\text{Cs}$  to  $^{118}\text{Cs}$ . Though our calculations are very close to the experiment, we do not get this unusual behavior.

Next we study the chain of Radium isotopes. The calculated (RHB(c) and DEF) isotopic shifts for the Radium chain are presented in Fig. 9 along with the corresponding experimental values [19] (where available). Unfortunately, no ex-

perimental charge radius measurement is available for the reference nucleus  $^{214}\text{Ra}$  or any other Radium isotope. Therefore, here we only present the calculated isotopic shifts. The Radium chain is one of the heaviest chains studied by the isotopic shift measurements. It can be clearly seen that RHB(c) as well as DEF results are in perfect harmony with the experimental isotopic shifts [19]. The kink at shell closure  $N = 126$  ( $^{214}\text{Ra}$ ) is well reproduced.

*Matter Radii.* Next we study the matter radii. The r.m.s. matter radii are deduced from the point proton and neutron radii through:

$$r_m^2 = \frac{Zr_p^2 + Nr_n^2}{Z + N}. \quad (45)$$

As mentioned earlier, one of the aims of the RIB reaction cross section measurements is to deduce the r.m.s. radii of the loosely bound projectiles. For almost all the chains in the low mass region (up to Magnesium) these deduced r.m.s. matter radii are available in the literature [33]. Such analysis is also available for Chlorine and Argon isotopes [74]. But, these deduced radii are highly model-dependent. Now we present the matter radii for Nitrogen, Neon, and Argon chains. The results for Fe, Cs, and Ra chains are not included in the view of the absence of the experimental data.

The calculated (RHB(c) and DEF) r.m.s. matter radii for Nitrogen, Neon, and Argon chain are presented in Fig. 10 along with the corresponding so-called experimental matter radii [33,74] (where available). Clearly, the calculated radii are in good agreement with the experiment.

The so-called experimental matter radii for Nitrogen exhibit interesting systematics. There is a prominent dip at  $^{13}\text{N}$ . The  $r_m$  remains nearly a constant up to  $^{17}\text{N}$  and then it increases steadily. There is another slight dip at  $^{21}\text{N}$  and a very sharp rise in the  $r_m$  for  $^{22}\text{N}$  and  $^{23}\text{N}$ , indicating a substantial change in the structure in these two isotopes. The calculations also reproduce the experimental trend. The dip at  $^{13}\text{N}$  is nicely reproduced. Thereafter, it increases monotonically. Overall quantitative agreement between the theory and the corresponding experiment is satisfactory. The deformation does not seem to have any significant effect on the  $r_m$  for this chain.

Experimentally, the charge radii for the Neon chain are known to have very unusual behavior [20]. The matter radii reflect a similar structure [33]. Both

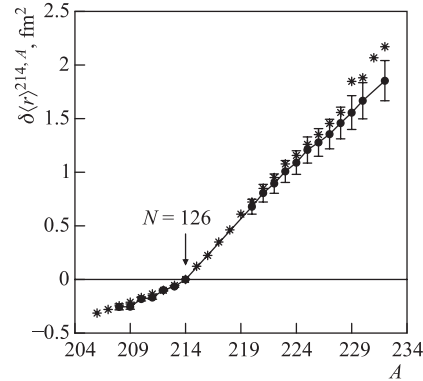


Fig. 9. The calculated (RHB(c) and DEF) isotopic shifts for Radium chain with respect to  $^{214}\text{Ra}$ . The experimental data (●, solid curve) [19] is also included for comparison. \* — RMF

(RHB(c) and DEF) theoretical calculations reproduce the experimental  $r_m$  well, apart from a very prominent dip at  $^{19}\text{Ne}$ . Argon chain, too, has a number of interesting features. A dramatic dip from  $^{31}\text{Ar}$  to  $^{32}\text{Ar}$  and a milder dip for  $^{37,38}\text{Ar}$  are most significant. The calculations, however, predict more or less monotonic increase in  $r_m$ , except for a very slight decrease in  $r_m$  from  $^{31}\text{Ar}$  to  $^{32}\text{Ar}$ .

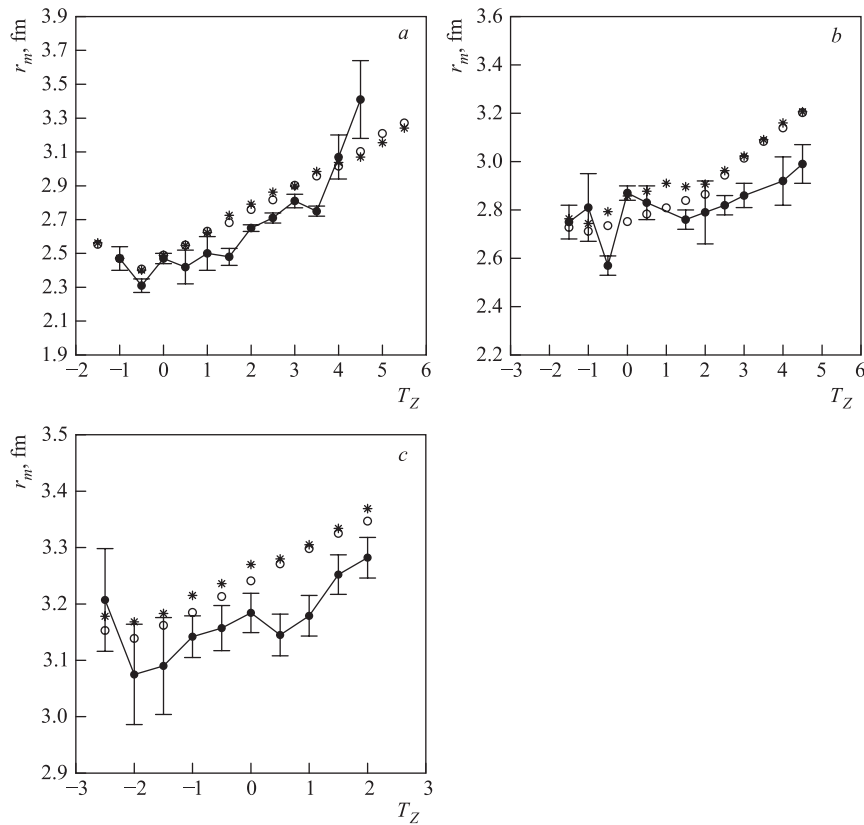


Fig. 10. The calculated and the corresponding so-called experimental [33, 74] r.m.s. matter radii (where available) for the chains of N (a), Ne (b), and Ar (c) isotopes.  $\circ$  — RHB(c); \* — DEF;  $\bullet$ , curves — experiment

To summarize, the calculations reproduce the so-called experimental  $r_m$  well, but, there are minor differences at a few places. The deformation seems to have a marginal effect on the matter radii.

*Nuclear Skin Thickness.* The nuclear skin thickness, defined as the difference between the neutron and proton radii, is an interesting quantity. For all the isotopic chains, the skin thickness is found to increase almost monotonically with the increase in the neutron number. The skin thickness may be related to the corresponding differences between the single-neutron and proton separation energies. Therefore, here, we explore this possibility for all the isotopic chains.

The calculated values of nuclear skin thickness are plotted as a function of the difference between the corresponding single-neutron and proton separation energies in Fig. 11 for all the isotopic chains. An inspection of these figures reveals a strong negative linear correlation between the skin thickness and the separation energy differences. This is true for all the mass regions across the periodic table. To quantify the degree of correlation, we carry out the regression analysis [75]. Accordingly, the correlation coefficient ( $\mathcal{C}$ ) and the slope ( $m$ ) are calculated using the following expressions:

$$\mathcal{C} = \frac{\text{Cov}(x, y)}{\sigma_x \cdot \sigma_y}, \quad (46)$$

where the covariance «Cov» is defined as:

$$\text{Cov}(x, y) = \frac{1}{N-1} \sum_j (x_j - \bar{x})(y_j - \bar{y}), \quad (47)$$

the variance is given by

$$\sigma_z^2 = \frac{1}{N-1} \sum_j (z_j - \bar{z})^2 \quad (z = x \text{ or } y) \quad (48)$$

and

$$m = \frac{\sum_j (x_j - \bar{x})(y_j - \bar{y})}{\sum_j (x_j - \bar{x})^2}. \quad (49)$$

The standard error in the slope is given by

$$e = \frac{\sigma}{\sqrt{N}}, \quad (50)$$

where  $\sigma$  is the standard deviation and  $N$  is the number of observations or the sample points.

The calculated results are presented in Table 3. The correlation coefficients obtained are better than 95% and are negative for these chains. This clearly reveals the strong negative correlation between the nuclear skin thickness and

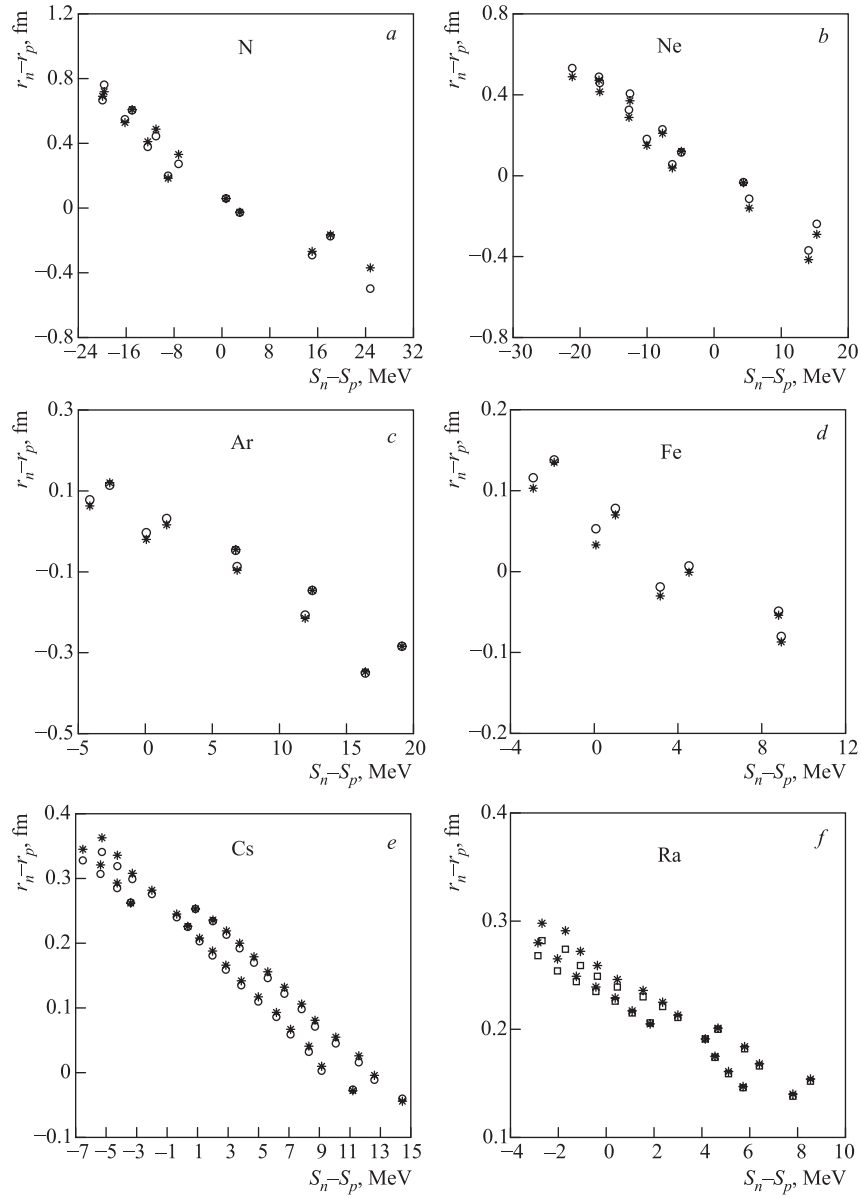


Fig. 11. The variation of the calculated nuclear skin thickness as a function of the corresponding difference between the single neutron and proton separation energies [66].  $\circ$  — RHB(c);  $\square$  — RHB(ob);  $*$  — DEF

Table 3. The calculated correlation coefficients, slope coefficients, and the standard errors

Nuclei	Approximation	$\mathcal{C}$	$m$	$e$	Nuclei	Approximation	$\mathcal{C}$	$m$	$e$
N	RHB(c)	-0.97	-0.026	0.002	Fe	RHB(c)	-0.95	-0.017	0.002
	DEF	-0.97	-0.024	0.002		DEF	-0.93	-0.016	0.003
Ne	RHB(c)	-0.97	-0.028	0.002	Cs	RHB(c)	-0.97	-0.019	0.001
	DEF	-0.99	-0.024	0.001		DEF	-0.97	-0.020	0.001
Ar	RHB(c)	-0.97	-0.017	0.001	Ra	RHB(ob)	-0.96	-0.012	0.001
	DEF	-0.96	-0.016	0.002		DEF	-0.96	-0.013	0.001

the corresponding separation energy differences. Interestingly, the slope of the regression lines turns out to be a weak function of charge number. Approximately, the slope is directly proportional to charge number. To quantify this statement, it is essential to include a large number of data sets. The values of the standard error indicate that there is at most 15% spread about the regression line.

**3.2. Isotonic and Isobaric Chains.** Next we investigate the  $N = 12$  isotonic and  $A = 18$  isobaric chains.

*Binding Energies and Deformations.* To investigate the exact degree of agreement between the theory and the corresponding experiment [66], we plot the difference between the calculated and the corresponding experimental binding energies in Fig. 12. All the prescriptions of solving the RMF/RHB equations are

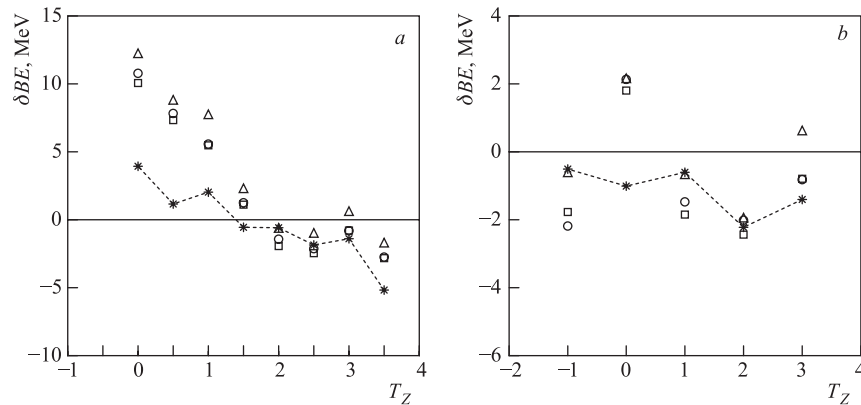


Fig. 12. The difference between the theoretical and experimental [66] binding energies for the  $N = 12$  (a) and  $A = 18$  (b) chains.  $\circ$  — RHB(c);  $\square$  — RHB(ob);  $\triangle$  — SPH; \*, dashed lines — DEF

found to reproduce the experiment well. However, it is clearly seen that the inclusion of deformation does improve the agreement.

Next, we plot the calculated (DEF) deformation parameters for the  $N = 12$  and  $A = 18$  chains along with the corresponding Möller–Nix values [68] (where available) (Fig. 13).

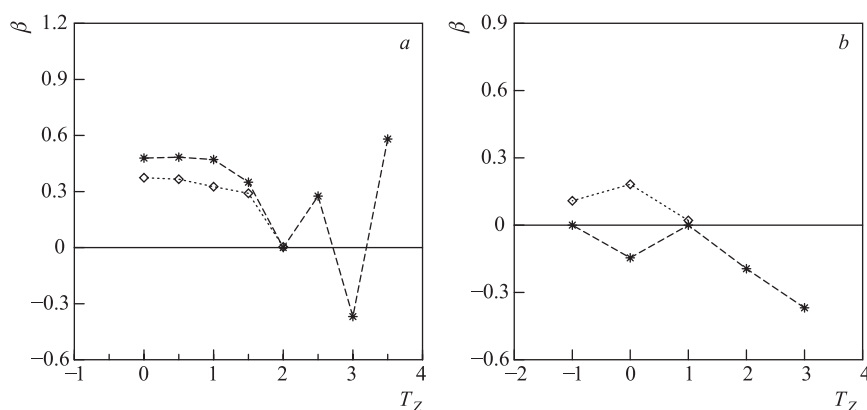


Fig. 13. The calculated (DEF) (\*, dashed lines) and the corresponding Möller–Nix (MN) ( $\diamond$ , dotted lines) [68] deformation parameters for  $N = 12$  (a) and  $A = 18$  (b) chains

The deformation parameters are found to be as expected.  $^{17}\text{B}$  (in  $N = 12$  chain) turns out to have very large deformation ( $\sim 0.6$ ). Another interesting feature clearly seen in  $A = 18$  chain is that there is a mirror symmetry about  $T_z = 0$  ( $^{18}\text{F}$ ). The mirror symmetry in almost all the ground state properties about  $T_z = 0$  has also been observed in  $A = 20$  isobaric chain [76].

*Radii.* The r.m.s. radii are now investigated for  $N = 12$  and  $A = 18$  chains. The calculated and the corresponding experimental charge and matter radii for these chains are presented in Fig. 14. The so-called experimental matter radii have been taken from [33], whereas the charge radii are from [20, 71, 77, 78].

The agreement between the RHB(c) and DEF results and the experiment is found to be excellent. There are some minor differences between the calculated and the corresponding so-called experimental matter radii, but the observed trend is well reproduced. Similar remarks hold for charge radii.

We have seen that in the case of the isotopic chains, the nuclear skin thickness and the corresponding difference between the single-neutron and proton separation energies are strongly correlated. This correlation is found to be true for the isotopic chains across the periodic table. It is therefore interesting to check for this correlation for the isobaric and the isotonic chains. The calculated

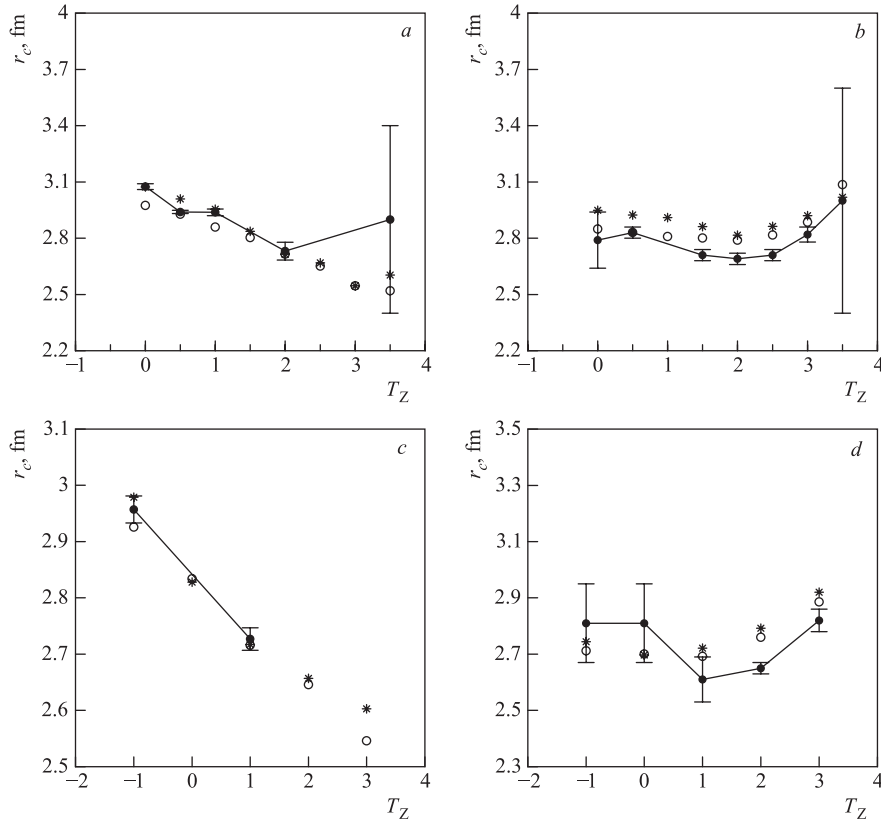


Fig. 14. The variation of the calculated charge and matter radii for  $N = 12$  (a, b) and  $A = 18$  (c, d) chains. The corresponding experimental values (●, solid curves) [20, 71, 77, 78] are also shown (where available). ○ — RHB(c); \* — DEF

skin thickness for the  $N = 12$  and  $A = 18$  chains is plotted as a function of the corresponding difference between the single neutron and proton separation energies [66] in Fig. 15. The strong negative correlation is evident. To quantify the degree of correlation, we again calculate the correlation coefficient and slope of the regression line. The calculated results are presented in Table 4.

Table 4. The calculated correlation coefficients, slope coefficients, and the standard errors

Chains		$\mathcal{C}$	$m$	$e$
$N = 12$	RHB(c)	-0.90	-0.032	0.006
	DEF	-0.94	-0.028	0.004
$A = 18$	RHB(c)	-0.98	-0.024	0.003
	DEF	-0.99	-0.025	0.001

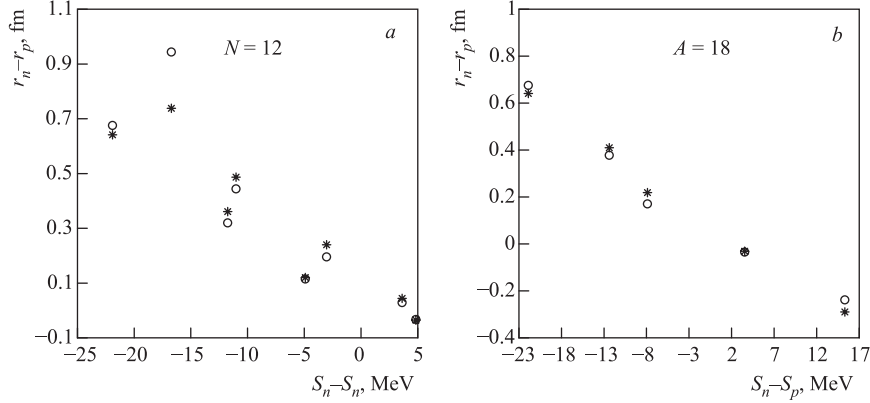


Fig. 15. The variation of calculated skin thickness as a function of the corresponding difference between the single neutron and proton separation energies [66].  $\circ$  — RHB(c);  $*$  — DEF

The negative correlation is amply clear from Table 4, the correlation is better than 90%. The only exception is RHB(c) for  $N = 12$  chain. An inspection of Fig. 15 shows that the RHB(c) skin thickness predicted for  $^{17}\text{B}$  in this chain is too large. If this data point is suppressed, then the correlation coefficient for RHB(c) turns out to be better than 94%. In all these cases, the standard error turns out to be small.

**3.3. Density Distributions.** In order to compare the calculated point proton density distributions with the corresponding experimental densities, the finite proton size is required to be included. As illustrative examples, here we consider  $^{54,56,58}\text{Fe}$ . For this purpose, the  $L = 0$  projected and renormalized proton densities are folded with the Gaussian profile to obtain the charge densities using

$$\rho_c(r) = \frac{1}{(\sqrt{2\pi}\sigma)^3} \int d^3r' \rho_p(r') \exp \left\{ -\frac{(\mathbf{r} - \mathbf{r}')^2}{2\sigma^2} \right\}, \quad (51)$$

where  $\sigma$  is a parameter fixed such that the Gaussian profile has the correct radius (proton radius, 0.8 fm). The motivation behind selecting the Iron isotopes is that for these cases, the model-independent determination (Fourier–Bessel series) of the charge densities is available [71]. The folded point proton densities and the corresponding experimental charge densities [71] are plotted in Fig. 16. Clearly, the calculations reproduce the experiment well. Even the slight depression observed in the interior region of the distribution is well reproduced. Only at a finer level, the DEF densities differ slightly from the corresponding experimental densities. These differences arise only in the peripheral region. Further, the folded and calculated point proton densities noticeably differ from each other primarily in the peripheral region. The experimental densities (Fourier–Bessel) may not be

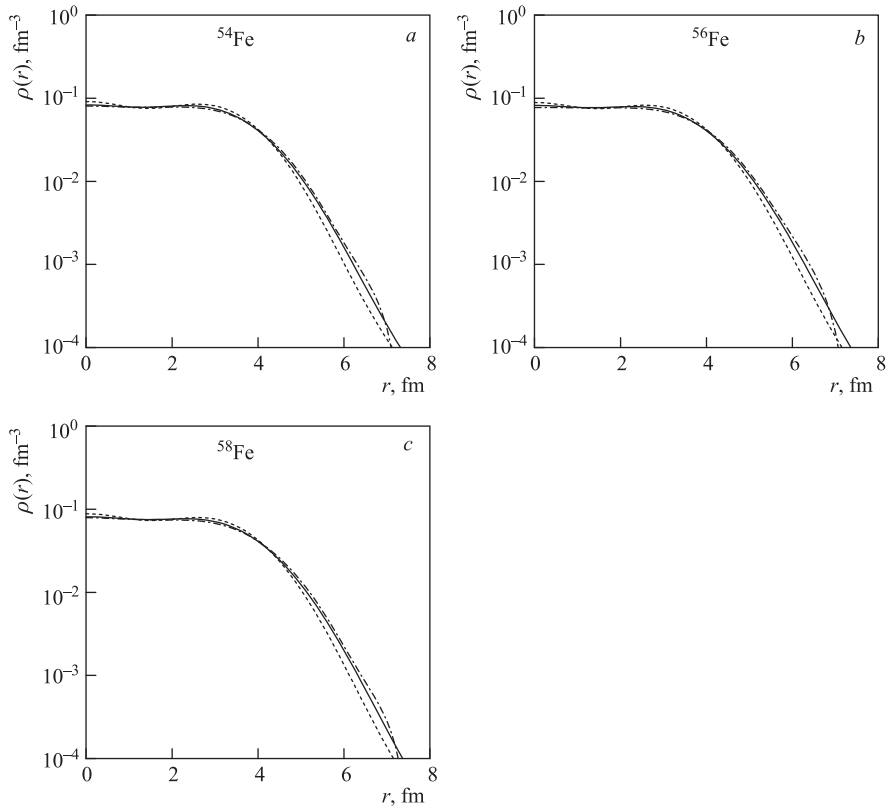


Fig. 16. The calculated ( $\rho_c$ ) (solid curves) and the corresponding experimental (Fourier–Bessel series) (dashed curves) charge densities of  $^{54,56,58}\text{Fe}$ . The point proton densities ( $\rho_p$ ) (dash-dotted curves) are also presented for comparison

as reliable in the far peripheral region.

The effect of folding is expected to be small for the heavier nuclei. To illustrate, the folded and DEF point proton densities of  $^{224}\text{Ra}$  are plotted in Fig. 17. Clearly, the folded and the point proton densities are very similar to each other. Only minor differences between them arise far in the peripheral region.

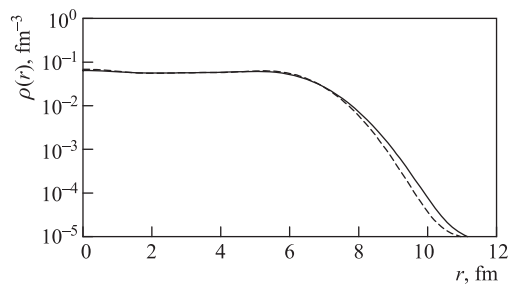


Fig. 17. The calculated charge ( $\rho_c$ ) (solid curve) and the corresponding point proton ( $\rho_p$ ) (dashed curve) densities for  $^{224}\text{Ra}$

Clearly, the RMF/RHB describe remarkably well the observed ground state properties of the nuclei spanning the entire periodic table.

#### 4. ANTIPROTON ANNIHILATION

It has been suggested [28–32] that the antiproton ( $\bar{p}$ ) annihilation in which the energy transferred to the nucleus is negligible can profitably be used to explore the nuclear periphery. When an antiproton is slowed down in the matter to less than 1 keV, an antiprotonic atom may be formed. This then cascades toward nuclear surface by emitting antiprotonic X rays. This cascade terminates when the antiproton encounters a nucleon at the nuclear surface and gets annihilated. Schematically, this is illustrated in Fig. 18.

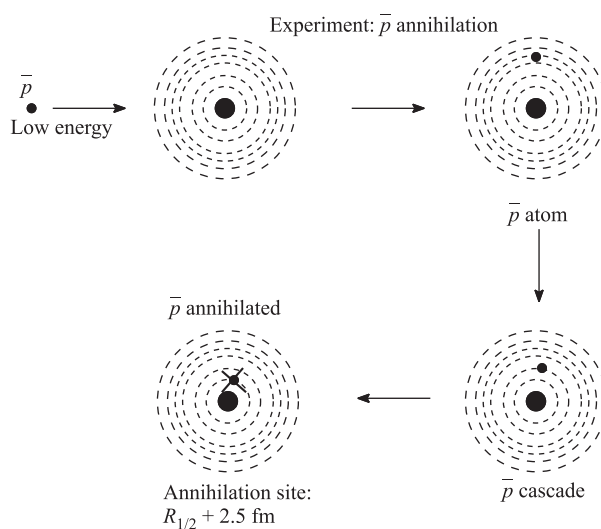
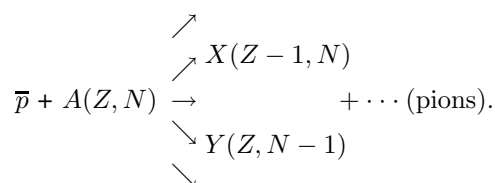


Fig. 18. Schematic representation of the  $\bar{p}$ -annihilation experiment

The process is symbolically represented as:



If the target nucleus  $A(N, Z)$  is selected judiciously such that both the residues  $X(N, Z-1)$  and  $Y(N-1, Z)$  are radioactive, then their relative yields can be measured accurately by standard radiochemical methods.

The so-called experimental peripheral factor  $f_{\text{exp}}^p$  [28, 31]

$$f_{\text{exp}}^p = \frac{N(\bar{p}, n)}{N(\bar{p}, p)} \frac{\text{Im}(a_p)}{\text{Im}(a_n)} \frac{Z}{N} \quad (52)$$

can then be extracted. Here  $N(\bar{p}, n)/N(\bar{p}, p)$  is the measured ratio of the residues  $Y(Z, N - 1)$  and  $X(Z - 1, N)$ ;  $a_n(a_p)$  is the  $\bar{p}$ - $n$  ( $\bar{p}$ - $p$ ) scattering amplitude. The factor  $(\text{Im}(a_n)) / (\text{Im}(a_p))$  accounts for the ratio of annihilation probabilities and in practice it is taken to be 0.63 [28]. In this formula it is assumed that the probabilities of excitation of the deep hole states during the distant annihilation are very small [30].

The peripheral factor is related to the nuclear density

$$f^p = \frac{Z}{N} \frac{\rho_n}{\rho_p}, \quad (53)$$

where  $\rho_p$  ( $\rho_n$ ) is the proton (neutron) density of the parent nucleus at the annihilation site, taken to be  $R_{1/2} + 2.5$  fm [28, 30];  $R_{1/2}$  being the half density radius of the parent nucleus. In recent years antiproton ( $\bar{p}$ ) annihilation experiments have been carried out, enabling one to extract the ratio of neutron to proton densities at the annihilation site (see Eq. (53)). These experiments, therefore, explore the nuclear periphery. In this peripheral region, both the neutron and the proton densities are very small indeed. Therefore, the asymptotics becomes important in the theoretical studies of nuclear densities. Further, the ratio of two very small numbers (neutron and proton densities) imposes a stringent test on the theoretical model used for the calculation of the nuclear densities. Further,  $f^p$  is a ratio of two very small numbers (neutron and proton densities at the annihilation site), therefore, a very small error even in any one of them may result in a large change in the calculated  $f^p$ .

Table 5. The nuclei for which the experimental  $\bar{p}$ -annihilation data are available

<sup>48</sup> Ca	<sup>58</sup> Ni	<sup>96</sup> Zr	<sup>96</sup> Ru	<sup>100</sup> Mo	<sup>104</sup> Ru	<sup>106</sup> Cd	<sup>112</sup> Sn	<sup>116</sup> Cd	<sup>124</sup> Sn
<sup>128</sup> Te	<sup>130</sup> Te	<sup>144</sup> Sm	<sup>148</sup> Nd	<sup>154</sup> Sm	<sup>160</sup> Gd	<sup>176</sup> Yb	<sup>232</sup> Th	<sup>238</sup> U	

We use the RMF approach to study the nuclei for which antiproton annihilation data are available [28–32] (see Table 5). Here, the asymptotics is expected to play a crucial role.

**4.1. Ground State Properties.** *Binding Energies.* For a comparative study of the binding energies obtained by using different methods for solving the RMF/RHB equations, we plot differences in the calculated binding energies and

the corresponding experimental values [66] in Fig. 19. It is evident from the figure that the differences between the binding energies obtained in RHB(c) and RHB(ob) are almost negligible. The binding energies calculated using RMF in spherical oscillator basis in frozen gap approximation (SPH), though very similar to those obtained from RHB(c) and RHB(ob), differ slightly in few cases: maximum deviation being less than 0.4%. The pairing energies in RHB(c) and RHB(ob) are very similar; but these do differ from those obtained from SPH; though the net binding energies are very close to each other, as mentioned before.

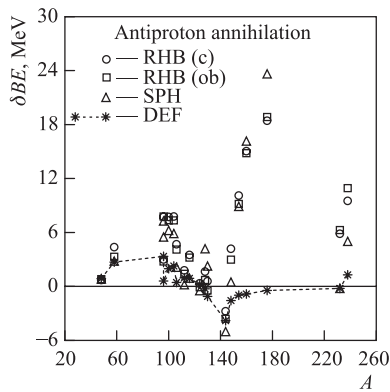


Fig. 19. Difference in the calculated (RMF/RHB) and corresponding experimental [66] binding energies

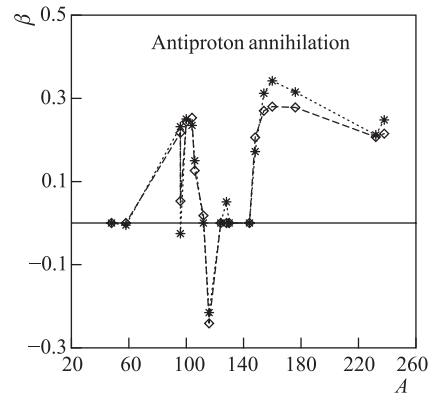


Fig. 20. The calculated deformation parameters  $\beta$  (\*, dotted line). The corresponding results obtained by Möller and Nix ( $\diamond$ , dashed line) [68] are also indicated for comparison

It is noticed that the calculated binding energies substantially differ from the corresponding experimental values only for such cases where the deformation seems to be important. As is seen from Fig. 19, the inclusion of the deformation brings the calculated binding energies (DEF) very close to the experiment. To further illustrate this point, calculated (DEF) deformations ( $\beta$ ) are plotted along with the corresponding values of Möller and Nix [68] in Fig. 20. The calculated (DEF) deformations agree very well with the Möller–Nix values. It is noticed that the effect of deformation to the binding energy is important only for the nuclei where  $\beta$  is large.

To conclude this part, the binding energies calculated by using different procedures for the solution of the relativistic mean field equations are very similar among themselves and also are in overall good agreement with the experiment. The inclusion of deformation brings the calculated binding energies very close to their corresponding experimental values [66].

*Radii.* The calculated values of charge radii ( $r_c$  (fm)) are plotted in Fig. 21 along with the corresponding experimental values [71, 79, 80]. The calculations are found to be in close agreement with the experiment.

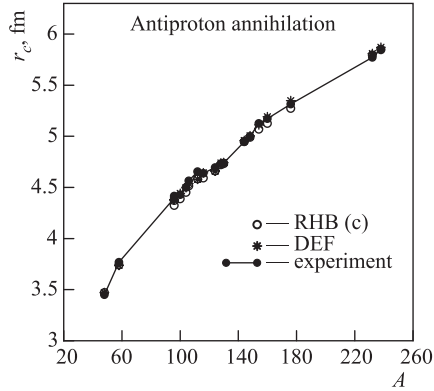


Fig. 21. The calculated (RMF/RHB) charge radii along with the corresponding experimental [71, 79, 80] values

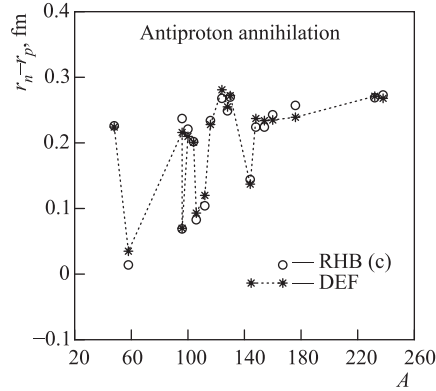


Fig. 22. The calculated neutron skin thickness ( $r_n - r_p$ ) for the nuclei used in the  $\bar{p}$  experiments

The calculated neutron skin thickness ( $r_n - r_p$ ) is shown in Fig. 22. It is seen that the trend in the neutron skin is qualitatively similar for RHB(c) and DEF, but there are some minor differences at a finer level. It is further noticed from the figure that the nuclei considered in this study, separate out into two distinct groups: those having larger  $r_n - r_p$  and those having small  $r_n - r_p$ . This observation is consistent with the fact that the nuclei belonging to the former have considerable neutron excess.

*Densities.* It is observed that the calculated point nucleon densities obtained by using different prescriptions for numerical solutions for the RMF/RHB equations are very similar. In fact, the calculated spherical densities (SPH, RHB(ob), RHB(c)) are almost identical in the interior and deviate slightly for large  $r$ , i.e., in the peripheral (outer) region. In the deformed case, the  $L = 0$  component in the expansion of the calculated densities (DEF) is also qualitatively similar to its spherical counterpart. Therefore, here, we shall restrict detailed discussion to the RHB(c) and DEF densities only.

For illustration, the calculated nucleon (neutron and proton) densities (DEF, RHB(c)) for some representative nuclei ( $^{96}\text{Zr}$  and  $^{238}\text{U}$ ) are shown in Fig. 23. It is clearly seen that the calculated proton (neutron) densities differ slightly only in the peripheral region, where the proton (neutron) densities have very small values. This, however, is very crucial as we shall see for the calculation of the peripheral factor.

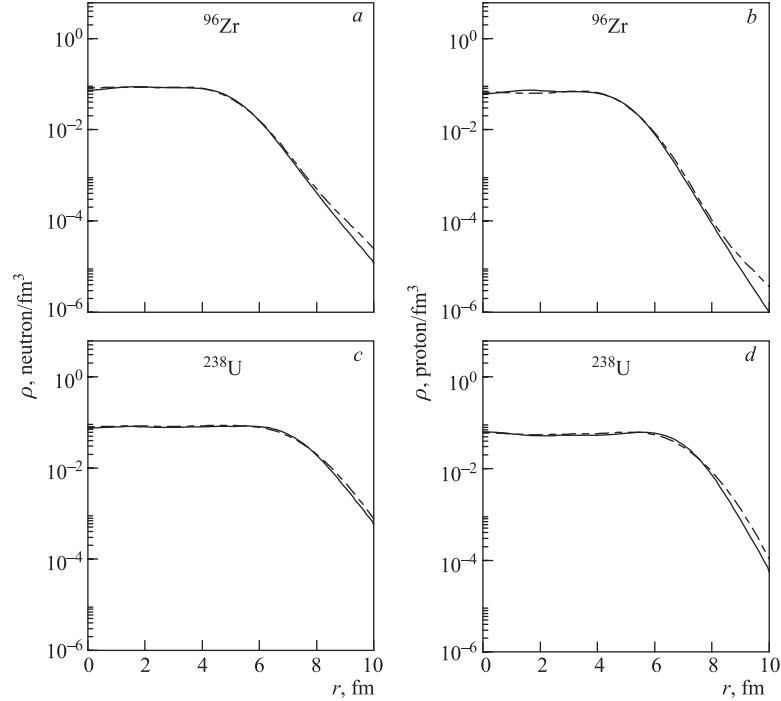


Fig. 23. Neutron (*a, c*) and proton (*b, d*) densities for some representative nuclei. Solid lines — RHB(c); dash-dotted lines — DEF

**4.2. Peripheral Factors.** The peripheral factors calculated by using densities obtained from RHB(c) and DEF along with the corresponding experimental values are presented in Fig. 24. In this figure, we have not included the SPH and RHB(ob) results. It is noticed that the  $f_{\text{exp}}^p$  is smaller than unity only for two cases viz.  $^{106}\text{Cd}$  ( $0.6 \pm 0.1$ ) and  $^{144}\text{Sm}$  ( $\leq 0.5$ ) (not shown in the figure). The single proton separation energies for these two cases are 7.3 and 6.3 MeV [66], respectively, as compared to the corresponding single neutron separation energies 10.7 and 10.5 MeV [66]. This does not seem to indicate a long proton tail. The corresponding calculated values of the peripheral factor for RHB(c) (DEF) are 1.5 and 2.2 (1.7 and 2.1), respectively. Therefore, these experimental results are somewhat surprising. Similar remarks also hold for  $^{96}\text{Ru}$  and  $^{112}\text{Sn}$  where the experimental values of  $f^p$  ( $f_{\text{exp}}^p$ ) are close to 1 ( $1.1 \pm 0.2$  for  $^{96}\text{Ru}$  and  $1.01 \pm 0.18$  for  $^{112}\text{Sn}$ ). The corresponding RHB(c) (DEF) values are 1.3 (1.3) and 1.9 (2.3), respectively.

The inspection of Fig. 25 reveals that the calculated  $f^p$  are qualitatively similar to the experiment. However, they are widely spread over for individual cases. In order to ascertain the quality of agreement, we calculate the mean squared deviation  $D$  and the  $\chi^2$ . These are defined as [75]:

$$D = \frac{1}{N} \sum_i (y_i - y_i^{\text{exp}})^2 \quad (54)$$

and

$$\chi^2 = \frac{1}{N} \sum_i \frac{(y_i - y_i^{\text{exp}})^2}{(\delta y_i)^2}. \quad (55)$$

Here,  $e_i$  is the error in  $y_i^{\text{exp}}$ .

The calculated values of  $D$  and  $\chi^2$  are presented in Table 6. In these calculations,  $^{106}\text{Cd}$  and  $^{144}\text{Sm}$  are not considered for the reasons mentioned earlier. The  $\chi^2$  varies from 11 to 24 for the calculated  $f^p$  values. This variation in  $\chi^2$  is not surprising since the calculated  $f^p$  is a ratio of two very small numbers ( $\rho_n$  and  $\rho_p$  at the annihilation site), therefore, a very small error even in any one of them may result in a large change in the calculated  $f^p$ . The  $\chi^2$  for RHB(c) is found to be minimum and this probably is due to the use of large box in RHB(c).

In order to ascertain the correlation between peripheral factor and the single neutron separation energy ( $S_n$ ), the correlation coefficient  $\mathcal{C}$  and the slope regression coefficient  $\mathcal{R}$  (with standard error; see [75]) are calculated. These are presented in Table 7.

It is clear from the table that both RHB(c) and RHB(ob) give relatively better negative correlations as compared to the rest (SPH and DEF). However,

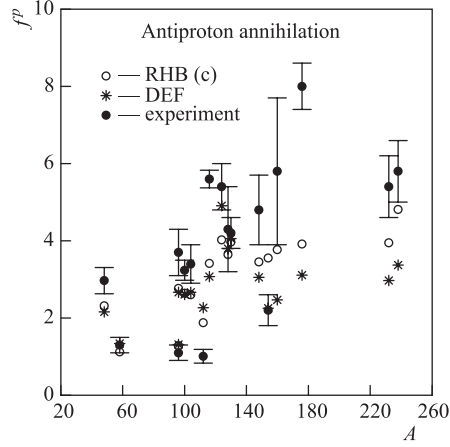


Fig. 24. The calculated peripheral factors along with the corresponding experimental values [28, 32] plotted as a function of mass number

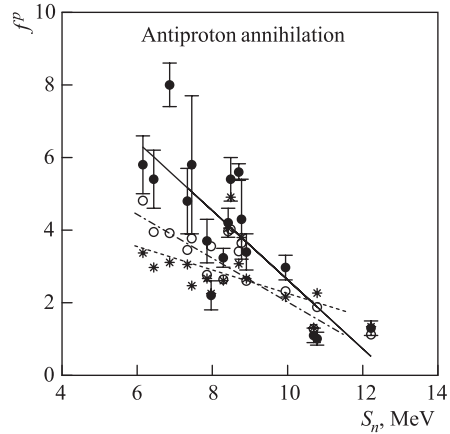


Fig. 25. The dependence of the RHB(c) (○), the DEF (\*) and the experimental (●) peripheral factors on  $S_n$  along with the best fit lines for RHB(c) (dash-dotted), DEF (dashed) and experiment (solid)

comparison of the slope regression coefficients reveals that RHB(c) gives a better description of the experiment, as compared to the other prescriptions of solving the RMF/RHB equations.

**Table 6. The calculated  $D$  and  $\chi^2$  values**

Approximation	$D$	$\chi^2$
RHB(c)	2.2	11.8
RHB(ob)	4.1	18.7
SPH	6.2	24.3
DEF	3.6	16.5

**Table 7. The calculated correlation coefficients ( $\mathcal{C}$ ) and regression coefficients  $\mathcal{R}$**

Approximation	$\mathcal{C}$	$\mathcal{R}$
RHB(c)	-0.88	$-0.56 \pm 0.08$
RHB(ob)	-0.86	$-0.35 \pm 0.05$
SPH	-0.52	$-0.16 \pm 0.07$
DEF	-0.53	$-0.30 \pm 0.12$
Experiment	-0.80	$-0.95 \pm 0.19$

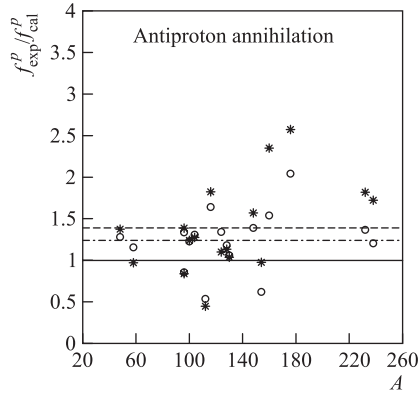


Fig. 26. The variation of the ratio of peripheral factors  $f_{\text{exp}}^p/f_{\text{cal}}^p$  for the RHB(c) (○) and the DEF (\*) with mass number. The lines corresponding to the average value of the ratio for the RHB(c) and that of DEF are also indicated by dash-dotted and dashed lines, respectively

**Table 8. The mean values and standard deviations for the ratio of the theoretical and the corresponding experimental peripheral factors**

Approximation	$\bar{x}$	$\sigma$
RHB(c)	1.24	0.35
RHB(ob)	1.39	0.57
SPH	1.82	0.80
DEF	1.39	0.53

deviation [75] is computed. The values of  $\sigma$ , so obtained are listed in Table 8 along with the corresponding values of  $\bar{x}$ . The inspection of the data presented in the table reveals that the results of the RHB(c) calculations are relatively closer to the experiment as compared to those of SPH, DEF, and RHB(ob).

Next, the ratio  $f_{\text{exp}}^p/f_{\text{cal}}^p$  is plotted against the atomic mass number in Fig. 26. For a perfect agreement between the calculation and the experiment, the ratio should be unity. Both the RHB(c) and DEF values are scattered around 1. The mean values  $\bar{x}$  for the ratio are presented in Table 8. The  $\bar{x}$  values corresponding to RHB(c) and DEF are also shown by dash-dotted and dashed lines (respectively) in Fig. 26. For quantification, the standard

## 5. ORIGIN OF PSEUDOSPIN SYMMETRY

The pseudospin symmetry has been discovered in nuclear physics nearly 30 years ago [22,23] and since then it has been used profitably and successfully for the description of several nuclear properties. The real origin of the pseudospin symmetry remained unknown till the recent observation of Ginocchio [24,81], where for the first time the origin of this symmetry has been claimed to be revealed as due to the near equality in magnitude of the attractive scalar and repulsive vector fields in relativistic theories.

**5.1. Pseudospin Concept.** The concept of pseudospin symmetry [22,23] is based on the experimental observation of the existence of quasi-degenerate doublets of normal parity orbitals ( $n, \ell, j = \ell + 1/2$ ) and ( $n-1, \ell+2, j = \ell+3/2$ ) such as ( $4s_{1/2}, 3d_{3/2}$ ), ( $3d_{5/2}, 2g_{7/2}$ ), etc., in the same major shell. Since for spherical systems the quantum numbers  $j^\pi$  are conserved, the pseudospin angular momenta ( $\tilde{\ell}, \tilde{s} = 1/2$ ) satisfy  $\tilde{j} = j = \tilde{\ell} \pm 1/2$ . Thus, the experimentally observed single-particle states are approximately pairwise degenerate.

To interpret this near degenerate pair of  $j = \ell + 1/2$  and  $j = \ell + 3/2$  states as pseudospin ( $\tilde{s}$ ) doublets corresponding to  $\tilde{m}_s = \pm 1/2$ , pseudospin angular momentum  $\tilde{\ell}$  has to be  $\ell + 1$ . It then follows that the pseudoquantum number:  $\tilde{N} = N - 1$ , the radial quantum number  $\tilde{n} = n - 1$  and the parity  $\tilde{\pi} = -\pi$ . For zero pseudospin orbit splitting, the pseudospin multiplet will be degenerate. Thus the pair of orbitals ( $4s_{1/2}, 3d_{3/2}$ ) and ( $3d_{5/2}, 2g_{7/2}$ ) can be viewed as the ( $2\tilde{p}_{1/2}, 2\tilde{p}_{3/2}$ ) and ( $1\tilde{f}_{5/2}, 1\tilde{f}_{7/2}$ ) pseudospin doublets, respectively. The symmetry can also be investigated in deformed nuclei. In the asymptotic Nilsson scheme one finds the pseudospin quantum numbers ( $\tilde{N} = N - 1, \tilde{n}_3 = n_3, \tilde{\Lambda} = \Lambda + 1$ , and  $\tilde{\Omega} = \Omega$ ). Therefore, the Nilsson orbitals [ $N, n_3, \Lambda, \Omega = \Lambda + 1/2$ ] and [ $N, n_3, \Lambda + 2, \Omega = \Lambda + 3/2$ ] can be viewed as the pseudospin orbit doublets [ $\tilde{N}, \tilde{n}_3, \tilde{\Lambda}, \tilde{\Omega} = \tilde{\Lambda} \pm 1/2$ ] [82]. For example, the pair [ $404$ ] $_{7/2^+}$  and [ $402$ ] $_{5/2^+}$  can be interpreted as the pseudospin orbit doublet: [ $\tilde{3}\tilde{0}\tilde{3}$ ] $_{7/2^-, 5/2^-}$ .

Models based on this concept have been shown to provide successful spectroscopic description of nuclei away from closed shell regions (e.g., see [83]).

**5.2. Relativistic Origin of Pseudospin Symmetry.** In the following discussion, we omit the explicit mention of the corresponding equations and contributions from the  $\rho$  meson and the photon since these are not relevant to the present discussion. However these are considered in the actual calculations and therefore, the results do include their contributions.

For spherically symmetric case the nucleon spinor  $\psi_i(\mathbf{r}, s, t)$  is chosen to be of the form

$$\psi_i(\mathbf{r}, s, t) = \begin{pmatrix} \psi_{u_i} \\ \psi_{l_i} \end{pmatrix} = \begin{pmatrix} f_i(r) \Phi_{\ell_i j_i m_i}(\vartheta, \varphi, s) \\ ig_i(r) \Phi_{\tilde{\ell}_i j_i m_i}(\vartheta, \varphi, s) \end{pmatrix} \chi_{t_i}(t) \quad (56)$$

with

$$\Phi_{\ell jm}(\vartheta, \varphi, s) = \sum_{m_s m_\ell} \left\langle \ell m_\ell \frac{1}{2} m_s \middle| jm \right\rangle Y_{\ell m_\ell}(\vartheta, \varphi) \chi_{m_s}(s), \quad (57)$$

where  $Y_{\ell m_\ell}(\vartheta, \varphi)$  is the spherical harmonics and  $\chi_{t_i}$  ( $\chi_{m_s}(s)$ ) is the isospin (spin) part of the wave function of the nucleon  $i$ . The orbital angular momenta  $\ell_i$  and  $\tilde{\ell}_i$  are determined by  $j_i$  and the parity  $\pi_i$  as

$$\ell = j + 1/2, \quad \tilde{\ell} = j - 1/2 \quad \text{for} \quad \pi = (-)^{j+1/2} \quad (58)$$

and

$$\ell = j - 1/2, \quad \tilde{\ell} = j + 1/2 \quad \text{for} \quad \pi = (-)^{j-1/2}. \quad (59)$$

The equivalent Schrödinger equation can be obtained starting from the Dirac equation, by eliminating the small component. Here, however, we prefer to eliminate the large component for this purpose.

Eliminating the large component  $\psi_{u_i}$  we have for the small component  $\psi_{l_i}$  the following second-order differential equation (see [25, 27]):

$$\left\{ -\nabla^2 - \frac{S' - V'}{E - (S - V)} \left( \frac{\partial}{\partial r} - \frac{\kappa_i - 1}{r} \right) \right\} \psi_{l_i} = (2m - E - (S + V))(E - (S - V))\psi_{l_i}. \quad (60)$$

For the case of equal strengths,  $S = V$ , Eq. (60) reduces to:

$$-\nabla^2 \psi_{l_i} + E(S + V) \psi_{l_i} = E(2m - E) \psi_{l_i}. \quad (61)$$

Clearly, Eq. (61) has an energy-dependent potential ( $E(V + S)$ ) and has the eigenvalue  $E(2m - E)$ . After scaling the radial variable  $r = x/(\sqrt{E})$ , the potential has a complicated ( $\sqrt{E}$ ) dependence, i.e.,  $S(x/\sqrt{E}) + V(x/\sqrt{E})$ . In such a situation this equation (61) is no longer a normal Schrödinger eigenvalue equation. Further, it is obvious that for this equation all solutions with «bound» states in the Fermi sea with  $E \geq 0$  are shifted to one degenerate eigenvalue with  $E = 0$ , which, in fact, is not bound. The corresponding wave functions are not normalizable. This indeed is an unphysical situation. This equation is the same as Eq. (3) of [24] in the scaled variable  $x$  when written in terms of the partial waves and using the relation  $\ell(\ell + 1) = \kappa(\kappa - 1)$ .

$$\left\{ \frac{d^2}{dx^2} + \frac{2}{x} \frac{d}{dx} - \frac{\tilde{\ell}(\tilde{\ell} + 1)}{x^2} - [(V - S) - 2 + E] \right\} g_i = 0. \quad (62)$$

Here  $\ell$ , the angular momentum of the lower component  $g_i$ , is identified with the pseudospin angular momentum ( $\tilde{\ell}$ ). This is the pseudospin symmetry limit

of Ref. 24, where the doublets  $j = \tilde{\ell} \pm 1/2$  with the same  $\tilde{\ell}$  are degenerate. However, in this limit only the Dirac sea states exist and no Dirac valence bound states and therefore it contradicts reality. According to these considerations in all realistic situations the pseudospin symmetry must be broken. Therefore the question arises, to what extent it is broken in real nuclei.

**5.3. Realistic Calculations, Results and Discussions.** The broken pseudospin symmetry both for the spherical and deformed nuclei within the relativistic mean field approach has been investigated [25, 27, 84]. For its study,  $^{208}\text{Pb}$  is chosen as a representative of spherical nuclei; and  $^{154}\text{Dy}$  as a representative of deformed nuclei. The Lagrangian parameter set NL3 [63] is used in the calculations.

First, spherical RMF calculations in the coordinate space are carried out for  $^{208}\text{Pb}$ . The calculated binding energy and the charge radius agree remarkably well with the experiment. The calculated single particle energies for the bound orbitals near the Fermi surface are shown in Fig. 27, *a* for neutrons ( $\nu$ ) and protons ( $\pi$ ). It is clear from the figure that the pairs of bound neutron valence orbitals ( $2g_{7/2}$ ,  $3d_{5/2}$ ) and ( $1i_{11/2}$ ,  $2g_{9/2}$ ) which correspond to pseudospin doublets ( $2\tilde{f}_{7/2}$ ,  $2\tilde{f}_{5/2}$ ) and ( $1\tilde{h}_{11/2}$ ,  $1\tilde{h}_{9/2}$ ), respectively, are quasi-degenerate indicating only a small breaking of pseudospin symmetry. The same is more or less true for the pairs of neutron hole ( $(2f_{5/2}$ ,  $3p_{3/2})$ ,  $(1h_{9/2}$ ,  $2f_{7/2})$ ), proton valence (particle) ( $1h_{9/2}$ ,  $2f_{7/2}$ ), and proton hole ( $(2d_{3/2}$ ,  $3s_{1/2})$ ,  $(1g_{7/2}$ ,  $2d_{5/2})$ ), orbitals forming the pseudospin doublets. But here the energy separation between the partners of the respective doublets is relatively larger. The larger is the binding energy the larger is the separation. This indicates that the concept of the pseudospin symmetry becomes better and better for the orbitals as their energies approach closer and closer to the continuum. This is consistent with the results found in [24] for the square-well potentials. In addition, the energy separation becomes larger if the pseudo-orbital angular momentum ( $\tilde{\ell}$ ) increases. The dependence of the energy splitting of the pseudospin partners on the energy  $E$  and on the pseudo-orbital angular momentum  $\tilde{\ell}$  can easily be understood from Eq. (60). For a given pseudo-orbital angular momentum  $\tilde{\ell}$  the term in Eq. (60) which splits the pseudospin partners is:

$$\frac{S' - V'}{(S - V) - E} \frac{\kappa_i}{r}. \quad (63)$$

It has the energy dependence  $(E - (S - V))$  in the denominator. Now  $(S - V)$  is about 50 MeV. Bound states in the Fermi sea have a binding energy  $E < 50$  MeV. For increasing binding energy  $E$ , i.e., going to more deeply bound states, the denominator decreases. This then results in a larger energy splitting between the pseudospin partners. For example, for the orbit  $\tilde{\ell} = 3$  the energy splitting between the pseudospin partners ( $1g_{7/2}$  and  $2d_{5/2}$ ) will be relatively larger as compared to that between ( $2g_{7/2}$  and  $3d_{5/2}$ ). In addition, the bigger is the value of  $\tilde{\ell}$  the larger is the splitting. For instance, the energy splitting between the pseudospin partners

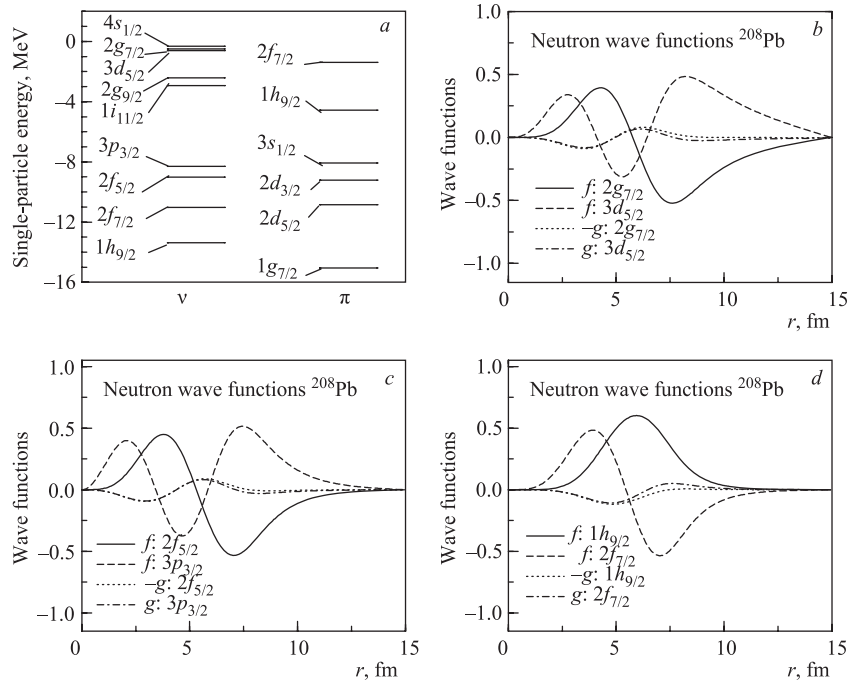


Fig. 27. Pseudospin splitting in the spherical nucleus  $^{208}\text{Pb}$ : *a*) single-particle spectra in the vicinity of the Fermi surface for neutrons ( $\nu$ ), protons ( $\pi$ ), large ( $f$ ) and small ( $g$ ) components of the Dirac wave functions for the pseudospin doublets  $\nu 2\bar{d}$  (*b*),  $\nu 2\bar{f}$  (*c*), and  $\pi 2\bar{q}$  (*d*) [85]

( $1i_{11/2}$  and  $2g_{9/2}$ ) corresponding to  $\tilde{\ell} = 5$  is relatively larger as compared to that between the partners ( $2g_{7/2}$  and  $3d_{5/2}$ ) which corresponds to  $\tilde{\ell} = 3$ , in the same major shell. Interestingly, the sign of the energy splittings between the partners of the neutron valence doublets is opposite to those of the neutron hole, proton doublet, and proton hole doublets.

The normalized single nucleon wave functions (both large ( $f$ ) and small ( $g$ ) components) are plotted for the pseudospin partners corresponding to the valence neutron pairs, the neutron hole pairs and valence proton pairs in Figs. 27, *b*, *c*, and *d*, respectively. The phase of the lower components ( $g$ ) of one of the partners is reversed while plotting in order to exemplify the differences in the lower components of the pseudospin partners. Clearly, the lower components are much smaller in magnitude as expected and are almost equal in magnitude. In the case of exact pseudospin symmetry, the lower component of the pseudospin partners should be identical (except for the phase). The very small differences

between these  $g$ 's which mainly appear around the surface are negligible for the pseudospin partners having very small binding energies.

Next we consider deformed systems and impose constraint on the quadrupole moment. Relativistic Hartree calculations have been carried out for the nucleus  $^{154}\text{Dy}$ . Numerical details are given in [6]. Pairing correlations are treated in the constant gap approximation and the Lagrangian parameter set NL3 [63] is used.

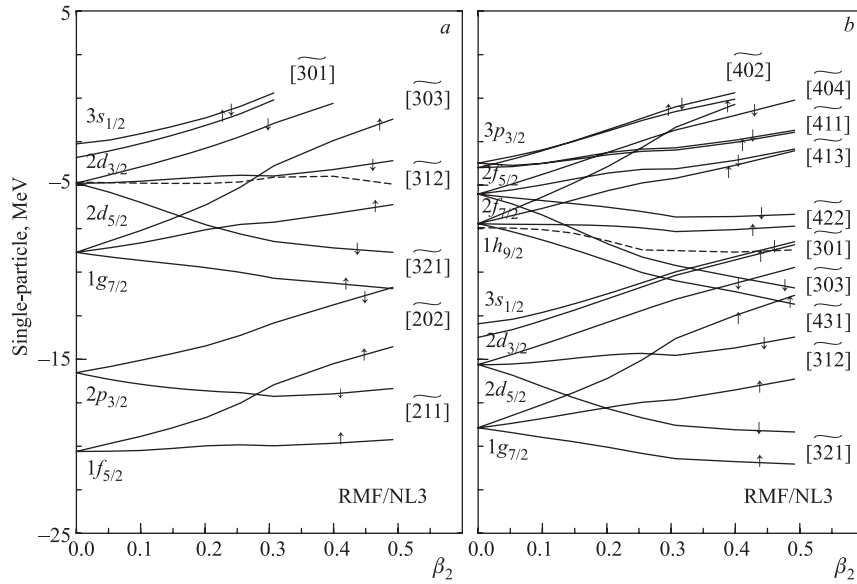


Fig. 28. Single-particle energies of the deformed Dirac equation for the protons (a) and neutrons (b) in the nucleus  $^{154}\text{Dy}$  as a function of the quadrupole deformation parameter  $\beta_2$  [85]. Asymptotic pseudospin quantum numbers are given and the pseudospin partners are indicated by arrows  $\uparrow$  and  $\downarrow$ .

The energies of the bound proton (neutron) pairs of orbitals corresponding to pseudospin doublets are plotted against the deformation  $\beta_2$  ranging from 0.0 to 0.5 in Fig. 28. The asymptotic Nilsson quantum numbers  $[N, n_3, \tilde{\Lambda}, \tilde{\Omega}]$  are good for large values of the deformation  $\beta_2$ . The pseudospin doublets  $[\tilde{N}, \tilde{n}_3, \tilde{\Lambda}, \tilde{\Omega} = \tilde{\Lambda} \pm 1/2]$  [82] are indicated by  $[\tilde{N}, \tilde{n}_3, \tilde{\Lambda}] \uparrow$  and  $\downarrow$  in the figure. For zero deformation ( $\beta_2 = 0$ ), the orbitals are indicated by the corresponding spherical states. The figure reveals the following number of interesting facts. It is seen that the energy splitting between the pseudospin partners is smaller for the valence orbitals and for the partners just below the Fermi surface. This energy difference is relatively larger for the partners having larger pseudospin angular momentum ( $\tilde{\ell}$ ). In general, this separation stays almost constant and does not vary with deformation after reasonable value of  $\beta_2$ . The energy difference between the

$\downarrow$  and the  $\uparrow$  partners always remains positive except for [404], where there is crossing at around  $\beta = 0.3$ . Such a crossing is not very unusual, it has also been observed in [82].

These systematics are consistent with those observed in the spherical case above. For more results and details, see [25,27].

Thus, it is established that the origin of pseudospin symmetry, indeed, is relativistic, and it is well accounted for within the RMF framework.

## 6. CROSS SECTIONS

To test the calculated ground state densities further, we now investigate the reaction properties of some of the nuclei considered here. Experimentally, the reaction cross sections have been measured for chains of the Nitrogen, Neon, and Argon isotopes [33,74]. The charge-changing cross sections have also been measured for some of these nuclei [35,37] and for a few Iron isotopes [86].

The reaction analysis of the loosely bound nuclei at high projectile energies is most conveniently carried out using the Glauber model, which is based on the multiple scattering theory [34]. The Glauber model requires the densities of target and projectile nuclei as inputs. Therefore, comparison of the calculated reaction cross sections with the corresponding experiment will be a good test of the calculated densities. It can be, in simple terms, viewed as the well-known eikonal approximation applied to the case of multiple scattering. The eikonal approximation is applicable for those scattering problems, where the scattering potential varies a little over a distance of the order of the de Broglie wavelength. As long as the projectile energy is sufficiently high, the potential itself need not be weak. This situation is quite different from the Börn approximation, where the effect of the potential on the incoming wave is not large [87]. Under the conditions of the eikonal approximation, the semiclassical notion of path becomes tenable. Hence, it becomes possible to replace the exact wave function by the semiclassical wave function, in terms of Hamilton's principal function. Thus, here, it is implicitly assumed that the projectile has «sufficiently» high energy so that the eikonal approximation is valid. However, it has been shown [88–90] that with some modifications, the Glauber model can be used with remarkable success for the case of intermediate energies as well. This is known as the Finite Range Glauber Model.

Under the optical limit [88,91] of the Glauber model, the reaction cross section ( $\sigma_R$ ), defined as the total cross section for change in the mass number of the projectile, is expressed as:

$$\sigma_R = 2\pi \int b db [1 - T(b)], \quad (64)$$

where  $T(b)$  is the transparency function at impact parameter  $b$ .

### 6.1. Glauber Model at High Projectile Energies: Zero Range Limit.

Replacing the nucleon profile function [34] by  $\delta$  function times the experimental nucleon–nucleon ( $NN$ ) cross section  $\bar{\sigma}$  (zero range limit), the transparency function  $T(b)$  reduces to:

$$T(b) = \exp \left[ - \sum_{i,j} \bar{\sigma}_{ij} \int ds \bar{\rho}_{ti}(s) \bar{\rho}_{pj}(|\mathbf{b} - \mathbf{s}|) \right]. \quad (65)$$

Here, the summation indices  $i$  and  $j$  run over neutrons and protons of the target and the projectile. The subscript  $t(p)$  refers to target (projectile), and  $\bar{\rho}(s)$  is the  $z$ -direction integrated nucleon (proton and neutron) density distribution expressed as:

$$\bar{\rho}(s) = \int_{-\infty}^{+\infty} dz \rho \left( \sqrt{s^2 + z^2} \right), \quad (66)$$

with  $s^2 = (x^2 + y^2)$ .

The calculation of the reaction cross section in the Glauber model requires the experimental  $NN$  cross section and the density distributions of both the target and the projectile. The former is taken from experiments, and is then multiplied by a phenomenological factor  $\epsilon$  (usually taken to be 0.8), to partly include the effects due to the nuclear medium. For example, due to Pauli blocking and Fermi motion, the in-medium  $NN$  cross section gets attenuated in comparison with the free nucleon–nucleon cross section.

**6.2. Glauber Model at Low Projectile Energies.** The Glauber model discussed up to now (zero range Glauber model), is applicable for higher projectile energies. The zero range Glauber model is required to be modified when the projectile energies are small. The modifications are twofold: 1) the finite range effects in the profile function and 2) the Coulomb modified trajectories.

Within the finite range approximation the transparency function is written as:

$$T(b) = \exp \left\{ - \int_P \int_T \sum_{ij} [\Gamma_{ij}(\mathbf{b} - \mathbf{s} + \mathbf{t}) \bar{\rho}_{Pi}(\mathbf{t}) \bar{\rho}_{Tj}(\mathbf{s})] ds dt \right\}. \quad (67)$$

Here, the profile function is given by [88, 90]:

$$\Gamma_{ij}(b_{\text{eff}}) = \frac{1}{2\pi\beta^2} \sigma_{ij} \exp \left( - \frac{b_{\text{eff}}^2}{2\beta^2} \right). \quad (68)$$

In this expression,

$$b_{\text{eff}} = |\mathbf{b} - \mathbf{s} + \mathbf{t}|, \quad (69)$$

$b$  is the impact parameter and  $s$  and  $t$  are just the dummy variables for integration over the  $z$ -projected target and projectile densities. The range parameter  $\beta$  is

$$\beta = \beta_{NN} = 0.996 \exp\left(-\frac{E}{106.679}\right) + 0.089, \quad (70)$$

where  $E$  is the projectile energy. This range parameter is obtained by fitting  $^{12}\text{C}$  on  $^{12}\text{C}$  cross sections from  $30 A \cdot \text{MeV}$  to  $1 A \cdot \text{GeV}$  energies. The nucleon–nucleon cross section is as usual taken from the experiment, or taken from some empirical fit to the experimental nucleon–nucleon cross sections (see, for example, [89]).

Especially for the lower energies, apart from the finite range effect, another important aspect is required to be taken into account: the Coulomb effects. The straight line trajectories assumed in the Glauber model, get distorted since the Coulomb force becomes significant at lower energies. This effect can be incorporated in the Glauber model through the classical perihelion. Under this assumption, the Coulomb modified impact parameter ( $b'$ ) can be written as:

$$b' = \frac{1}{k} \left[ \eta + (\eta^2 + k^2 b^2)^{1/2} \right], \quad (71)$$

where,  $\eta$  is the usual Sommerfeld parameter, and  $k$  is the wave number of projectile. With this correction, the total reaction cross section is expressed as:

$$\sigma_R = 2\pi \int_{2\eta/k}^{\infty} b' \left(1 - \frac{\eta}{kb'}\right) [1 - T(b')] db'. \quad (72)$$

**6.3. Charge-Changing Cross Sections.** The charge-changing cross section is another important observable. It can be defined as the total cross section for all the processes which result in the change of the atomic number of the projectile. Neutron removal cross section can be similarly defined as the cross section for processes which result in a change of atomic mass but not of the atomic number of projectile [37]. The charge-changing cross sections are very important since they give information about the proton distributions in the nucleus in the presence of neutrons. Extensive experimental data on charge-changing cross sections is available in the literature [35, 37, 86, 92–97].

It had been proposed by Serber [98] that the nuclear breakup reactions can be modeled as two-step processes: the first step being fast, and the subsequent process being a slow process. The first step results in modification of the composition of the reaction partners, and it excites the fragments. This process is very fast and is called the abrasion stage. The second process, which is considerably slower than the first one, involves the de-excitation of the excited fragments by evaporation of neutrons, protons, light particles, etc. This is called the ablation

stage [99]. The ablation stage is expected to make additional contributions to the total charge-changing cross sections. Therefore, the charge-changing cross sections cannot be obtained directly in analogy with the total reaction cross section, by using the proton density of the projectile instead of the full (both the proton and the neutron) density of the projectile. There are some claims [100] that in spite of the possibility of additional contributions to the charge-changing cross section due to projectile neutrons, it is enough to use projectile proton densities to account for the experimental charge-changing cross sections. However, as we shall see later, this approach is, conceptually deficient.

Keeping these aspects in mind, we examine the structure of the transparency function:

$$T(b) = \exp \left[ - \sum_{i,j} \bar{\sigma}_{ij} \int ds \bar{\rho}_{ti}(s) \bar{\rho}_{pj}(|\mathbf{b} - \mathbf{s}|) \right]. \quad (73)$$

For brevity, the  $z$ -integrated densities  $\bar{\rho}_t(s)$  and  $\bar{\rho}_p(|\mathbf{b} - \mathbf{s}|)$  are replaced by  $\bar{\rho}_t$  and  $\bar{\rho}_p$ , respectively, for the target and projectile. Equation (73) then reads:

$$T(b) = \exp \left[ - \sum_{i,j} \bar{\sigma}_{ij} \int ds \bar{\rho}_{ti} \bar{\rho}_{pj} \right]. \quad (74)$$

Explicitly, summing over the neutron and proton indices:

$$\begin{aligned} \sum_{i,j} \bar{\sigma}_{ij} \int ds \bar{\rho}_{ti} \bar{\rho}_{pj} &= \bar{\sigma}_{pp} \int ds \bar{\rho}_{tp} \bar{\rho}_{pp} + \bar{\sigma}_{pn} \int ds \bar{\rho}_{tp} \bar{\rho}_{pn} + \\ &+ \bar{\sigma}_{np} \int ds \bar{\rho}_{tn} \bar{\rho}_{pp} + \bar{\sigma}_{nn} \int ds \bar{\rho}_{tn} \bar{\rho}_{pn}, \end{aligned} \quad (75)$$

$$\begin{aligned} &= (\bar{\sigma}_{pp} \int ds \bar{\rho}_{tp} \bar{\rho}_{pp} + \bar{\sigma}_{np} \int ds \bar{\rho}_{tn} \bar{\rho}_{pp}) + \\ &+ (\bar{\sigma}_{pn} \int ds \bar{\rho}_{tp} \bar{\rho}_{pn} + \bar{\sigma}_{nn} \int ds \bar{\rho}_{tn} \bar{\rho}_{pn}). \end{aligned} \quad (76)$$

The transparency function, therefore, splits up into the product of two terms:

$$T(b) = T^p(b) T^n(b), \quad (77)$$

where,

$$T^p(b) = \exp \left[ - (\bar{\sigma}_{pp} \int ds \bar{\rho}_{tp} \bar{\rho}_{pp} + \bar{\sigma}_{np} \int ds \bar{\rho}_{tn} \bar{\rho}_{pp}) \right], \quad (78)$$

$$T^n(b) = \exp \left[ - (\bar{\sigma}_{pn} \int ds \bar{\rho}_{tp} \bar{\rho}_{pn} + \bar{\sigma}_{nn} \int ds \bar{\rho}_{tn} \bar{\rho}_{pn}) \right]. \quad (79)$$

The subscripts  $n$  and  $p$  stand for neutrons and protons, respectively. Note that the transparency function has been factorized into two terms: one containing complete target density and only the proton density of the projectile and the other containing the complete target density and only the neutron density of the projectile (hence the superscripts  $n$  and  $p$ ). The reaction cross section, therefore, becomes:

$$\sigma_R = 2\pi \int bdb \left[ 1 - T^p(b)T^n(b) \right], \quad (80)$$

which, in turn, can be written as:

$$\begin{aligned} \sigma_R &= 2\pi \int bdb \left[ T^p(b) - T^p(b) + 1 - T^p(b)T^n(b) \right] = \\ &= 2\pi \int bdb \left[ 1 - T^p(b) \right] + 2\pi \int bdb \left[ T^p(b)(1 - T^n(b)) \right]. \end{aligned} \quad (81)$$

Intuitively [100], one may think that the charge-changing cross section may involve only the proton density of the projectile. The first term in Eq. (81) represents such a mechanism («Glauber Mechanism») for the charge-changing cross sections. We denote this term by  $\sigma_{cc}^{\text{free}}$ , signifying that the neutrons in the projectile have no role to play in the charge-changing process. The second term in Eq. (81) is denoted by  $\sigma_{cc}^I$ , leading to:

$$\sigma_R = \sigma_{cc}^{\text{free}} + \sigma_{cc}^I. \quad (82)$$

Notice that the quantities  $\sigma_R (= \sigma_{cc} + \sigma_{-xn})$  and  $\sigma_{cc}$  are experimentally measured. Theoretically, the calculations of  $\sigma_R$  and  $\sigma_{cc}^{\text{free}}$  are straightforward (unambiguous), while the problem appears in the calculation of  $\sigma_{cc}$ , because of the finite projectile neutron contribution ( $\sigma_{cc} - \sigma_{cc}^{\text{free}}$ ). The term  $\sigma_{cc}^I$  contains both 1) the projectile neutron contributions to the total charge-changing cross section and 2) the total neutron removal cross section. Realizing the fact that the projectile neutrons may also contribute to the charge-changing cross sections, we write  $\sigma_{cc}$  as a sum of two terms:

$$\sigma_{cc} = \sigma_{cc}^{\text{free}} + \mathcal{F}\sigma_{cc}^I. \quad (83)$$

The reaction cross section therefore becomes:

$$\sigma_R = \sigma_{cc} + (1 - \mathcal{F})\sigma_{cc}^I. \quad (84)$$

The total neutron removal cross section ( $\sigma_{-xn}$ ) for the projectile, is the difference between the reaction cross section and the corresponding charge-changing cross section. Therefore,

$$\begin{aligned} \sigma_{-xn} &= \sigma_R - \sigma_{cc}, \\ &= (1 - \mathcal{F})\sigma_{cc}^I. \end{aligned} \quad (85)$$

The detailed comparative study of the calculation and the experiment reveals that factor  $\mathcal{F}$  may be parametrized as [36]:

$$\begin{aligned}\mathcal{F} &= 0.8 \frac{Z^2}{N^2} \text{ for } N \geq Z, \\ &= 0.8 \quad \text{for } N < Z,\end{aligned}\tag{86}$$

where  $N(Z)$  denotes the neutron (proton) number of the projectile. This choice of  $\mathcal{F}$  works well throughout the periodic table [36].

**6.4. Results. Total Reaction Cross Sections.** The total reaction cross section is a fundamental and reliable quantity that is measured in the RIB experiments. Usually, the Glauber model is employed to analyze the cross sections and to deduce the r.m.s. radii. The Glauber model can also be used to estimate the total reaction cross sections theoretically. It requires both the target and the projectile

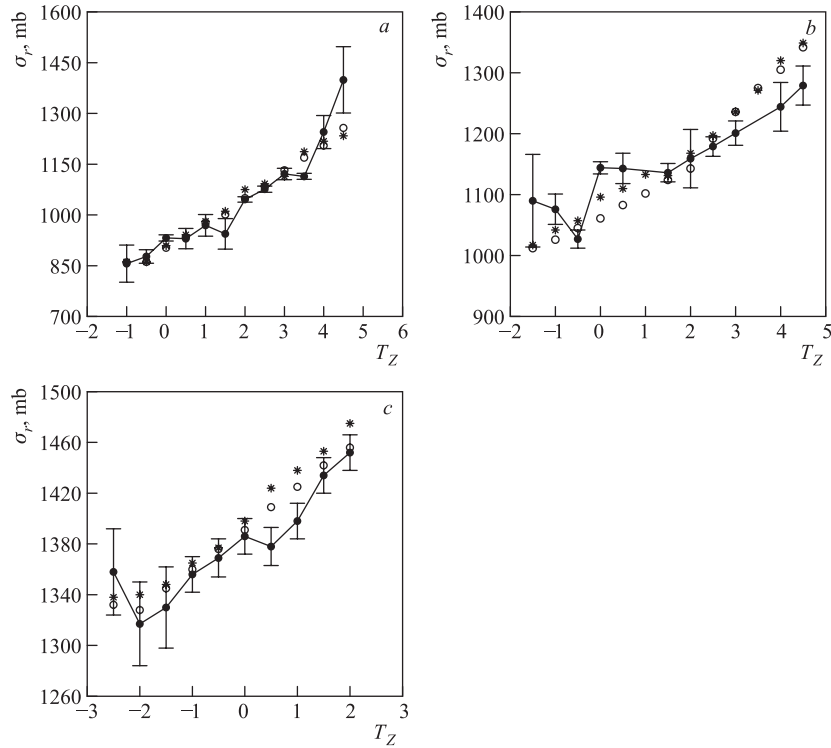


Fig. 29. The calculated (RHB(c) (○) and DEF (\*)) and the corresponding experimental (●, solid curves) [33, 74] reaction cross sections for the N (a), Ne (b) and Ar (c) chains as projectiles incident on  $^{12}\text{C}$  target

density distributions as the input. These can be obtained from a theoretical model. In this work, we use the calculated RMF/RHB neutron and proton densities of the nuclei considered here, in the Glauber model as projectile densities. The target density ( $^{12}\text{C}$ ) has been taken from an earlier work [101].

The deformed densities cannot be used as such in calculating the cross sections. Therefore, in this work, the deformed densities are expanded in terms of multipoles, and the  $L = 0$  component is projected out. It is the renormalized (to the correct particle number)  $L = 0$  component that is used in the cross-section calculations. The results obtained for this case are denoted by DEF.

The calculated reaction cross sections for the nuclei belonging to the chains of N, Ne, and Ar isotopes as projectiles on  $^{12}\text{C}$  target at specified projectile energies are plotted in Fig. 29. The corresponding experimental values [33,74] are also indicated. The overall agreement between the theory and the corresponding experimental results is impressive. Finer differences do exist at various places. The maximum difference between the theory and the experiment is  $\sim 6\%$ .

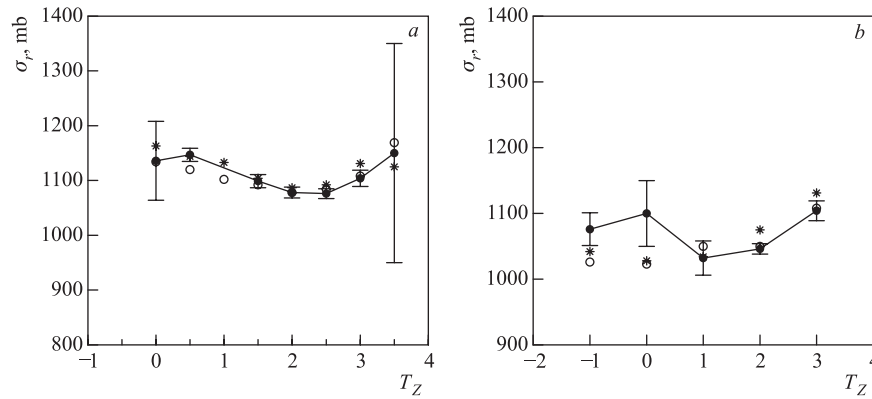


Fig. 30. The calculated (RHB(c) (○) and DEF (\*)) and the corresponding experimental (●, solid curves) [33] reaction cross sections for the nuclei in the  $N = 12$  (a) and  $A = 18$  (b) chains as projectiles incident on  $^{12}\text{C}$  target

Next, we plot the reaction cross sections for the  $N = 12$  and  $A = 18$  chains in Fig. 30. Again, the agreement between the theory and the experiment is found to be excellent. It should be noted that the deformation has a little effect on the cross sections. Still, there are a few cases like  $^{20}\text{Ne}$ , where inclusion of deformation does bring the calculated cross sections closer to the experiment.

*Charge-Changing Cross Sections.* We present and discuss the results obtained for  $\sigma_{cc}$  using the proposed model [36] for the nuclei belonging to N and Fe (isotopic),  $N = 12$  (isotonic), and  $A = 18$  (isobaric) chains incident on  $^{12}\text{C}$  target. The results for Fe chain are for polyethylene ( $-\text{CH}_2$ ) target.

The respective results for  $\sigma_{cc}$  are presented in Fig. 31. The figures reveal excellent agreement between the present model and the corresponding experiment. The curve with the tag «free» corresponds to  $\sigma_{cc}^{\text{free}}$  (Eq. (82)). The curve without any such tag corresponds to the present model (Eq. (83)). The Glauber model, as mentioned earlier, requires an additional phenomenological parameter, denoted by  $\epsilon$ , which is the ratio of the experimental free nucleon–nucleon cross section to the in-medium nucleon–nucleon cross section. The in-medium nucleon–nucleon cross section may be less than the free value. This is reasonable, since the medium poses restrictions due to complicated effects like the Pauli blocking and Fermi motion. In almost all the Glauber model analysis, this parameter is assumed to have a fixed value, 0.8 [69]. In order to reproduce the experimental  $\sigma_{cc}$  with only the first term ( $\sigma_{cc}^{\text{free}}$ ), this parameter should be enhanced to at least 1.3, which

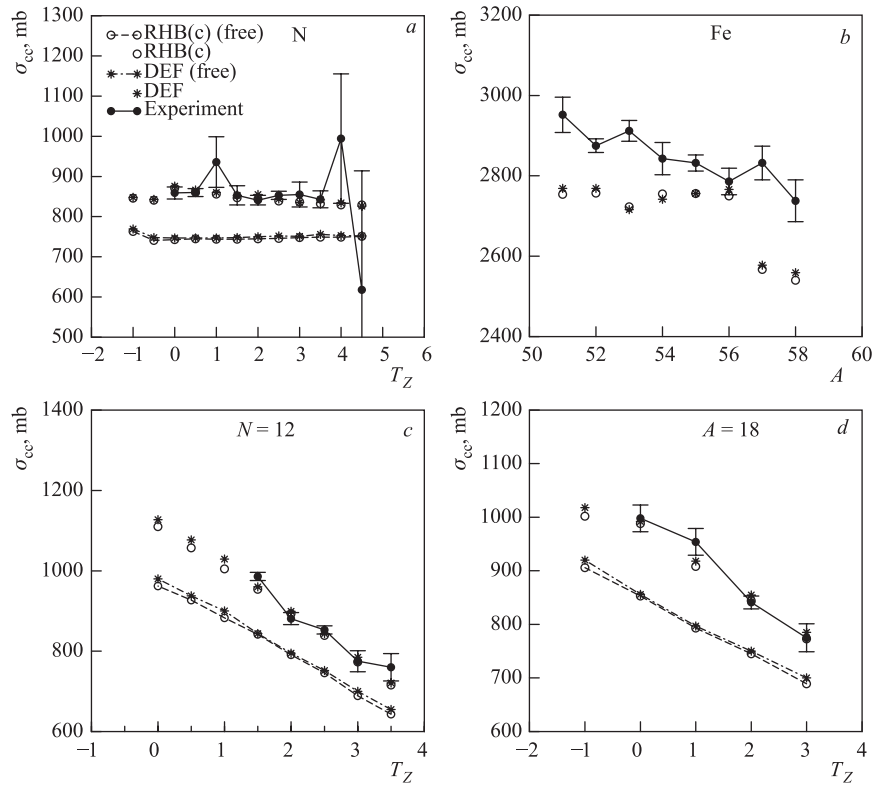


Fig. 31. The calculated charge-changing cross sections ( $\sigma_{cc}$ ) along with the corresponding experimental values [35, 37, 86] (where available)

may be unphysical. It is to be noted that with this  $\epsilon = 1.3$ , the calculated  $\sigma_R$  are overestimated. It is recommended that for the consistent description of  $\sigma_R$  and  $\sigma_{cc}$  the same factor  $\epsilon$  (0.8) should be used.

The experimental  $\sigma_{cc}$  are almost constant for a given chain of isotopes. However, there are sudden jumps in the cross sections. For example,  $^{16}\text{N}$  is found to have large charge-changing cross sections in comparison with the neighboring nuclei. Also, there is a sharp decline in  $\sigma_{cc}$  from  $^{22}\text{N}$  to  $^{23}\text{N}$ . This may correspond to the appearance of a new magic shell ( $N = 16$ ).

*Neutron Removal Cross Sections.* Knowing the reaction cross sections and the charge-changing cross sections, the neutron removal cross sections ( $\sigma_{-xn}$ ) can be

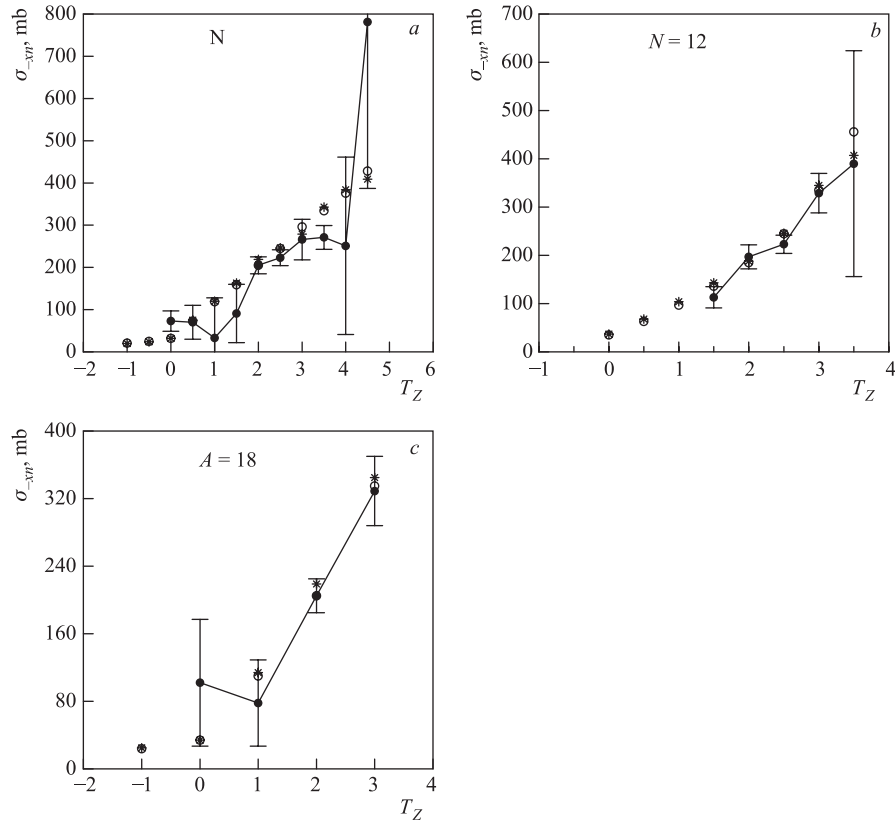


Fig. 32. The calculated neutron removal cross sections ( $\sigma_{-xn}$ ) along with the corresponding experimental values (●, solid curves) (deduced from [35,37]) (where available). ○ — RHB(c); \* — DEF

obtained, merely by taking the difference between the two [33]. Here, we present and discuss our results of  $\sigma_{-xn}$  and compare these with the corresponding  $\sigma_{-xn}$  values deduced from the experimental reaction cross sections and the charge-changing cross sections. It should be noted that the neutron removal cross sections thus *deduced* from the experimental data may be a little bit erroneous, since taking this difference implies that both the cross sections have been measured at the same energy. The projectile energies are different in some of these cases. Since these energies are relativistic, the energy dependence is expected to be weak.

The agreement between the theory (RHB(c) and DEF) and the corresponding so-called experimental  $\sigma_{-xn}$  is impressive. This validates the reliability of the proposed model for  $\sigma_{cc}$  and hence that for  $\sigma_{-xn}$ . The neutron removal cross sections for the neutron deficient nuclei are found to be small (few tens of mb), which is intuitively clear. Beyond  $N = Z$ ,  $\sigma_{-xn}$  is found to increase almost linearly with the third component of isospin, which is in agreement with the corresponding experiment. Thus, within the framework of the Glauber model, it is possible to describe observables like the charge-changing and neutron removal cross sections, consistently with the reaction cross sections.

*Further Considerations.* The charge-changing cross section is related to the proton density of the projectile. Actually, the dominant contribution ( $\geq 80\%$ ) to the charge-changing cross section comes from the Glauber-type mechanism ( $\sigma_{cc}^{free}$ ), where the neutrons in the projectile are considered to be merely spectators. The other mechanisms contribute the rest ( $\leq 20\%$ ) and these have been considered phenomenologically in the second term of our definition (in Eq. (83)).

Further, we find that the neutron removal cross sections increase linearly with the increase in the neutron number. Therefore, it is natural to investigate, how these quantities are related to the neutron skin thickness and hence the difference between the corresponding single-nucleon separation energies. We have seen earlier that the latter two are related to each other through a very strong negative linear regression.

To explore this, we next study the ratio:

$$\mathcal{R}_{cc}^{-xn} = \frac{\sigma_{cc} - \sigma_{-xn}}{\sigma_R} \quad (87)$$

as a function of the calculated values of nuclear skin thickness.

This ratio is plotted as a function of the corresponding values of nuclear skin thickness in Fig. 33. Inspection of these figures reveals a remarkable feature: the ratio  $\mathcal{R}_{cc}^{-xn}$  is nearly independent of skin thickness for neutron deficient nuclei (negative skin thickness), whereas for the neutron-rich side, it bears a very strong negative linear correlation (with correlation coefficient close to  $-1$ ) with the corresponding values of nuclear skin thickness. To quantify this observation, the regression analysis is carried out. The calculated results are arranged in Table 9. Inspection of the table reveals an excellent correlation as observed before.

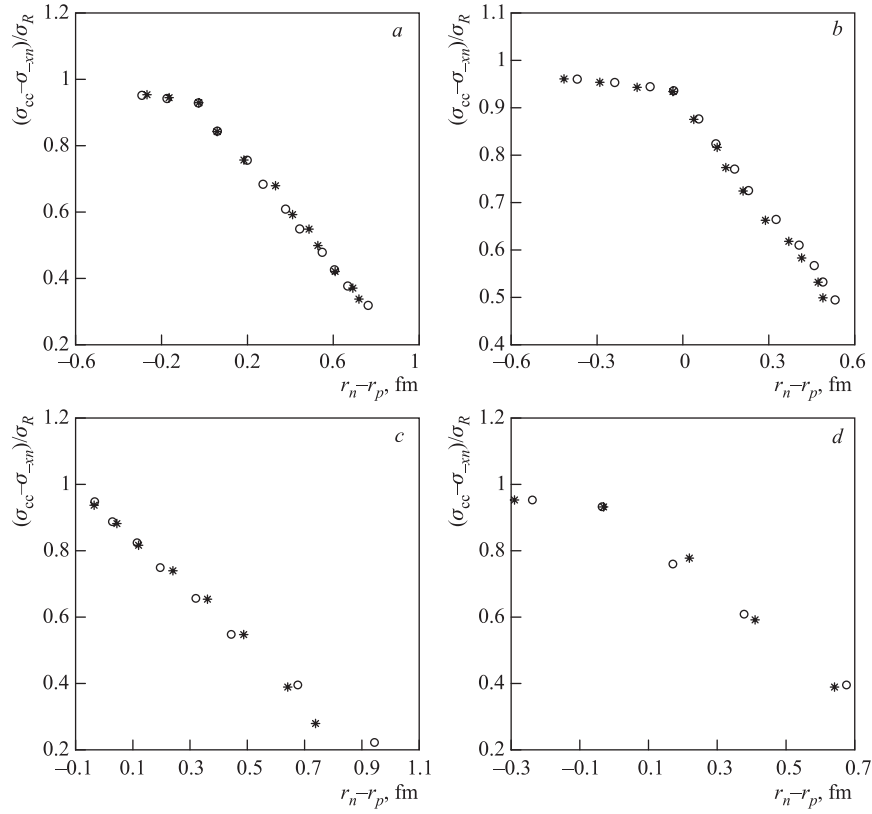


Fig. 33. The calculated ratio  $\mathcal{R}_{cc}^{-xn}$  (Eq. (87)) for N (a), Ne (b),  $N = 12$  (c), and  $A = 18$  (d) chains as a function of the corresponding nuclear skin thickness values ( $r_n - r_p$ ). ○ — RHB(c); \* — DEF

Table 9. The calculated correlation coefficients, slope coefficients and the standard errors

Nuclei	Approximation	$\mathcal{C}$	$m$	$e$
N	RHB(c)	-0.999	-0.775	0.010
	DEF	-0.997	-0.776	0.020
Ne	RHB(c)	-0.999	-0.771	0.012
	DEF	-0.998	-0.801	0.019
$N = 12$	RHB(c)	-0.998	-0.745	0.020
	DEF	-0.996	-0.832	0.032
$A = 18$	RHB(c)	-0.999	-0.751	0.020
	DEF	-0.995	-0.819	0.055

It should be noted that the correlation has been calculated by leaving out the «plateau» region of the graphs (33).

*Results of Finite Range Glauber Model.* We now present some of the preliminary results of the finite range Glauber model calculations. A significant amount of experimental data for the low-energy reaction cross section measurements, for stable

as well as unstable projectiles exists in the literature [102–104]. As illustrative examples, we have chosen two cases: 1)  $^{12}\text{C}$  on  $^{12}\text{C}$  reactions (energy dependence) and 2) cross sections for chain of neutron-deficient Selenium isotopes as projectiles, incident on  $^{28}\text{Si}$  target at low energies ( $\sim 50 A \cdot \text{MeV}$ ).

The calculated Glauber model reaction cross sections for  $^{12}\text{C}$  projectile incident on  $^{12}\text{C}$  target at different energies are shown in Fig. 34, *a*. It can be clearly seen that at energies below around  $150 A \cdot \text{MeV}$ , the finite range Glauber model (FRGM) results are in excellent agreement with the experiment [90, 102], in comparison with the corresponding zero range (ZRGM) results. At higher projectile energies, the difference between the two models decreases. Both of these are in good agreement with the experiment at the higher projectile energies.

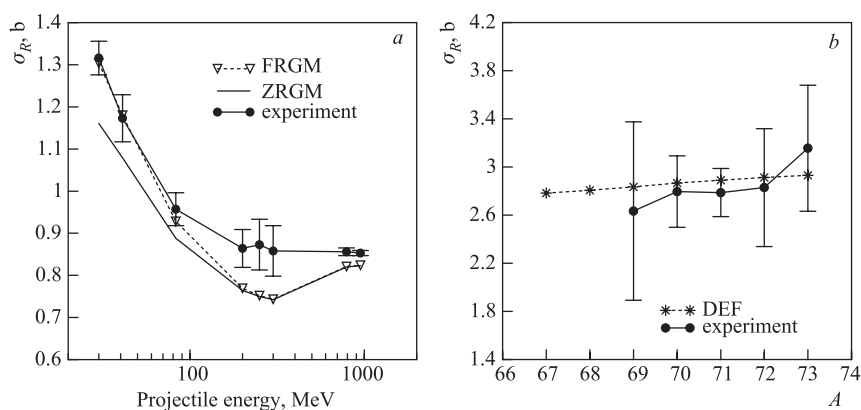


Fig. 34. The calculated and the experimental reaction cross sections for: *a*)  $^{12}\text{C}$  projectiles on  $^{12}\text{C}$  target (energy dependence); *b*) Selenium projectiles on  $^{28}\text{Si}$  target. See the text for details

Next, the calculated (DEF) reaction cross sections for neutron-deficient Selenium isotopes are presented in Fig. 34, *b*, along with the corresponding experimental values [104]. The agreement between the calculations and the experiment is found to be excellent within the limits of the experimental error bars.

## 7. DECAY HALF-LIVES

The production, identification and study of the superheavy elements is of current interest, and is being vigorously pursued by a number of laboratories around the world. All these are very short lived, and decay primarily through spontaneous  $\alpha$  emission. Thus, they can be identified through the  $\alpha$ - $\alpha$  correlations. So far, the elements up to  $Z = 116$  have been successfully produced and

identified. Here, we use the RMF formalism to study the superheavy nuclei, with the primary focus on the decay properties. For illustration, we present the results for the  $\alpha$  decay chains of  $^{271}\text{Ds}$  ( $Z = 110$ ) and  $^{278}113$ . The calculation proceeds in three steps. The ground state properties of the relevant nuclei are calculated using the RMF theory. Next, the calculated densities are used to determine the nucleus–nucleus interaction potential within the double folding model [105–108]. The resulting potential, along with the nucleus–nucleus Coulomb potential are used in the WKB model to determine the decay half-lives. This prescription has been applied successfully to describe the  $\alpha$  decay of the superheavy nucleus  $^{277}112$  [109].

The cluster radioactivity of the heavy nuclei [44–50] is one of the most striking discoveries in the nuclear physics. We investigate the cluster decay properties of the heavy nuclei using the RMF coupled with the double folding and WKB approaches, in analogy with the  $\alpha$ -decay investigations of the superheavy nuclei. Here, as an illustrative example, we present and discuss the  $^{14}\text{C}$  radioactivity of the Radium isotopes.

The essentials of the double folding procedure now follow.

**7.1. Double Folding Model.** The basic idea behind the double folding model is to get a reasonable nucleus–nucleus potential, knowing some nucleon–nucleon interaction (e.g., M3Y interaction, etc.). In general, the double folding potential comprises of the direct and the exchange terms. The direct term contains the direct nucleon–nucleon matrix elements, whereas, the exchange term, as the name suggests, contains the exchange part. The latter is considerably more difficult to handle in practice. Thus, for some of the applications, the exchange term is *simulated* by a delta function pseudopotential, with some density dependence.

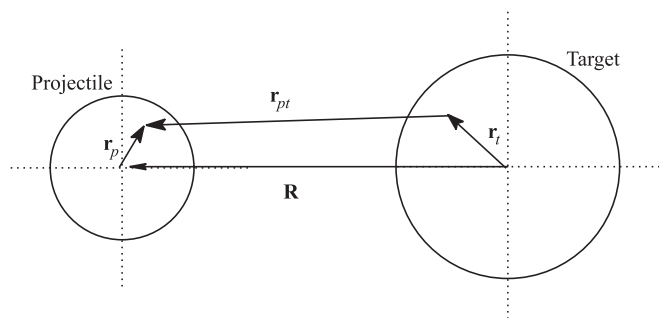


Fig. 35. Geometry of the double folding prescription

In the present work, the double folding prescription to obtain the nucleus–nucleus potential has been used (refer to Fig. 35 for the geometry of the problem). The M3Y effective nucleon–nucleon interaction employed here is given by [106, 108]:

$$v^{\text{M3Y}} = 7999 \frac{e^{-4s}}{4s} - 2134 \frac{e^{-2.5s}}{2.5s}. \quad (88)$$

The exchange effects are considered only through a delta-function pseudopotential [106]:

$$v^{\text{pseudo}} = J_{00}(E)\delta(s), \quad (89)$$

where the volume integral ( $J_{00}$ ) is [106]:

$$J_{00} = -276 \left( 1 - \frac{0.005E}{A_\alpha} \right), \text{ MeV} \cdot \text{fm}^3. \quad (90)$$

In the present work, the energy dependence is ignored. Thus, the M3Y interaction with pseudopotential becomes:

$$v^{\text{M3Y+pseudo}} = 7999 \frac{e^{-4s}}{4s} - 2134 \frac{e^{-2.5s}}{2.5s} - 276\delta(s), \text{ MeV}. \quad (91)$$

The density dependence is supposed to compensate to some extent the higher-order exchange effects and the effects of the Pauli blocking. Following the earlier work [106], it is assumed to be of the form:

$$v^{\text{dd}} = C(1 - \beta(E)\rho_1^{2/3})(1 - \beta(E)\rho_2^{2/3}), \quad (92)$$

where  $C$  is the overall normalization constant and is taken to be 1.0 in the present work.  $\beta(E)$  is the energy-dependent part of the density-dependent term and is assumed to have a constant value, 1.6 [106].

With the density dependence and the M3Y with pseudopotential, the assumed nucleon–nucleon interaction is now given by:

$$v(s) = C \left( 7999 \frac{e^{-4s}}{4s} - 2134 \frac{e^{-2.5s}}{2.5s} - 276\delta(s) \right) \times \\ \times \left( 1 - \beta(E)\rho_1^{2/3} \right) \left( 1 - \beta(E)\rho_2^{2/3} \right). \quad (93)$$

In these expressions,  $\beta(E)$  is 1.6 and  $s$  is equal to  $\mathbf{r}_{pt}$  (refer to the figure).

The total double folding potential between the nucleus–nucleus system is:

$$V_{\text{PT}}(\mathbf{R}) = \int \rho_P(\mathbf{r}_p)\rho_T(\mathbf{r}_t)v(\mathbf{r}_p - \mathbf{r}_t + \mathbf{R})d\mathbf{r}_p d\mathbf{r}_t, \quad (94)$$

where  $v$  is as defined above (Eq. (93)). In the actual calculations, we evaluate the six-dimensional integral in the above equation by transforming it into the momentum space. The details are easy to work out and are straightforward.

In order to evaluate the half-life time of the nucleus against  $\alpha$  (cluster) decay, one needs to know the nuclear potential, the Coulomb potential and the energy of the  $\alpha$  (cluster), which in turn is obtained by the  $Q$  value and the zero-point energy of the oscillation of the  $\alpha$  (cluster) in the potential well. It should be noted that, in the present case, it is assumed that the  $\alpha$  (cluster) is already formed in the parent nucleus, so that its motion can be simulated by assuming that it is moving in an average potential well formed by the *daughter*- $\alpha$  (cluster) system. The Coulomb potential ( $V_C(R)$ ) required in this case, is obtained by double folding the point proton densities of a daughter and  $\alpha$  (cluster) with the Coulomb interaction.

Here the decay half-life is calculated using the WKB approximation. The half-life time of the nucleus (parent) against the  $\alpha$  decay is then given by

$$T_{1/2} = \frac{\ln 2}{\nu} (1 + e^K). \quad (95)$$

Within the WKB approximation, the action integral is given by

$$K = \frac{2}{\hbar} \int_{R_a}^{R_b} \{2\mu (E(R) - Q)\}^{1/2} dR, \quad (96)$$

where  $\mu$  is the reduced mass of the  $\alpha$  (cluster)-daughter system. The total interaction potential  $E(R)$  is written as

$$E(R) = V_{PT}(R) + V_C(R) + \frac{\hbar^2 \lambda^2}{2\mu r^2}, \quad (97)$$

with  $V_{PT}$  as defined by Eq. (94) and  $V_C(R)$  is the double folded Coulomb potential. The last term with  $\lambda = l + 1/2$  represents the centrifugal term and reduces to the usual  $l(l + 1)$  form for large  $l$ . This term is usually known as the Langer term [110] and is used in the WKB approximation. In the present work, we take  $l = 0$ . The  $R_a$  and  $R_b$  in Eq. (96) are the lower and upper turning points, respectively. These are determined through the requirement:

$$E(R_a) = Q + E_\nu = E(R_b).$$

In Eq. (95),  $\nu$  is the assault frequency, given by

$$\nu = \left( \frac{1}{2R} \sqrt{\frac{2E}{M}} \right), \quad (98)$$

where  $R$  is the radius of the parent, given by  $R = 1.2A^{1/3}$ ;  $E$  is the energy of the cluster, corrected for recoil;  $M$  is the mass of cluster, expressed in MeV.

**7.2.  $\alpha$  Radioactivity of  $^{271}\text{Ds}$ ,  $^{278}\text{113}$ .** We now present and discuss application of the RMF formalism to the superheavy elements. Our aim is to calculate the half-lives of these nuclei against  $\alpha$  decay. The calculations proceed in three steps. The ground state properties are first calculated using RMF formalism. The  $\alpha$ -daughter interaction potentials are next determined within the framework of double folding procedure. The calculated as well as the experimental  $Q$  values against  $\alpha$  decay are then used in the WKB approximation for determining the half-lives.

Extensive calculations of all the  $\alpha$ -decay chains observed so far have been carried out. Here, as an illustrative example, we present and discuss the results for  $\alpha$ -decay chains of  $^{271}\text{Ds}$  and  $^{278}\text{113}$  ( $A = 278$ ,  $Z = 113$ ) only. It is interesting to note that all the observed nuclei in this mass region are found to be prolate deformed. Therefore, it is sufficient to present the results obtained by solving RMF equations in deformed oscillator basis.

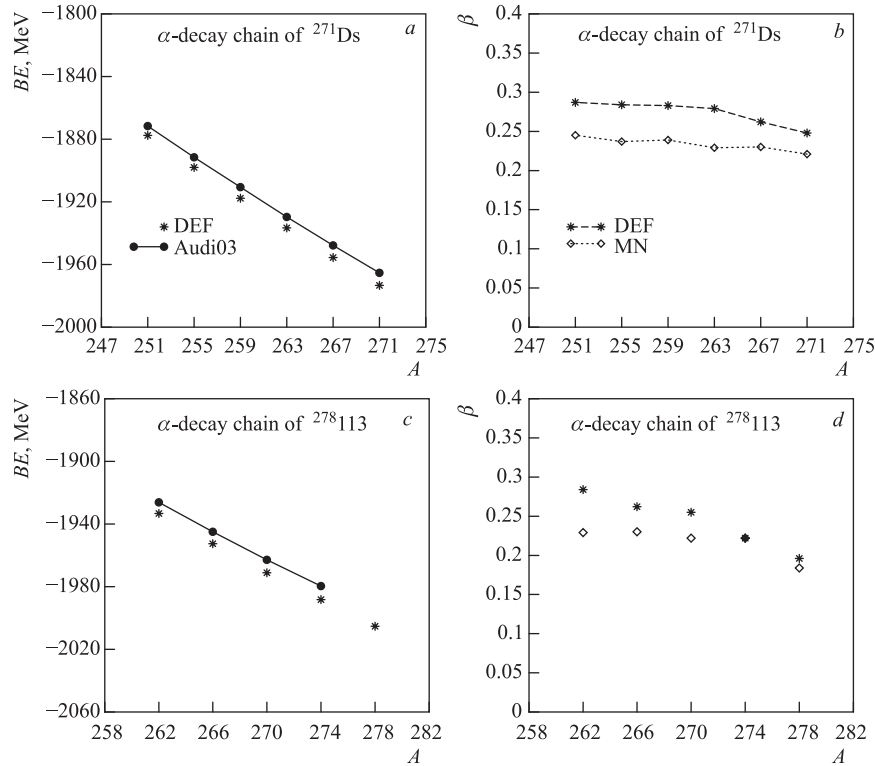


Fig. 36. *a, c*) The calculated and the Audi–Wapstra [66] binding energies for the nuclei belonging to  $\alpha$ -decay chains of  $^{271}\text{Ds}$ ,  $^{278}\text{113}$  and the quadrupole deformation parameters. *b, d*) The corresponding Moller–Nix values [68] are also indicated for comparison

**Binding Energies.** The calculated and the corresponding extrapolated (Audi03) [66] binding energies for the nuclei appearing in the  $\alpha$ -decay sequences of the superheavy nuclei  $^{271}\text{Ds}$  and  $^{278}113$  are presented in Fig. 36, *a, c*. It is clearly seen that the calculations are in good agreement (about 5 parts in 2000) with the corresponding extrapolated values [66]. This quality of agreement (0.25%, on the average) is also found for all the observed decay chains of the superheavy nuclei.

**Deformations.** The quadrupole deformation parameters ( $\beta$ ) are obtained from the calculated point neutron ( $Q_n$ ) and proton ( $Q_p$ ) quadrupole moments through:

$$Q = Q_n + Q_p = \sqrt{\frac{16\pi}{5}} \frac{3}{4\pi} AR_0^2\beta$$

with  $R_0 = 1.2A^{1/3}$  fm. The calculated  $\beta$  for the nuclei considered are shown in Fig. 36, *b, d*, along with the corresponding values of the microscopic–macroscopic (mic–mac) calculations of Möller–Nix (MN) [68]. All the nuclei investigated here turn out to be prolate. By and large, this observation agrees with the predictions of Möller and Nix [68]. Minor differences do exist at some places.

**Single-Particle States.** To convey the structure of the single-particle levels, we display these levels (two below and two above the Fermi surface) in Fig. 37 for the nuclei appearing in the  $\alpha$ -decay chains of superheavy nuclei  $^{271}\text{Ds}$  and  $^{278}113$ . These are reasonable and are as expected.

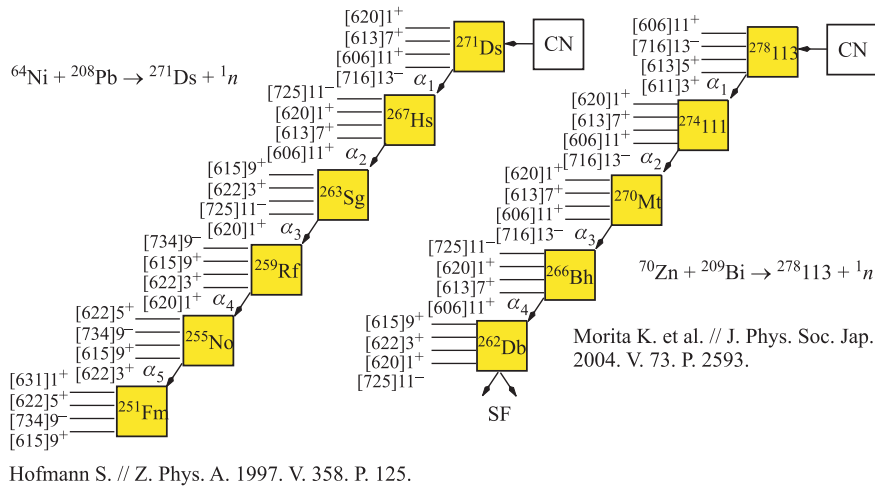


Fig. 37. Single-particle level structure near the Fermi level

*Matter Radii.* The root-mean-square (r.m.s.) matter radii ( $r_m$ ) are obtained from the r.m.s. proton and neutron radii through

$$r_m^2 = \frac{Zr_p^2 + Nr_n^2}{Z + N}. \quad (99)$$

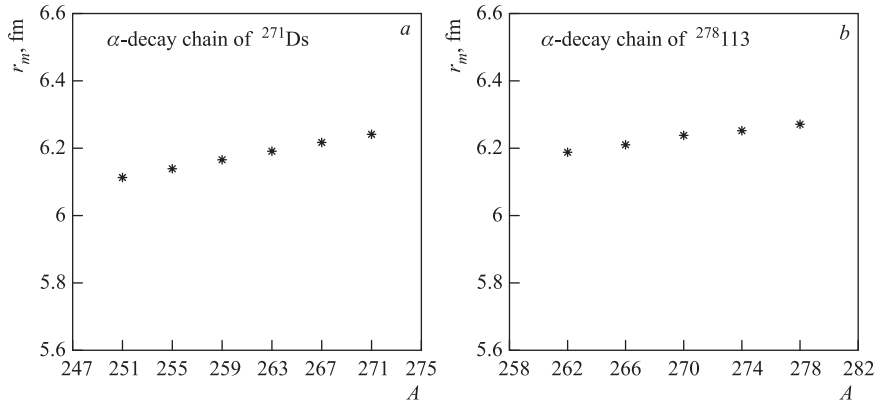


Fig. 38. The r.m.s. matter radii. \* — DEF

These are of considerable interest to the experimental community. The calculated  $r_m$  values are shown in Fig. 38. They are found to be varying monotonically with the mass number. The corresponding radius parameter is defined by

$$r_0 = \frac{r_m}{A^{1/3}}, \quad (100)$$

where  $A$  is the mass number. The calculated parameter  $r_0$  for all the known chains of superheavy elements in the range  $108 \leq Z \leq 118$  is plotted in Fig. 39. The parameter  $r_0$  is found to be a constant to a good degree of precision, with average value 0.965 (with  $\sigma = 0.0005$ ) fm. This  $r_0$  (Eq. (100)) should be distinguished from the one used, e.g., by Buck et al. [111] and Akevali [112], in the calculation of the hindrance factors. There,  $r_0$  really corresponds to the size of the potential well used.

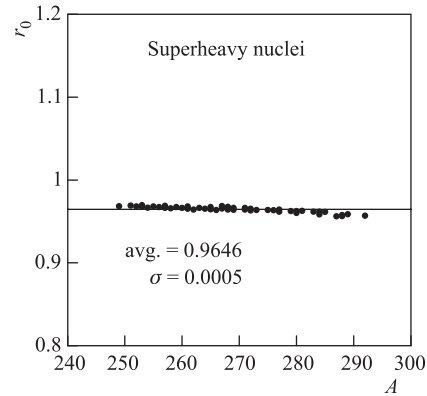


Fig. 39. The radius parameter ( $r_0 = r_m/A^{1/3}$ ,  $A$  being the mass number) for all the known heavy nuclei in the range  $108 \leq Z \leq 116$

A few superdeformed ground state solutions exist for some of the superheavy nuclei (e.g.,  $^{292}116$ ,  $^{288}114$ , etc.). Such solutions are also reported earlier by Ren [113] and also by Sharma et al. [114]. These superdeformed solutions seem to be unphysical and may disappear if the higher multipolar constraints are imposed. This assertion is supported by the recent mic-mac calculations by Muntian and Sobiczewski [115].

*Q Values.* The  $Q$  value of a parent nucleus against  $\alpha$  decay is just the difference between the binding energy of the parent nucleus and the sum of binding energies of the daughter nucleus and  $\alpha$  nucleus. The results for both (Ds and  $Z = 113$ ) chains are shown in Fig. 40, *a, c*. The calculations are found to be in agreement with the corresponding experimental values. The calculations differ from the experiment at some places, the maximum departure being of the order of 1 MeV. This is gratifying in the view of the fact that, the  $Q$  values being the difference between large numbers, a small error in even one of them could affect the  $Q$  values substantially.

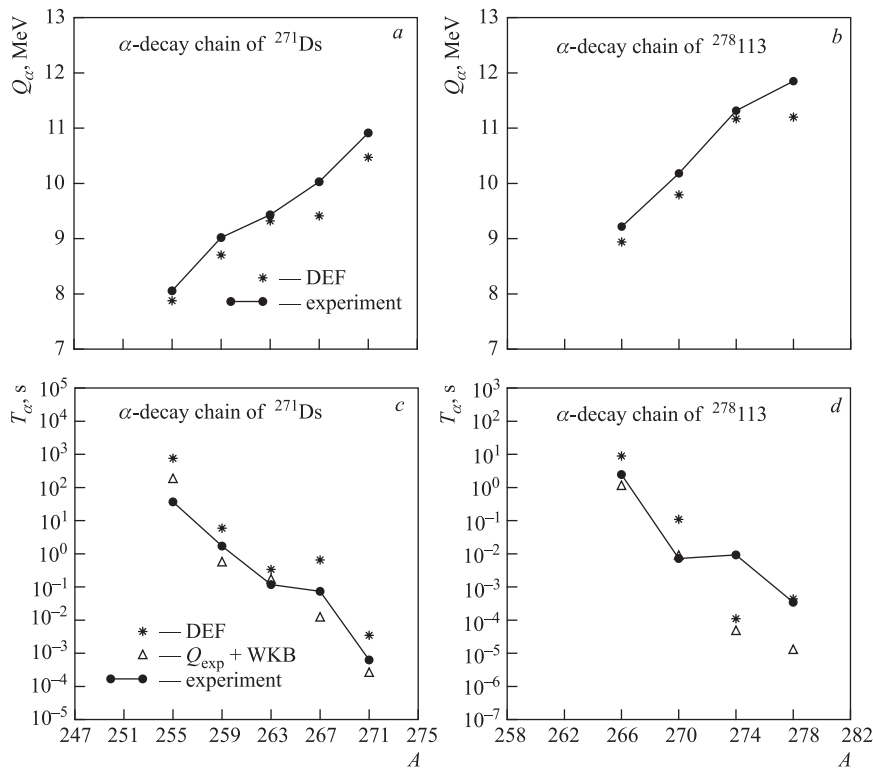


Fig. 40. *a, c*) The  $Q$  values against  $\alpha$  decay. The corresponding experimental values [40, 116] are also shown, where available. *b, d*) Half-lives against  $\alpha$  decay of superheavy nuclei

*Half-Lives.* The calculated and the corresponding experimental half-lives for the superheavy nuclei against  $\alpha$  decay are presented in Fig. 40, *b, d*. The half-lives obtained by using the calculated  $Q$  values in the WKB procedure are denoted by DEF, whereas those obtained by using the corresponding experimental  $Q$  are denoted by  $Q_{\text{exp}} + \text{WKB}$  in Fig. 40. Both the calculations qualitatively agree with the experiment. The differences, even of the order of magnitude exist. The half-lives obtained by using the calculated  $Q$  values, though similar to the experimental trend, differ from it quantitatively at places. This reflects hypersensitivity of the half-lives on  $Q$  values. It is clearly seen that the use of experimental  $Q$  values in WKB approach brings the calculated half-lives much closer to the experiment. This reflects reliability of the calculated nucleus–nucleus potential. It, therefore, can be used with confidence in the reaction calculations, e.g., as the real part of the optical potential.

Similar calculations of half-lives for all the chains of superheavy nuclei observed to date have been carried out [117], with similar quality of agreement with the corresponding experimental values.

**7.3. Cluster Decay of Radium Isotopes.** One of the interesting discoveries in nuclear physics is the cluster decay. In all, five of the Radium isotopes have been found to be spontaneous  $^{14}\text{C}$  emitters. This is one of the reasons for selecting the chain of Radium isotopes in the present study. Here, we investigate the cluster-decay properties of some of the Radium isotopes ( $^{221-226}\text{Ra}$ ). As mentioned in Sec. 7, the calculations are carried out in three steps. In the first step, the relevant ground state properties are calculated within the framework of relativistic mean field theory. Two properties are essential here: the binding energy (to obtain  $Q$  value for cluster decay) and the total (proton + neutron) density of daughter as well as the cluster (to calculate the double folding potential).

Most of the Radium isotopes in the region of interest turn out to be deformed. Therefore, here we only present and discuss the results obtained by solving RMF equations in the deformed oscillator basis (DEF).

The calculated  $Q$  values for  $^{14}\text{C}$  decay of the Radium isotopes are plotted in Fig. 41 along with the corresponding experimental values [66]. The figure reveals that the calculated  $Q$  values are in overall good agreement with the experiment [66]. The maximum departure is of the order of 2 MeV (about 6%).

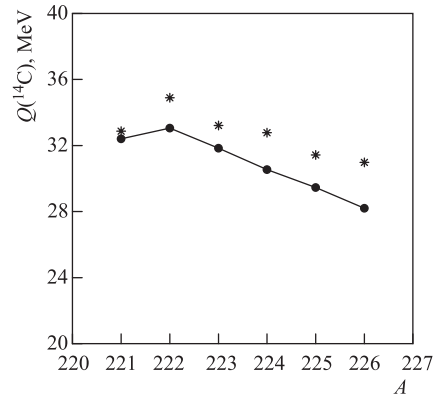


Fig. 41. The calculated (DEF (\*))  $Q$  values for  $^{14}\text{C}$  decay of Radium isotopes, along with the corresponding experimental values (●, solid curves) [66], where available

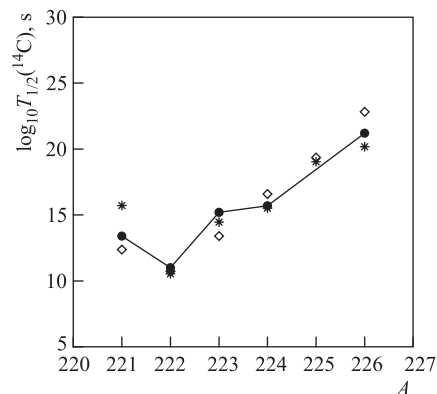


Fig. 42. The calculated (DEF (\*)) half-lives for  $^{14}\text{C}$  decay of Radium isotopes, along with the corresponding experimental values (●, solid curves) [50], where available. The results obtained by using the corresponding experimental  $Q$  values are also shown ( $Q_{\text{exp}}$ )

The calculated half-lives are next presented in Fig. 42 along with the experimental values [50], where available. Here, the label DEF corresponds to the half-lives obtained by using the DEF  $Q$  values in the WKB approach,  $Q_{\text{exp}}$  indicates the half-lives obtained by using the experimental  $Q$  values in the WKB framework. Clearly, the use of experimental  $Q$  values in the double folding plus WKB approach reproduces the experimental half-lives well. Even the DEF results are found to be reasonable. This graph also shows the sensitive dependence of half-lives on the  $Q$  values: a few per cent change in  $Q$  values changes the calculated half-lives by orders of magnitude. An exhaustive study of the observed cluster decays has been carried out recently [118] along the similar lines.

## SUMMARY AND CONCLUSIONS

The salient features of RMF are presented. The results of a few selected isotopic/isotonic/isobaric chains spread over the entire periodic table are presented and discussed. The inclusion of deformation is found to be important for an accurate description, particularly, of binding energies and charge radii. The calculations reproduce the ground state properties remarkably well. The total binding energies are reproduced, on the average, within 0.25% and the calculated charge radii differ only in the second decimal place of fermi from the corresponding experimental values. It is observed that the binding energies of the nuclei with large neutron excess are overestimated. This trend persists throughout the low mass region. This may point towards the need to fine tune the Lagrangian parameters, especially in the isospin sector. The RMF successfully accounts for the observed peripheral factors, extracted in the antiproton annihilation experiments. It is interesting to note that the RMF establishes the origin of pseudospin symmetry, which was till recently a mystery, to be relativistic.

The RMF densities used in the Glauber model successfully describe the observed total reaction cross sections. The transparency function of the Glauber

model has successfully been factorized to give *consistent* definitions of the charge-changing as well as the neutron removal (stripping) cross sections. The proposed forms for these cross sections are shown to be consistent with the observed charge-changing and neutron removal cross sections. In short, the present framework successfully and consistently describes the reaction and charge-changing (neutron removal) cross sections.

The calculated  $Q$  values of the superheavy nuclei against the  $\alpha$  decay are found to be in reasonably good agreement with the experiment. The calculations deviate from the corresponding experiment, at the most by 1 MeV. The half-lives obtained by using these  $Q$  values, though qualitatively similar to the experiment, do differ significantly at some places, implying that the half-lives depend very sensitively on the  $Q$  values used. On the other hand, the use of experimental  $Q$  values improves the agreement significantly. This implies that the calculated double folding potential is reliable and can be used with confidence in other reaction studies as the real part of the optical potential. Similar remarks do hold for the cluster radioactivity of heavy nuclei.

To conclude, the relativistic formulation and its remarkably accurate description of nuclear properties with only a few fixed parameters is now considered to be one of the most striking developments in the field of nuclear theory.

**Acknowledgements.** The authors are grateful to P. Ring, M. M. Sharma, G. M $\ddot{u}$ nzenberg, J. Meng, G. A. Lalazissis, M. Gupta, A. K. Jain, and S. H. Patil for their interest in the work. The financial support of the Board of Research in Nuclear Sciences (BRNS), Government of India (Proj. No. 2001/37/13/BRNS/692) is gratefully acknowledged.

#### REFERENCES

1. *Walecka J. D.* A theory of highly condensed matter // *Ann. Phys.* 1974. V. 83. P. 491–529.
2. *Serot B. D., Walecka J. D.* // *Adv. Nucl. Phys.* 1986. V. 16. P. 1 and references cited therein.
3. *Reinhardt P.-G. et al.* Nuclear ground state properties in a relativistic mean-field theory // *Z. Phys. A.* 1986. V. 323. P. 13–25;  
*Reinhardt P.-G.* The relativistic mean-field description of nuclei and nuclear dynamics // *Rep. Prog. Phys.* 1989. V. 52. P. 439–514 and references cited therein.
4. *Bouyssy A. et al.* Relativistic description of nuclear systems in the Hartree–Fock approximation // *Phys. Rev. C.* 1987. V. 36. P. 380–401 and references cited therein.
5. *Gambhir Y. K., Ring P.* The relativistic mean-field description of the ground-state nuclear properties // *Pramana.* 1989. V. 32. P. 389–404.
6. *Gambhir Y. K., Ring P., Thimet A.* Relativistic mean-field theory for finite nuclei // *Ann. Phys. (N. Y.)* 1990. V. 198. P. 132–179 and references cited therein.
7. *Serot B. D.* Quantum hydrodynamics // *Rep. Prog. Phys.* 1992. V. 55. P. 1855–1946 and references cited therein.
8. *Ring P.* Relativistic mean-field theory in finite nuclei // *Prog. Part. Nucl. Phys.* 1996. V. 37. P. 193–263 and references cited therein.

9. Ring P., Schuck P. The Nuclear Many-Body Problem. Heidelberg: Springer-Verlag, 1980.
10. Kucharek H., Ring P. Relativistic field theory of superfluidity in nuclei // Z. Phys. A. 1991. V. 339. P. 23–35.
11. Furnstahl R. J., Serot B. D., Tang Hua-Bin. Analysis of chiral mean-field models for nuclei // Nucl. Phys. A. 1996. V. 598. P. 539–582 and references cited therein.
12. Furnstahl R. J., Serot B. D., Tang Hua-Bin. A chiral effective lagrangian for nuclei // Nucl. Phys. A. 1997. V. 615. P. 441–482 and references cited therein.
13. Furnstahl R. J., Serot B. D. Parameter counting in relativistic mean-field models // Nucl. Phys. A. 2000. V. 671. P. 447–460 and references cited therein.
14. Serot B. D. Covariant effective field theory for nuclear structure and currents. nucl-th/0405058. 2004 and references cited therein.
15. Nikolaus B. A., Hoch T., Madland D. G. Nuclear ground state properties in a relativistic point coupling model // Phys. Rev. C. 1992. V. 46. P. 1757–1781 and references cited therein.
16. Bürvenich T. et al. Nuclear ground state observables and QCD scaling in a refined relativistic point coupling model // Phys. Rev. C. 2002. V. 65. P. 044308-1-23 and references cited therein.
17. Madland D. G. et al. On the isovector channels in relativistic point coupling models within the Hartree and Hartree-Fock approximations // Nucl. Phys. A. 2004. V. 741. P. 52–59 and references cited therein.
18. Aufmuth P., Heiling K., Steudel A. Changes in mean-square nuclear charge radii from optical isotope shifts // At. Data Nucl. Data Tables. 1987. V. 37. P. 455–490.
19. Otten E. W. // Treatise Heavy-Ion Sci. (N. Y.). 1989. V. 8. P. 517 and references cited therein.
20. Geithner W. Ph.D. CERN-THESIS-2002-030. 2002; references cited therein.
21. Billowes J., Campbell P. High-resolution laser spectroscopy for the study of nuclear sizes and shapes // J. Phys. G: Nucl. Part. Phys. 1995. V. 21. P. 707–739.
22. Hecht K. T., Alder A. Generalized seniority for favored  $J = 0$  pairs in mixed configurations // Nucl. Phys. A. 1969. V. 137. P. 129–143.
23. Arima A., Harvey M., Shimizu K. Pseudo-LS coupling and pseudo- $SU_3$  coupling schemes // Phys. Lett. B. 1969. V. 30. P. 517–522.
24. Ginocchio J. N. Pseudospin as a relativistic symmetry // Phys. Rev. Lett. 1997. V. 78. P. 436–439.
25. Gambhir Y. K., Maharana J. P., Warke C. S. Pseudospin as a relativistic symmetry // Eur. Phys. J. A. 1998. V. 3. P. 255–262.
26. Meng J. et al. Pseudospin symmetry in relativistic mean-field theory // Phys. Rev. C. 1998. V. 58. P. R628–R631.
27. Lalazissis G. A. et al. Relativistic mean-field approach and the pseudospin symmetry // Ibid. P. R45–R48.
28. Lubinski P. et al. Neutron halo in heavy nuclei from antiproton absorption // Phys. Rev. Lett. 1995. V. 73. P. 3199–3202.
29. Lubinski P. et al. Composition of the nuclear periphery from antiproton absorption // Phys. Rev. C. 1996. V. 57. P. 2962–2973 and references cited therein.
30. Wycech S. et al. Antiprotonic studies of nuclear neutron halos // Ibid. V. 54. P. 1832–1842 and references cited therein.
31. Jastrzebski J. et al. Antiprotonic investigation of the nuclear periphery // Nucl. Phys. B (Proc. Suppl.). 1997. V. 56A. P. 108–113.

32. Schmid R. *et al.* Composition of the nuclear periphery from antiproton absorption using short-lived residual nuclei // *Phys. Rev. C.* 1999. V. 60. P. 054309-1-9.
33. Ozawa A., Suzuki T., Tanihata I. Nuclear size and related topics // *Nucl. Phys. A.* 2001. V. 693. P. 32–62 and references cited therein.
34. Glauber R. J. *Lectures in Theoretical Physics* / Eds. W. Brittin, L. Dunham. Interscience Publishers Inc., 1959. V. 1. P. 315.
35. Bochkarev O. V. *et al.* Evidence for a neutron skin in  $^{20}\text{N}$  // *Eur. Phys. J. A.* 1998. V. 1. P. 15.
36. Bhagwat A., Gambhir Y. K. Microscopic investigations of mass and charge-changing cross sections // *Phys. Rev. C.* 2004. V. 69. P. 014315-1-11.
37. Chulkov L. *et al.* Total charge-changing cross sections for neutron-rich light nuclei // *Nucl. Phys. A.* 2000. V. 674. P. 330–342.
38. Nilsson S. G. *et al.* On the nuclear structure and stability of heavy and superheavy elements // *Nucl. Phys. A.* 1969. V. 131. P. 1–66.
39. Mosel U., Greiner W. On the stability of superheavy nuclei against fission // *Z. Phys.* 1969. V. 222. P. 261–282.
40. Hofmann S. Heavy and superheavy nuclei // *Z. Phys. A.* 1997. V. 358. P. 125–129.
41. Oganessian Yu. Ts. *et al.* Synthesis of superheavy nuclei in the  $^{48}\text{Ca} + ^{244}\text{Pu}$  reaction // *Phys. Rev. Lett.* 1999. V. 83. P. 3154–3157.
42. Oganessian Yu. Ts. *et al.* Synthesis of superheavy nuclei in the reactions of  $^{244}\text{Pu}$  and  $^{248}\text{Cm}$  with  $^{48}\text{Ca}$  // *Eur. Phys. J. A.* 2002. V. 15. P. 201–204.
43. Oganessian Yu. Ts. *et al.* Experiments on the synthesis of element 115 in the reaction  $^{243}\text{Am}(^{48}\text{Ca}, xn)^{291-x}115$  // *Phys. Rev. C.* 2004. V. 69. P. 021601 (R)-1-5.
44. Rose H. J., Jones G. A. A new kind of natural radioactivity // *Nature (London)*. 1984. V. 307. P. 245–247.
45. Alexandrov D. V. *et al.* // *Zh. Eksp. Teor. Fiz.* 1984. V. 40. P. 909; *JETP Lett.* 1984. V. 40. P. 152.
46. Price P. B. *et al.* Discovery of radioactive decay of  $^{222}\text{Ra}$  and  $^{224}\text{Ra}$  by  $^{14}\text{C}$  emission // *Phys. Rev. Lett.* 1985. V. 54. P. 297–299.
47. Barwick S. W., Price P. B., Stevenson J. D. Radioactive decay of  $^{232}\text{U}$  by  $^{24}\text{Ne}$  emission // *Phys. Rev. C.* 1985. V. 31. P. 1984–1986.
48. Price P. B. Complex radioactivity // *Nucl. Phys. A.* 1989. V. 502. P. 41c–58c.
49. Poenaru D. N. *et al.* Nuclear lifetimes for cluster radioactivities // *At. Data Nucl. Data Tables.* 1991. V. 48. P. 231–327.
50. Poenaru D. N. *et al.* Systematics of cluster decay modes // *Phys. Rev. C.* 2002. V. 65. P. 054308-1-6 and references cited therein; Erratum. Systematics of cluster decay modes // *Phys. Rev. C.* 2002. V. 65. P. 054308; V. 66. P. 049902(E)-1-1.
51. Arnold L. G., Clark B. C., Mercer R. L. Relativistic optical model analysis of medium energy  $p$ - $^4\text{He}$  elastic scattering experiments // *Phys. Rev. C.* 1979. V. 19. P. 917–922.
52. Clark B. C. *et al.* Dirac-equation impulse approximation for intermediate-energy nucleon–nucleus scattering // *Phys. Rev. Lett.* 1983. V. 50. P. 1644–1647.
53. Murdock D. P., Horowitz C. J. Microscopic relativistic description of proton–nucleus scattering // *Phys. Rev. C.* 1987. V. 35. P. 1442–1462.
54. Kozack R., Madland D. G. Dirac optical potentials for nucleon scattering by  $^{208}\text{Pb}$  at intermediate energies // *Phys. Rev. C.* 1989. V. 39. P. 1461–1474.

55. Hama S. *et al.* Global Dirac optical potentials for elastic proton scattering from heavy nuclei // Phys. Rev. C. 1990. V. 41. P. 2737–2755.
56. Cooper E. D. *et al.* Global Dirac phenomenology for proton–nucleus elastic scattering // Phys. Rev. C. 1993. V. 47. P. 297–311.
57. Susan P., Shastry C. S., Gambhir Y. K. Salient features of scattering amplitudes in intermediate-energy nucleon–nucleus scattering // Phys. Rev. C. 1994. V. 50. P. 2955–2962.
58. Murdock D. P., Horowitz C. J. Microscopic relativistic description of proton–nucleus scattering // Phys. Rev. C. 1987. V. 35. P. 1442–1462.
59. Boguta J., Bodmer A. R. Relativistic calculation of nuclear matter and the nuclear surface // Nucl. Phys. A. 1977. V. 292. P. 413–428.
60. Decharge J., Gogny D. Hartree–Fock–Bogoliubov calculations with the D1 effective interaction on spherical nuclei // Phys. Rev. C. 1980. V. 21. P. 1568–1593.
61. Gonzalez-Llarena T. *et al.* Relativistic Hartree–Bogoliubov calculations with finite range pairing forces // Phys. Lett. B. 1996. V. 379. P. 13–19.
62. Meng J., Ring P. Relativistic Hartree–Bogoliubov description of the neutron halo in  $^{11}\text{Li}$  // Phys. Rev. Lett. 1996. V. 77. P. 3963–3966;  
Meng J. Relativistic continuum Hartree–Bogoliubov theory with both zero range and finite range Gogny force and their application // Nucl. Phys. A. 1998. V. 635. P. 3–42.
63. Lalazissis G. A., Konig J., Ring P. New parameterization for the Lagrangian density of relativistic mean-field theory // Phys. Rev. C. 1997. V. 55. P. 540–543.
64. Sharma M. M., Nagarajan M. A., Ring P. Rho-meson coupling in the relativistic mean-field theory and description of exotic nuclei // Phys. Lett. B. 1993. V. 312. P. 377–381.
65. Sharma M. M., Farhan A. R., Mythili S. Shell effects in nuclei with vector self-coupling of the omega meson in the relativistic Hartree–Bogoliubov theory // Phys. Rev. C. 2000. V. 61. P. 054306-1-15.
66. Audi G., Wapstra A. H., Thibault C. The AME2003 atomic mass evaluation. II. Tables, graphs and references // Nucl. Phys. A. 2003. V. 729. P. 337–676.
67. Bhagwat A., Gambhir Y. K. Recently observed charge radius anomaly in neon isotopes // Phys. Rev. C. 2003. V. 68. P. 044301-1-5.
68. Möller P. *et al.* Nuclear ground-state masses and deformations // At. Data Nucl. Data Tables. 1995. V. 59. P. 185–381.
69. Tanihata I. *et al.* Measurements of interaction cross sections and nuclear radii in the light  $p$ -shell region // Phys. Rev. Lett. 1985. V. 55. P. 2676–2679.
70. Ozawa A. *et al.* Interaction cross sections and radii of light nuclei // Nucl. Phys. A. 1996. V. 608. P. 63–76.
71. de Vries H., de Jager C. W., de Vries C. Nuclear charge density distribution parameters from elastic electron scattering // At. Data Nucl. Data Tables. 1987. V. 36. P. 495–536.
72. Klein A. *et al.* Moments and mean-square charge radii of short-lived argon isotopes // Nucl. Phys. A. 1996. V. 607. P. 1–22.
73. Thibault C. *et al.* Hyperfine structure and isotope shift of the D2 line of  $^{118-145}\text{Cs}$  and some of their isomers // Nucl. Phys. A. 1981. V. 367. P. 1–12.
74. Ozawa A. *et al.* Measurements of the interaction cross sections for Ar and Cl isotopes // Nucl. Phys. A. 2002. V. 709. P. 60–72; Erratum. Measurements of the interaction cross sections for Ar and Cl isotopes // Nucl. Phys. A. 2002. V. 709. P. 60; 2003. V. 727. P. 465–466.

75. *Chapman D.G., Schaufele R.A.* Elementary probability models and statistical inference. Waltham; Toronto: Xerox College Pub. Co., 1970.
76. *Bhagwat A., Gambhir Y.K.* Isospin dependence of ground state properties of  $A = 20$  isobars // Intern. J. Mod. Phys. E. 2004. V. 12. P. 725–745.
77. *Chulkov L. et al.* Interaction cross sections and matter radii of  $A = 20$  isobars // Nucl. Phys. A. 1996. V. 603. P. 219–237.
78. *Ozawa A. et al.* Interaction cross sections and radii of the mass number  $A = 17$  isobar ( $^{17}\text{N}$ ,  $^{17}\text{F}$ , and  $^{17}\text{Ne}$ ) // Phys. Lett. B. 1994. V. 334. P. 18–22.
79. *Nadjakov E.G., Marinova K.P., Gangrsky Yu.P.* Systematics of nuclear charge radii // At. Data Nucl. Data Tables. 1994. V. 56. P. 133–157.
80. *Shera E.B. et al.* Nuclear charge radii of the Te isotopes from muonic atoms // Phys. Rev. C. 1989. V. 39. P. 195–208.
81. *Ginocchio J.N., Leviatan A.* On the relativistic foundations of pseudospin symmetry in nuclei // Phys. Lett. B. 1998. V. 425. P. 1–5.
82. *Bohr A., Hamamoto I., Mottelson B.R.* Pseudospin in rotating nuclear potentials // Phys. Scr. 1982. V. 26. P. 273–279.
83. *Ratna Raju R.D., Draayer J.P., Hecht K.T.* Search for a coupling scheme in heavy deformed nuclei: The pseudo- $SU(3)$  model // Nucl. Phys. A. 1973. V. 202. P. 433–466.
84. *Meng J. et al.* Pseudospin symmetry in Zr and Sn isotopes from the proton drip line to the neutron drip line // Phys. Rev. C. 1999. V. 59. P. 154–163.
85. *Gambhir Y.K.* Nuclear Models / Ed. V. K. B. Kota. Allied Publishers Pvt. Limited, 2002.
86. *Brohm T. et al.* Total charge-changing cross sections of stable and neutron-deficient secondary projectiles around  $A = 60$  // Nucl. Phys. A. 1995. V. 585. P. 565–576.
87. *Landau L.M., Lifshitz E.M.* Quantum Mechanics: Nonrelativistic Theory. N.Y.: Pergamon Press, 1977.
88. *Ogawa Y., Yabana K., Suzuki Y.* Glauber model analysis of the fragmentation reaction cross sections of  $^{11}\text{Li}$  // Nucl. Phys. A. 1992. V. 543. P. 722–750.
89. *Charagi S.K., Gupta S.K.* Coulomb-modified Glauber model description of heavy-ion reaction cross sections // Phys. Rev. C. 1990. V. 41. P. 1610–1618.
90. *Zheng T. et al.* Study of halo structure of  $^{16}\text{C}$  from reaction cross section measurement // Nucl. Phys. A. 2002. V. 709. P. 103–118.
91. *Karol P.J.* Nucleus–nucleus reaction cross sections at high energies: Soft-spheres model // Phys. Rev. C. 1975. V. 11. P. 1203–1209.
92. *Westfall G.D. et al.* Fragmentation of relativistic  $^{56}\text{Fe}$  // Phys. Rev. C. 1979. V. 19. P. 1309.
93. *Greiner D.E. et al.* Uranium nuclear reactions at 900 MeV/nucleon // Phys. Rev. C. 1985. V. 31. P. 416–420.
94. *Binns W.R. et al.* Systematics of the release of residual nuclei from relativistic nucleus–nucleus interactions // Phys. Rev. C. 1987. V. 36. P. 1870–1885.
95. *Webber W.R., Kish J.C., Schrier D.A.* Total charge and mass changing cross sections of relativistic nuclei in hydrogen, helium, and carbon targets // Phys. Rev. C. 1990. V. 41. P. 520–526.
96. *Chen C.-X. et al.* Interactions in hydrogen of relativistic neon to nickel projectiles: Total charge-changing cross sections // Phys. Rev. C. 1994. V. 49. P. 3200–3210.
97. *Webber W.R. et al.* Measurement of charge-changing and isotopic cross sections at 600 MeV/nucleon from the interactions of 30 separate beams of relativistic nuclei from  $^{10}\text{B}$  to  $^{55}\text{Mn}$  in a liquid hydrogen target // Phys. Rev. C. 1998. V. 58. P. 3539–3552.

98. *Serber R.* Nuclear reactions at high energies // *Phys. Rev.* 1947. V. 72. P. 1114–1115.
99. *Gaimard J.-J., Schmidt K.-H.* A re-examination of the abrasion–ablation model for the description of the nuclear fragmentation reaction // *Nucl. Phys. A.* 1991. V. 531. P. 709–745.
100. *Meng J., Zhou S.-G., Tanihata I.* The relativistic continuum Hartree–Bogoliubov description of charge-changing cross section for C, N, O, and F isotopes // *Phys. Lett. B.* 2002. V. 532. P. 209–214.
101. *Bhagwat A., Gambhir Y. K., Patil S. H.* Nuclear densities in the neutron-halo region // *Eur. Phys. J. A.* 2000. V. 8. P. 511–520;  
*Bhagwat A., Gambhir Y. K., Patil S. H.* Nuclear densities of Li isotopes // *J. Phys. G: Nucl. Part. Phys.* 2001. V. 27. P. B1–B7.
102. *Kox S. et al.* Trends of total reaction cross sections for heavy ion collisions in the intermediate energy range // *Phys. Rev. C.* 1987. V. 35. P. 1678–1691 and references cited therein.
103. *Fang D. Q. et al.* Measurements of total reaction cross sections for some light nuclei at intermediate energies // *Phys. Rev. C.* 2000. V. 61. P. 064311-1-5.
104. *Lima G. F. et al.* Reaction cross section and matter radius measurements of proton-rich Ga, Ge, As, Se, and Br nuclides // *Nucl. Phys. A.* 2004. V. 735. P. 303–328.
105. *Satchler G. R., Love W. G.* Folding model potentials from realistic interactions for heavy-ion scattering // *Phys. Rep.* 1979. V. 55. P. 183–254 and references cited therein.
106. *Choudhuri A. K.* A density-dependent interaction in the folded alpha-nucleus potential // *Nucl. Phys. A.* 1986. V. 449. P. 243–250.
107. *Khoa D. T., von Oertzen W., Bohlen H. G.* Double-folding model for heavy-ion optical potential: Revised and applied to study  $^{12}\text{C}$  and  $^{16}\text{O}$  elastic scattering // *Phys. Rev. C.* 1994. V. 49. P. 1652–1668 and references cited therein.
108. *Khoa D. T.* Alpha-nucleus optical potential in the double-folding model // *Phys. Rev. C.* 2001. V. 63. P. 034007-1-15 and references cited therein.
109. *Gambhir Y. K. et al.* Alpha radioactivity of superheavy nuclei // *Phys. Rev. C.* 2003. V. 68. P. 044316-1-6.
110. *Langer R. E.* On the connection formulas and the solutions of the wave equation // *Phys. Rev.* 1937. V. 51. P. 669–676.
111. *Buck B., Merchant A. C., Perez S. M.* New look at alpha decay of heavy nuclei // *Phys. Rev. Lett.* 1990. V. 65. P. 2975–2977.
112. *Akovali Y. A.* Review of alpha-decay data from doubly-even nuclei // *Nucl. Data Sheets.* 1998. V. 84. P. 1–114.
113. *Ren Z.* Shape coexistence in even–even superheavy nuclei // *Phys. Rev. C.* 2002. V. 65. P. 051304(R)1-5.
114. *Sharma M. M., Farhan A. R., Münzenberg G.* Alpha-decay properties of superheavy elements  $Z = 113–125$  in the relativistic mean field theory with vector self-coupling of  $\omega$  meson. nucl-th/0409066 2005.
115. *Muntian I., Sobiczewski A.* Superdeformed ground state of superheavy nuclei // *Phys. Lett. B.* 2004. V. 586. P. 254–257 and references cited therein.
116. *Morita K. et al.* Experiment on the synthesis of element in the reaction  $^{209}\text{Bi}(^{70}\text{Zn}, n)^{278}113$  // *J. Phys. Soc. J.* 2004. V. 73. P. 2593–2596.
117. *Gambhir Y. K., Bhagwat A., Gupta M.* Alpha-decay half-lives of the observed superheavy nuclei ( $Z = 108–118$ ) // *Phys. Rev. C.* 2005. V. 71. P. 037301-1-4.
118. *Bhagwat A., Gambhir Y. K.* Relativistic mean-field description of cluster radioactivity // *Phys. Rev. C.* 2005. V. 71. P. 017301-1-4.